SISSA - International School for Advanced Studies

ICTP - International Center for Theoretical Physics

Modified Gravity in Cluster of Galaxies

Thesis Submitted for the Degree of

Doctor of Philosophy

Supervisors

Prof. Carlo Baccigalupi
Prof. Andrea Lapi
Dr. Balakrishna S. Haridasu

Candidate

Yacer Boumechta

Contents

Abstract

For the last century, General Relativity (GR) has been successful in explaining several phenomena which were not explained before, for instance, the perihelion precession of Mercury, the bending of light due to the gravitational field, and the prediction of Gravitational Waves (GWs). Nevertheless, GR fails to explain some of the most important phenomena in the universe, namely the Dark Energy (DE) component, and inflation. Therefore, an extension to its original framework should be adopted. There are many ways to modify GR in a way to explain the cosmological observations, among them, one of the first and trivial modification to GR is the introduction of the Cosmological Constant (CC) Λ to the original theory which can predict the accelerated expansion rate of the universe. However, this modification does not explain the origin of DE and therefore another modification is required. Moreover, the homogeneity and the flatness of the universe cannot be predicted by a mere GR theory, an early time modification to GR to contain additional scalar field called the inflation which through slow rolling can predict the homogeneity and the flatness we observe in today's cosmology. Some of the attempts to modify GR in order to account for the DE component include $f(R)$ gravity which are a class of models where the Ricci scalar R in the Lagrangian of the original GR is modified with another scalar function ($f(R)$) which represents a generalization instead of simply adding one constant Λ. Another alternative is represented by the Quintessence, which instead of a constant DE, it assumes a dynamical one through an addition of a scalar field. Our focus however, will be on a specific type of modification to GR which is represented by the Chameleon Gravity, which introduces a new scalar field, too, which locally behaves as GR but at the large scales it modifies GR and account for the constant DE, represented by Λ.

There are different manners to investigate manifestations of MG in cosmology, involving CMB and LSS. In this Thesis, we bring the analysis of manifestations of specific MG scenarios in the largest cosmological objects, namely galaxy clusters, taking the advantage of new datasets which became available recently. The Thesis is divided in two parts. First, we review GR

and general cosmology, derived from the Einstein's field equations including a cosmological constant and a Cold Dark Matter Component, represented by particles which were non-relativistic at their time of decoupling, interacting at most weakly with the rest of the system, the ΛCDM model. We conclude the first part by introducing Modified Gravity (MG) in a general context, which is then specialized to the specific case of Chameleon Gravity (CG) and $f(R)$ theories. The second part consists of studying the CG phenomenology in cluster of galaxies, which can now be inspected as potential carriers of MG signature, thanks to new datasets. In particular, we study how CG affects the hydrostatic pressure within the cluster which is then used to find unprecedented constraints on the model. In addition, in the following chapters, we extend the analysis by including clusters in tension with the assumption of a Navarro Frenk and White (NFW) CDM halo, solving semi-analytical the CG field equations in relation to their mass model. A concluding chapter sums up the main parts of the Thesis, the results obtained so far, and the future prospects.

List of Publications

[1] *Mass modeling and kinematics of galaxy clusters in modified gravity*; L. Pizzuti, **Y. Boumechta**, S. Haridasu, A. Pombo, S. Dossena, M. A. Butt, F. Benetti, C. Baccigalupi, and A. Lapi, JCAP 11 (2024) 014.

[2] *Caustic and hydrostatic mass bias: Implications for modified gravity*; M. A. Butt, B. S. Haridasu, **Y. Boumechta**, F. Benetti, L. Pizzuti, C. Baccigalupi, and A. Lapi, Phys. Rev. D 109, 064006 (2024).

[3] *Dark Matter in Fractional Gravity III: Dwarf Galaxies Kinematics*; F. Benetti, A. Lapi, G. Gandolfi, M. A. Butt, **Y. Boumechta**, B. S. Haridasu, and C. Baccigalupi, Universe 9, 478 (2023).

[4] *Constraining Chameleon screening using galaxy cluster dynamics*; **Y. Boumechta**, B. S. Haridasu, L. Pizzuti, M. A. Butt, C. Baccigalupi, and A. Lapi, Phys. Rev. D 108, 044007 (2023).

Acknowledgments

I would like to express my gratitude to everyone who made this thesis possible, starting with my supervisors, Carlo Baccigalupi, Andrea Lapi, and Sandeep Haridasu, for their constant supervision, full support, and understanding throughout my PhD journey.
I am also grateful to the MG group at SISSA (my supervisors, Minahil Butt, and Francesco Benetti), which was founded when my first project began, and which grew as more students joined. This provided a sense of continuity to our ideas and made the topics more diverse. I hope that the spirit of collaboration continues in the future and that more people become interested in our research activities.
I would like to express my gratitude to Paolo Creminelli for his support and assistance during the Diploma Program at ICTP and throughout my PhD.
A special thanks to Lorezzo Pizzuti, our main collaborator outside of SISSA, for his work and the insightful discussions during my PhD years.
I also want to thank all the SISSA and ICTP professors for providing one of the best working and learning environments a physicist could dream of, from the pedagogical programs to the quality of research and facilities.

وَفَوْقَ كُلِّ ذِى عِلْمٍ عَلِيمٌ

but over every possessor of knowledge is one more knowing.
(Quran 12:76)

إلى عائلتي، أمي، أصدقائي، و كل من علمني شيئا...

إلى جدي عمر و جدتي علجة من أحباني و دعماني منذ صغري و لم يتمكنا من رؤيتي أتخرج...

To my Family, my Mother, my Friends, and anyone who taught me something...
To my dear grandparents Amar and Alja who supported me since I was a kid and didn't make it to see me graduate...

Notations

Here, we provide a brief guide to the notation and a list of acronyms.

$c = 1$	the speed of light is set to be equal to one;
G	Newtonian Gravitational Constant;
m_{pl}	Planck mass;
$M_{\rm Pl}$	reduced Planck mass;
$(-,+,+,+)$	metric signature;
$i, j, k...$	3D spatial indices in vectors and tensors;
$\mu, \nu, \gamma...$	4D indices in vectors and tensors;
$g_{\mu\nu}$	metric tensor;
g	determinant of the metric tensor $g_{\mu\nu}$;
H	Hubble parameter in cosmic time t;
$R_{\mu\nu}, R$	Ricci tensor and its trace;
$T_{\mu\nu}, T$	Stress energy tensor and its trace;
$G_{\mu\nu}$	Einstein Tensor ($G_{\mu\nu} = R_{\mu\nu} - 1/2 g_{\mu\nu} R$);
ϕ	Scalar field;
χ_m	Matter fields;
S_m	Matter action of all matter fields, χ_m;
∇_μ	Covariant derivative;
∇^2	Spatial covariant derivative;
Λ	Cosmological Constant;

Acronyms

ΛCDM	Lambda Cold Dark Matter;
CC	Cosmological Constant Λ;
DM	Dark Matter;
CDM	Cold Dark Matter;
GR	General Relativity;
EFE	Einstein's Field Equations;
CG	Chameleon Gravity;
FLRW	Friedmann-Lemaître-Robertson-Walker metric;
DE	Dark Energy;
MG	Modified Gravitational Theory;
LSS	Large Scale structure;
WMAP	Wilkinson Microwave Anisotropy Probe;
C.L.	Confidence Limits;
CMB	Cosmic Microwaves Background radiation;
MCMC	Markov Chain Monte Carlo;
l.h.s	Left hand side;
r.h.s	Right hand side;
w.r.t.	With respect to.

Part I

Introduction

Chapter 1

General Relativity

After the success of the Special Theory of Relativity as it was introduced by Albert Einstein in 1905 [5], and specifically for its applications in the context of uniformly accelerated frame of references which are equivalent to local gravitational fields, it was realized that the latter affect the flow of time and, therefore, a relativistic theory of gravity was needed [6, 7, 8]. Sin free fall, there is no external force, indicating that gravitational fields can be locally canceled out by uniform acceleration. This is what is referred to as *Equivalence Principle* [6, 9, 10].
Moreover, In Special Relativity, the Minkowski spacetime[11, 12] is a vector space defined on a flat four-dimensional spacetime that permits to define the algebra of Special Relativity. Special Relativity, starting from a kinematic and dynamical extension of Newtonian physics, became a theory where space and time are interconnected in what we call spacetime. In order to identify accelerations as a manifestation of gravity, spacetime has to bend accordingly, i.e. it is curved.

A curved spacetime requires the use of the Riemannian geometry, and the corresponding theory was put forth in 1915 and it is, so far, the most successful theory that describes gravity[13, 14].
GR has been successful in predicting phenomena which were not predicted in the context of Newtonian gravity, for instance, the perihelion precession of mercury [15], gravitational lensing, i.e. bending of light due to the gravitational field of a massive object [16, 17], and the existence of GWs. [18, 19, 20].
GR dynamics relies on field equations coupling curvature with energy. Under the assumptions of homogeneity and isotropy, they can be applied to study the evolution of the universe, which is the basis for the successful big bang theory and the ΛCDM cosmology[21, 22], providing a precise description of the history of the universe [23].
This Chapter will be a brief introduction to the framework of GR with the

most important results that are going to be used throughout the thesis. We start in section 1.1 by defining the elements of geometry f General relativity, followed in section 1.2 by kinematics and dynamics derived from the Einstein-Hilbert action. Finally, we conclude in section 1.4 by discussing possible modification(s) to General Relativity.

1.1 Spacetime geometry

GR cannot be formulated without the understanding of its essential cornerstone, i.e., spacetime geometry. It is defined on a four-dimensional spacetime Manifold (without going into details, a manifold is simply a curved space which is locally flat, for more details, please refer to [24, 25]). The essential feature of the spacetime is the metric $g_{\mu\nu}$, which is basically a tensor defined in a way to measure distances. Locally this metric can be diagonalized, and through a finite number of coordinate transformations it can be transformed into the Minkowski metric $\eta_{\mu\nu} = diag(-1, 1, 1, 1)$ [26, 27, 28]. It is useful to construct an invariant quantity that involves the metric; For a given coordinate system x^μ, the metric element ds^2 is then defined as

$$ds^2 = g_{\mu\nu} dx^\mu dx^\nu, \tag{1.1}$$

where, we can also define the proper time which is the time a local observer measures between two events. This time is invariant and can be related to the metric element by $d\tau^2 = -ds^2$.

1.2 Kinematics

GR is a geometry based theory that considers gravity not as a force but rather as a manifestation of spacetime curvature due to existence of a matter source. In Newtonian physics, bodies with no acting force on them follow a straight line trajectory which are the geodesics of a flat geometry. On the other hand, following the same principle, freely falling bodies in GR follow geodesics in a curved spacetime, which are by definition the trajectories that corresponds to the least "distance" between two points, or in the case of the space time, the one that follows the least amount of proper time:

$$\tau = \int (-g_{\mu\nu} dx^\mu dx^\nu)^{1/2}. \tag{1.2}$$

By choosing the minimum proper time, the geodesic equation for a freely falling particle following the world line[1] $x^\mu(\tau)$ in a spacetime characterized

[1] A World line is the trajectory a particle follows in spacetime.

by the metric $g_{\mu\nu}$ is

$$\frac{d^2x^\mu}{d\tau^2} + \Gamma^\mu_{\alpha\beta}\frac{dx^\alpha}{d\tau}\frac{dx^\beta}{d\tau} = 0, \tag{1.3}$$

where τ is the proper time and $\Gamma^\mu_{\alpha\beta}$ is the Christoffel symbol which for GR is given by $\Gamma^\mu_{\beta\alpha} = \Gamma^\mu_{\alpha\beta} = \frac{1}{2}g^{\mu\lambda}(\partial_\alpha g_{\beta\lambda} + \partial_\beta g_{\alpha\lambda} - \partial_\lambda g_{\alpha\beta})$ [26]. The geodesic equation can be rewritten in terms of the Four-velocity vector $U^\mu = \frac{dx^\mu}{d\tau}$ which yields

$$U^\alpha \nabla_\alpha U^\mu = 0, \tag{1.4}$$

where we have utilized the definition of covariant derivative $\nabla_\alpha U^\mu = \frac{\partial U^\mu}{\partial x^\alpha} + \Gamma^\mu_{\alpha\beta}U^\alpha$, this can also be written in terms of the Four-momentum $P^\mu = mU^\mu$, such that

$$P^\alpha \nabla_\alpha P^\mu = 0. \tag{1.5}$$

This is a very useful way of expressing the geodesic trajectory as we are going to use it later on in the context of cosmology to determine the trajectories of particles in an Friedmann–Lemaître–Robertson–Walker (FLRW) metric [29, 30, 31, 32, 33, 34].

1.3 Einstein Hilbert action

One can formulate the field equations in GR through a single action (S), which is the Einstein-Hilbert action, written as

$$S = \frac{1}{8\pi G}\int R\sqrt{-g}d^4x + S_m(g_{\mu\nu}, \chi_m), \tag{1.6}$$

where G is the gravitational constant, R is the Ricci scalar, g is the determinant of the metric tensor $g_{\mu\nu}$, and $S_m(g_{\mu\nu}, \chi_m)$ is the matter action that is minimally coupled to gravity. The field equations can be obtained by imposing $\frac{\delta S}{\delta g_{\mu\nu}} = 0$. That is to insure the equivalence principle which states that the physics should not change by locally changing the frame of reference. This leads to

$$\frac{1}{16\pi G}\int \left[\frac{\delta R}{\delta g^{\mu\nu}}\sqrt{-g} + R\frac{\delta\sqrt{-g}}{\delta g^{\mu\nu}}\right] d^4x + \frac{\delta S_m}{\delta g^{\mu\nu}} = 0. \tag{1.7}$$

Since $\frac{\delta R}{\delta g_{\mu\nu}} = R_{\mu\nu}$, and $\frac{\delta\sqrt{-g}}{\delta g^{\mu\nu}} = -\frac{1}{2}g_{\mu\nu}\sqrt{-g}$, we get

$$R_{\mu\nu} - \frac{1}{2}Rg_{\mu\nu} = -8\pi G\left[\frac{2}{\sqrt{-g}}\frac{\delta S_m}{\delta g^{\mu\nu}}\right]. \tag{1.8}$$

Moreover, following [35], we get

$$T_{\mu\nu} = -\frac{2}{\sqrt{-g}}\frac{\delta S_m}{\delta g^{\mu\nu}}, \tag{1.9}$$

and

$$R_{\mu\nu} - \frac{1}{2}Rg_{\mu\nu} = 8\pi G T_{\mu\nu}. \tag{1.10}$$

These are the equations determining dynamics in GR, also known as Einstein Field Equations (EFE). Note that the Einstein tensor, i.e, $G_{\mu\nu} = R_{\mu\nu} - \frac{1}{2}Rg_{\mu\nu}$ has the property $\nabla^\mu G_{\mu\nu} = 0$ which translates to

$$\nabla^\mu T_{\mu\nu} = 0. \tag{1.11}$$

The last equation is simply the analogous form of the continuity and the conservation equations in curved spacetime, and it is going to be a useful identity to use later on.

1.4 Trivial modification to General Relativity

It is quite obvious to ask the question: is the action defined in eq. (1.6) unique? In other words what changes can we make to the Lagrangian while retaining the properties of eq. (1.10). Naively, adding any term proportional to the metric tensor $g_{\mu\nu}$ to eq. (1.10) will have the same symmetries and properties of the stress energy tensor $T_{\mu\nu}$. Which can be written for instance as

$$R_{\mu\nu} - \frac{1}{2}Rg_{\mu\nu} + \Lambda g_{\mu\nu} = 8\pi G T_{\mu\nu}. \tag{1.12}$$

In terms of the action, adding a surface term and any other term that is proportional to the metric will lead to the same field equation [36, 37], i.e., we can safely add a proportional term to the metric in eq. (1.6) and the theory will still be consistent with GR principles. However, as this new term will appear in the field equations, it surely will give kinematics depending on the nature of the constant. Therefore, adding such a constant must be justified as we are going to see in the next Chapter. This addition may look like a modification of GR but in fact it falls in the same GR category since there was no addition to GR principles or violation to any of them. A modification to GR would include the following new features [38]:

- Non minimal coupling between gravity and other objects in the action,
- higher order curvature terms,
- additional fields in the action,
- Extra dimensions.

These are ways to modify GR implying different properties and dynamics, so that, according to [39, 40, 41, 42, 43], simply adding a constant is a modification of EFE, but not a truly different theory. Throughout the Thesis, we will focus on adding an additional field and non minimal coupling as we are going to study in detail in the MG chapter.

Chapter 2

Cosmology

Cosmology has been a point of interest for thinkers for centuries, starting from ancient epochs in Greece with the Ptolemy geocentric model[44], where the Earth is located at the center and the Sun and the planets rotating around it, with the stars belonging to an outside sphere equally distant from the Earth. This model, which was purely based on naked eye observations, persisted for centuries, even in the civilizations that followed. Later on in the 16th century, Copernicus [45] suggested the heliocentric model for the first time, a picture which Galileo substantiated later with the observation of the Jupiter's moons which meant that there are celestial objects rotating other planets rather than Earth[46]. Subsequently, in the 17th century, based on Tycho Brahe's astronomical observations about the positions of the planets in the night sky[47], Johannes Kepler formulated the first laws that governs the motion of planets around the Sun, but these laws were purely based on observations but not a result of laws of physics[48, 49]. Isaac Newton using the gravitational law of attraction and the laws of dynamics, could explain the Kepler's laws and provide a firmer understanding of the gravitational force that governs celestial objects through actual fundamental physics principles[50].

By 1915, as GR was formulated [51], the study of the universe and its evolution became possible due to the nature of the theory, which provided an understanding of the cosmos, its geometry, matter content, and evolution through gravitational interactions, including components from compact objects like stars and black holes to galaxies and galaxy clusters.as Einstein's theory developed, many solutions were proposed within cosmology. For instance, Willem de Sitter proposed a model where the universe contains only a Λ term (cosmological constant), which causes it to accelerate exponentially [52]. However, after Hubble's 1929 discovery that the galaxies are receding from each other [53], it has become clear that the universe is, in fact, expand-

ing and not static, an occurrence which Einstein had tried to impose in his equations, by introducing precisely the cosmological constant [36]. He later called this his "Biggest Blunder" [54], as it turned out that the universe is not static but rather dynamic and expanding exponentially in time. The most successful model among these was represented by the work done by Alexander Friedmann, Georges Lemaître, Howard P. Robertson and Arthur Geoffrey Walker, who adopted the 'cosmological principle' [29, 30, 31, 32, 33, 34] assuming that the universe is both homogeneous and isotropic, although at that time this assumption was not backed by observations. Later, through the large surveys conducted, notably the Cosmic Microwave Background (CMB) [55, 56, 57], we now know that this assumption is valid on large scales, and the proposed model remains the most successful one.

The ΛCDM, also known as the Cosmological Concordance Model is supported by observational evidence. It is based on GR and the cosmological principle, along with the existence of a cosmological constant (Λ) which drives the acceleration of the universe at late times. It acts like a form of fluid with negative pressure that pushes outward against inward gravitational pull, and includes CDM, which, as we anticipated, includes particles interacting at most weakly with those of the Standard Model of Particle Physics, and decoupled from their thermal equilibrium in the early universe when they were non-relativistic. This concept of particles was first introduced in 1933 by Fritz Zwicky[58], who observed that the visible mass in the Coma cluster was insufficient to explain its gravitational effects. Later, Vera Rubin and Kent Ford's observations of galaxy rotation curves provided robust evidence for CDM, as outer stars in galaxies moved faster than expected from visible matter alone[59]. Later studies including gravitational lensing, CMB analysis, and large scale structure surveys[60], confirmed CDM as a critical component of the universe's mass energy content.

This Chapter is divided as follows: in section 2.1 , we review the geometrical consequences of the cosmological principle in cosmology, specifically the metric corresponding to a homogeneous and isotropic universe. In section 2.2, we model the matter component of the universe in a single stress energy tensor by relying on the same assumptions and symmetries. Consequently, in section 2.3 since we have all the geometrical and the matter ingredients, we can proceed and solve the Einstein's field equations, i.e, the Friedmann equations and have some comments on the nature of the solutions and their behavior. Furthermore, in section 2.4, we briefly review the ΛCDM model, concluding in section 2.5 with a discussion on the nature of the DE.

2.1 The Cosmological Principle and the FLRW metric

The Cosmological principle is a key feature of cosmology, stating that the universe is both homogeneous and isotropic in the large scales, surpassing hundreds of millions of light years.The former ensures that on a sufficiently large distance, the universe will look the same for any observer, while the latter means that while looking at the universe from a certain location, there will be no preferred directions. This implies that an inhomogeneity and the anisotropy appear only in small scales.

Between the 1920s and 1930s, Friedmann, Lemaître, Robertson, and Walker independently proposed a form for the metric $g_{\mu\nu}$ [29, 31, 32, 34] that aligns with the Cosmological Principle for use in Einstein's equations. This metric remains the most effective way to describe the evolution of the Universe. Since then, numerous cosmological models have been developed based on this metric as we are going to see later in Section 2.4. Another metric that was proposed is the The Lemaître Tolman Bondi (LTB) metric [61, 37, 62] which describes a spherically symmetric, inhomogeneous universe. It models a universe with a radially varying density, allowing for the possibility of local density fluctuations such as voids or over densities. The LTB metric is often used in cosmology to study structures like galaxy clusters and large scale inhomogeneities in the cosmological expansion. It generalizes the FLRW metric by allowing for inhomogeneities without assuming a uniform density.

Unlike in the beginning of the past century, at present there are numerous observational evidences for the cosmological principle, showing that the universe at the large scale contains structures which are gathered into galaxy groups, clusters of galaxies, super clusters, etc. Also, the CMB which fills the entire sky with a radiation with temperature of $T_{\text{CMB}} \simeq 2.725K$ [63] offers the a direct evidence for the cosmological principle showing that the universe, since the radiation comes with the same intensity from all directions of the sky.

Let us first write down the metric element in a general way, where the index i runs only through the space coordinates and t is the time coordinate,

$$ds^2 = g_{00}dt^2 + 2g_{0i}dtdx^i + g_{ij}dx^i dx^j. \tag{2.1}$$

We can choose $g_{00} = -1$ by introducing the concept of cosmic time, t. Furthermore, the isotropy implies two things : since the second r.h.s term would have different values for the same line element in opposite directions which

contradicts the isotropy, thus $g_{0i} = 0$. The second one, is due to isotropy, fixing the radial component at a time t should have spherical symmetry, which implies $g_{ij}dx^i dx^j = a(t)^2 \left[f(r)dr^2 + r^2 d\Omega^2\right]$ where $d\Omega$ is the solid angle and a(t) is the scale factor which is the only degree of freedom which is left to dynamics because of the homogeneity and isotropy. Spatially, instead, the function $f(r)$ is determined by the fact that due to homogeneity all observers should measure the same curvature all over space (spatially independent Ricci scalar) , and therefore the three dimensional curvature should be a constant, which eventually fixes the function $f(r) = \frac{1}{1-kr^2}$, which eventually leads to

$$ds^2 = dt^2 - a^2(t)\left[\frac{dr^2}{1-kr^2} + r^2 d\Omega^2\right], \tag{2.2}$$

where k is the curvature parameter which can assume any value, which we represent as

$$k = \begin{cases} < 0 & H^3, \\ 0 & E^3, \\ > 0 & S^3. \end{cases}$$

H^3 corresponds to the negative curvature, E^3 to the null curvature or a flat space, and S^3 to the positive curvature.

We can introduce the FLRW metric by referring to a key component in the kinematics cosmology, that is the Hubble Constant or the Hubble parameter H. But before doing that, let us see how a particle behaves in an expanding universe. For a particle with Four momentum P^μ, we know that from homogeneity that $\frac{\partial P^\mu}{\partial x^i} = 0$, which when replaced into the geodesic equation given in eq. (1.5) will give

$$P_0 \frac{dP^0}{d\tau} + \Gamma^0_{ij} P^i P^j = 0, \tag{2.3}$$

while the other terms vanish [64]. It is easy to show that $\Gamma^0_{ij} = -a\dot{a}\gamma_{ij}$, where γ_{ij} is the comoving part of the spacial FLRW metric, i.e, $ds^2 = -dt^2 + a(t)^2\gamma_{ij}dx^i dx^j$.
We know that the momentum is given as $p^2 = g_{ij}P^i P^j = a^2\gamma_{ij}P^i P^j$[1], combined with the fact that $E^2 - p^2 = m^2$. Thus eq. (2.3) becomes

$$\frac{\dot{p}}{p} = -\frac{\dot{a}}{a}, \tag{2.4}$$

[1]Please note, this is not to be confused with the pressure of the individual components, which is also labeled with p.

which after solving finally gives

$$p \propto \frac{1}{a}. \tag{2.5}$$

We can now define the Hubble parameter as

$$H(t) = \frac{\dot{a}}{a}, \tag{2.6}$$

Let's consider a galaxy emitting a photon at a wavelength λ_{em} at a scale factor $a_{em} = a(t_{em})$ while it is received by an observer on the earth at a wavelength λ_0 at a scale factor $a_0 = a(t_0)$. The Redshift is defined as

$$z = \frac{\lambda_{em} - \lambda_0}{\lambda_0}, \tag{2.7}$$

which can be written differently with the help of eq. (2.5) and gives

$$z = \frac{a_0}{a_{em}} - 1. \tag{2.8}$$

Assuming that the emitting and the observing points are not far enough for the scale factor to grow significantly, thus we can Taylor expand around the current time, which gives

$$a_{em} \simeq a_0 + (t_{em} - t_0)\dot{a}_0, \tag{2.9}$$

which, after being included into eq. (2.8), gives $z = (t_0 - t_{em})H_0$. For time intervals in which the universe has not been expanding significantly, we can assume that the distance between the emission and the observation points is $d = t_0 - t_{em}$, where again c has been assumed to be 1. Therefore, we finally get

$$z = dH_0, \tag{2.10}$$

Which is known as the Hubble law, introduced by Edwin Hubble in 1929 [53], who found that the emission spectra of nearby galaxies is redshifted, which indicate that they are receding away from each other as opposed to what is expected due to the gravity, leading to the concept of cosmological expansion. By plotting the redshift of galaxies against their distance, Hubble discovered a linear relationship: the farther a galaxy is from us, corresponding to the Hubble law.

The expression in eq. (2.2) defines the spacetime metric throughout the universe at a given time t, which also reveals the l.h.s of eq. (1.10). We now address the concept of Stress-energy tensor $T_{\mu\nu}$.

2.2 The Stress-energy tensor

The stress-energy tensor as defined in eq. (1.9) is a conserved symmetric tensor (since $g_{\mu\nu}$ is symmetric). According to the Cosmological Principle, The large scale structure of the universe is homogeneously distributed, thus we can say that matter is approximately homogeneously distributed which implies that the evolution of density and the pressure of different components depends only on time. Cosmology is of course affected by perturbations which deviate from homogeneity and isotropy. Perturbations are thought to be originated in the early Universe, during Inflation, in the linear perturbative regime, later on growing in observed structures. We do not give a complete description of those in this Thesis, referring to other works [65, 66, 67, 68]. In order to describe the large scale evolution of the universe we can imagine the galaxies to be small grains, stationary in the comoving frame, i.e. the one at rest with respect to the cosmological expansion, which can be described by the perfect fluid stress energy tensor

$$T_{\mu\nu} = (\rho + P)U_\mu U_\nu + P g_{\mu\nu}, \tag{2.11}$$

where ρ, P are respectively the total energy densities and the pressure, while U_μ is the four velocity of the fluid. We now apply the conservation equation eq. (1.11) to the case of FLRW. Consider a comoving frame that is defined with the four velocity as

$$U^\mu = (1, 0, 0, 0). \tag{2.12}$$

By substituting that into eq. (2.11) we get the conditions

$$T_{00} = \rho, \quad T_{ii} = a^2 P, \quad T_{0i} = 0, \tag{2.13}$$

which can be written as a single Matrix:

$$T^\nu_\mu = \begin{pmatrix} -\rho & 0 & 0 & 0 \\ 0 & P & 0 & 0 \\ 0 & 0 & P & 0 \\ 0 & 0 & 0 & P \end{pmatrix}. \tag{2.14}$$

By substituting into eq. (1.11) we finally have

$$\dot{\rho} + 3\frac{\dot{a}}{a}(\rho + P) = 0. \tag{2.15}$$

Depending on the matter component, eq. (2.15) shows the evolution of each cosmological species as a function of the scale factor $a(t)$. By considering the equation of state $P = \omega\rho$, the solution to eq. (2.15) gives:

$$\rho \propto a^{-3(1+\omega)}. \tag{2.16}$$

For instance in the case of radiation the following condition holds: $P = \frac{1}{3}\rho$, which leads to:

$$\rho_r \propto \frac{1}{a^4}. \tag{2.17}$$

This result is intuitive, as the dilution of energy in radiation, in addition to the volume, decreasing as $1/a^3$, includes an extra $\frac{1}{a}$ (see section 2.1), due to the wavelenght stretch.
In the case of non-relativistic fluid(s) ($P = 0$), such as the CDM, the density scales as

$$\rho_m \propto \frac{1}{a^3}, \tag{2.18}$$

as no extra redshift in the mass is present.

2.3 Friedmann equations

We now consider the dynamics of the FLRW universe using eq. (1.10), the metric in eq. (2.2) and the stress-energy tensor in eq. (2.11). Two equations are derived, corresponding to

$$H^2 = \frac{8\pi G}{3}\rho - \frac{k}{a^2}, \tag{2.19}$$

$$\frac{\ddot{a}}{a} = -\frac{4\pi G}{3}(\rho + 3P). \tag{2.20}$$

Note that eq. (2.19) combined with eq. (2.15) gives eq. (2.20) and therefore we have two sets of equations but three unknown ($a(t)$, ρ, and P) therefore we need another equation to find a full solution, which is commonly taken from the equation of state $P = \omega\rho$. Note that ρ and P are the total density and pressure summed over all types of cosmological constituents

$$\rho = \sum_i \rho_i, \quad P = \sum_i P_i, \quad P_i = \omega_i \rho_i, \tag{2.21}$$

where ρ_i , P_i, and ω_i are the density, pressure, and the equation of state defined for each component. The critical density is then defined as

$$\rho_c = \frac{3H^2}{8\pi G}, \tag{2.22}$$

and at the present time it is

$$\rho_c^0 = \frac{3H_0^2}{8\pi G} \simeq 2.8 \times 10^{11} h^2 M_\odot \mathrm{Mpc}^{-3}, \tag{2.23}$$

where $h = H_0/100\,\mathrm{km\,s^{-1}\,Mpc^{-1}}$. We can rewrite eq. (2.19) as

$$\frac{k}{(Ha)^2} = 1 - \frac{\rho}{\rho_c}, \tag{2.24}$$

which will result in 3 cases:

$$\begin{aligned} &\rho < \rho_c \to k > 0 \quad \to \quad \text{closed universe} \\ &\rho > \rho_c \to k < 0 \quad \to \quad \text{open universe} \\ &\rho = \rho_c \to k = 0 \quad \to \quad \text{flat universe.} \end{aligned} \tag{2.25}$$

Consider now Λ whose density does not change as the universe expands, from eq. (2.15) it is clear that $\omega_\Lambda = -1$, this component is what we refer to as cosmological constant providing, in the ΛCDM cosmology, a DE driven late time acceleration [69]. Thus, eq. (2.24) can be written simply as

$$\Omega_m + \Omega_r + \Omega_\Lambda + \Omega_k = 1, \tag{2.26}$$

where the fractional densities $\Omega_i = \frac{\rho_i}{\rho_c}$ and $\Omega_k = \frac{k}{(Ha)^2}$. We can now find the time dependent solutions for each component separately by considering different eras where each component is dominant, this is possible because the evolution of each species scales differently w.r.t the scale factor. First let's consider a radiation dominated era, which, in the current picture of cosmology, preceeds the matter dominated era. As we pointed out, from eq. (2.15) we've $\rho_r \sim 1/a^4$, and substituting it back in eq. (2.19), gives the solution

$$a \propto t^{1/2}, \quad H = \frac{1}{2t}. \tag{2.27}$$

Second, following the same approach, we can show that the time dependent solution to the matter dominated era are

$$a \propto t^{2/3}, \quad H = \frac{2}{3t}. \tag{2.28}$$

Finally, in an DE dominated era, the density is constant, implying that the Hubble constant also remains unchanged, as it is straightforward from eq. (2.19), and the solution is given as

$$a \propto e^{Ht}, \quad H = \sqrt{\frac{8\pi G}{3}\rho_\Lambda}. \tag{2.29}$$

If we fix the scale factor at the current time to unity ($a_0 \equiv a(t = t_0) = 1$), the Friedmann equation can be written as

$$H^2 = H_0^2 \left[\Omega_{r,0} a^{-4} + \Omega_{m,0} a^{-3} + \Omega_{k,0} a^{-2} + \Omega_{\Lambda,0}\right]. \tag{2.30}$$

where $\Omega_{i,0} = \frac{\rho_{i,0}}{\rho_{c,0}}$ for each component, and the index "0" indicates that we evaluate the density parameter Ω at the current time. The quantities defined in the equation above are known as cosmological parameters. They are constrained by observations, of the CMB, large scale structure through their manifestations in the cosmological expansions, as well as cosmological perturbations, see [70, 71] and references therein. Within 68% confidence level, the measures are

$$\begin{aligned} \Omega_{m,0} &= 0.315 \pm 0.007, \\ \Omega_{b,0}h^2 &= 0.0224 \pm 0.0001, \\ \Omega_{c,0}h^2 &= 0.120 \pm 0.001, \\ \Omega_{\Lambda,0} &= 0.685 \pm 0.007, \\ \Omega_{k,0} &= 0.0007 \pm 0.0019, \\ H_0 &= 67.4 \pm 0.5 \text{ km s}^{-1} \text{ Mpc}^{-1}. \end{aligned} \tag{2.31}$$

The second and the third values represent the abundances of Standard Model Particles and CDM, respectively.

2.4 ΛCDM

As we discussed so far, the ΛCDM model is the prevailing model that is mostly successful in describing the large scale structure and the background evolution of the universe. It describes cosmological geometry, compositions and its evolution since the Big Bang. In summary, the essential components of the ΛCDM are:

- **Λ or DE - Dark Energy**: Λ is the cosmological constant, or equivalently the Dark energy (see Section 2.5). It drives acceleration in the expansion, opposite to the gravitational attraction[72, 73].
- **CDM - Cold Dark Matter**: it is a form of matter that interacts at most weakly with particles of the Standard Model of Particle Physics, and is main evidence is therefore through gravitational effects, "Cold" refers to the relatively negligible velocity of this matter compared to the speed of light since the time in which these particles decoupled from the thermal bath in the Early Universe. This form of matter is a necessary component in the structure formation as it provides the gravitational scaffolding for ordinary matter to form galaxies and structure of galaxies.

- **Particles in the Standard Model**: This form of matter is the one we observe in the universe, which we can also reproduce in laboratories on Earth. In cosmology it is misleadingly named "baryonic", only because it it, baryons dominate in terms of mass. It accounts for stars in galaxies, cluster of galaxies, and unprocessed gas in the interstellar and inter-Galactic media.

As we have seen, current observations [70] indicate that our universe at the present time is dominated by DE with $\Omega_\Lambda = 0.68$. Non-relativistic matter has $\Omega_{m,0} \sim 0.31$, and radiation $\Omega_{r,0} \sim 4.1 \times 10^{-5} h^2$[2]. The curvature contribution is $|\Omega_k| < 0.01$, and since it scales as a^{-2}, it becomes negligible at earlier times compared to matter and radiation. Furthermore, Inflation dilute any initial curvature[75, 76, 77], to the current limits in which CMB measurements indicate that the universe is effectively flat within errors. Thus, $\Omega_k = 0$ is assumed in the ΛCDM. It is also worth noting that the matter component is primarily composed of $\Omega_{\mathrm{CDM},0} = 0.27$, with baryonic matter representing $\Omega_{\mathrm{b},0} \simeq 0.04$.

2.5 Nature of Dark Energy

DE has been the last cosmological component, added into eq. (2.30) as a mere consequence of observations, namely the acceleration of the universe. As we can see from the second Friedmann eq. (2.20), in the case of a universe with only radiation and matter the r.h.s is negative and therefore the expansion acceleration is negative and vanishes asymptotically which does not match with the data. However, if at a late time the universe is dominated by a form of DE, the acceleration becomes positive, as indicated by observations. In term of a pure cosmological constant playing the DE role, that can be seen as a geometrical component in the Einstein field equation given by the version in eq. (1.12) where $\Lambda = 8\pi G \rho_\Lambda$. On the other hand, there are two well known theoretical problems associated to the simple explanation of the cosmic acceleration through a cosmological constant. One is represented by the coincidence, meaning why the DE, having a constant energy density, is comparable to the non-relativistic component at recent epochs. The other is the fine tuning, meaning why in the early universe it was so small with the density of other components. As an attempt to address these problems, DE generalizes the concept of a cosmological constant, in a new component with negative pressure ($P = -\rho$) which dynamically evolve, and also can develop its own linear perturbations. This brings up more hypotheses, could

[2]Here the radiation density is constituted both by photons and neutrinos [74].

DE come from a much deeper theory of gravitation which accounts for its observed phenomenological effect? [78].

That is the subject of the next Chapter where we are going to review some modification to GR which attempt to account for the dark energy with more focus on Chameleon Gravity and $f(R)$ theories.

Chapter 3

Modified Gravity

As we explained in previous Chapters, GR has theoretical and observational shortcomings that lead to considering MG theories [79, 80, 81, 82, 83]. Although it has proven to be remarkably effective in describing gravity in a variety of contexts, such as solar system experiments [84, 85] and observations of GWs[20, 18], it faces considerable challenges [86], such as the existence of singularities as those predicted at the center of a black hole, violating the equivalence principle [87, 88]. This might be a reflection of the fact that GR could be an effective theory.
Another reason why MG should be taken into consideration is the fact that GR has not been extensively tested across all scales [89]. For example, Yukawa potential correction to the Newtonian law is neglected, as it was shown in [90], for distances of order $10\mu m$. GR validity outside of these domains is still a work in progress, and further observations are ongoing to probe potential MG scenarios [80].

The latter could produce observable corrections in the vicinity of black holes or in the early universe, or on cosmological large scales. Therefore, MG theories suggest different approaches to gravity which could be tested and provide an in depth understanding of gravity in different regimes. Within the ΛCDM model itself, dark matter and dark energy components are postulated, and since they have not been directly observed other than through their manifestations through gravity, their nature is still a mystery. This motivated the idea that large scale modification to GR is responsible for the accelerated expansion in cosmology, without the introduction of a DE component.
In summary, there are theoretical motivations, as well as observational evidences, which allow to challenge GR in its current formulation. In the next Section we review the main category of MG scenarios, and described the breakdown of the current chapter, which contains the definition of MG sce-

narios to be investigated in the Second part of this work.

3.1 Different MG approaches

MG scenarios can be classified in various manners, including the modifications in the Einstein-Hilbert action eq. (1.6), which involves introducing new fields or parameters, higher dimensions, or even new functions of the curvature tensor. Some of the approaches intend to tackle the strong regimes, i.e., black holes, while others attempt to explain weak regimes, namely, at the cosmological scales.

One approach to modify GR is assuming that the action contains higher order functions of the Ricci Scalar. For instance, Gauss-Bonnet gravity [91] introduces quadratic terms in the Ricci scalar and Ricci tensor in the action which in return provide higher term corrections to the strong gravity regime. This leads to more complex equation of motions but also it may help explaining the structure of black holes and the early universe accelerated expansion [92].

Another MG approach consists in introducing extra fields in the theory [93, 94, 95, 96]. Unlike GR, which assumes that the metric tensor fully describes the geometry of spacetime that appears as gravity, many MG theories assume the existence of extra fields that contribute to the gravitational phenomena, such as scalars, vectors, or tensor fields that interact with the metric and result in dynamics different from GR. The presence of such a field provides an additional contribution to the gravitational force [97, 98], leaving (in principle) detectable imprints on the formation and evolution of cosmic structures[99, 100, 101, 102]. Scalar-tensor theories are one of the most well-known examples that follow this approach, such as the well known Jordan-Brans-Dicke model [103]. This theory introduces a scalar field that varies over time in a way that modifies the gravitational constant depending on regions and time. A more generalized form that belongs to this category is the Horndeski theories[104, 105], which encompasses lots of the other theories as a special case, namely Galileon theories [106], $f(R)$ [107] models, Brans-Dicke etc [104]. Chameleon Gravity [108, 109, 110, 111] also falls into this category, which we are going to explore further in the next Section.

GR is a theory where the coupling between matter and the spacetime curvature is minimal. However, there are non-minimally coupled theories [112] where the interaction between matter and gravity is more complex. This may include additional terms in the action that couple scalar and vector fields to the curvature, providing new ways to explain DE and inflation [113].

Exploring higher dimensions is another possibility for Modified Gravity,

which implies adding extra dimensions to the four dimensions; these dimensions are supposed to be observable only at very high energies or very small scales beyond current observations [114, 115]. An example of this category is represented by the Kaluza-Klein theory [116], which suggests that gravity can behave differently at a certain scale with respect to the higher dimensions. These theories also provide intriguing possibilities of unifying gravity with other forces.

Finally, GR is a local theory whose equations at every point of spacetime depend only on its vicinity. However, some MG theories are non-local, allowing for gravitational effects to depend on conditions far away from a given point, providing an alternative dynamic of the universe on large scales. Such theories may offer ways to resolve DE problems without introducing new forms of energy. An example of this type of MG is fractional gravity [117], which modifies the Laplacian in the field equation with a non-local operator, which provides new dynamics and equations of motion.

In summary, gravity can be modified in a variety of ways, including introducing higher-order curvature terms, adding new fields, altering the coupling between gravity and matter, exploring higher dimensional frameworks, and considering non-local interactions. Each of these modifications provide unique insights into the challenges that GR faces in explaining the full range of gravitational phenomena across different scales and regimes. In these, however, we explore two ways of modifying GR, starting with chameleon gravity and a subclass of $f(R)$ theories, which are relevant for our analyses in the second part of this Thesis.

This Chapter is divided as follows. We begin in chapter 3 by categorizing Modified Gravity theories depending on how the modification is made. Then in section 3.2 we discuss in detail the Chameleon Gravity which is the main theory we are concerned with throughout the thesis, followed in section 3.3 by explaining the screening mechanism which a necessary property of the Chameleon. Finally we conclude by discussing the $f(R)$ gravities and a particular subclass that is equivalent to CG.

3.2 Chameleon Gravity

The chameleon field was first introduced by Justin Khoury and Amanda Weltman in their 2004 paper entitled "Chameleon fields: awaiting surprise for tests of Gravity in Space" [108]. In their Paper they proposed a scalar field that dynamically regulate its mass based on local environment becoming heavier in dense regions and lighter in low density regions, making it harder to detect at local densities such as the solar system where no signifi-

cant deviation from GR is detected. This scalar field couples to matter in a non-minimal yet conformal way, which makes the field behavior depend on the local matter density. The Chameleon field offers an alternative explanation through a dynamic scalar field that can evolve over time. It operates similarly to quintessence [118], which as we already mentioned is a scalar field that can drive cosmic acceleration, but with the added advantage that its properties adapt to the local environment. One of the main issues arising when adding a scalar field is the violation of the Equivalence Principle which states that all forms of matter should fall at the same rate in a gravitational field. However, scalar fields are expected to interact with matter, possibly leading to detectable violations of the equivalence principle itself. Nevertheless, the chameleon field surpasses these constraints through the screening mechanism as its mass becomes larger in dense environments, which causes decoupling from matter making it undetectable in local experiments or within our solar system. However, the field gets lighter in cosmological scale which can influence the cosmic dynamics such as expansion and gravity in large scale structures. In addition, Chameleon field features the thin-shell effect, which ensures that only a thin outer mass shells of massive objects interact with it. This suppression is crucial since it allows the field to remain hidden from local tests of gravity, while having the potential to reveal new physics on large, cosmological scales.

We now present the Chameleon field theory and discuss the field equations related to this theory. First we begin with introducing the action of the theory of the chameleon field ϕ coupled to one matter field ψ,

$$S = \int d^4x \left[\sqrt{-g} \left\{ \frac{M_{pl}^2}{2} R - \frac{1}{2} \nabla_\mu \phi \nabla^\mu \phi - V(\phi) \right\} - L_m(\psi, A^2(\phi) g_{\mu\nu}) \right], \tag{3.1}$$

Where $M_{\rm pl} = (8\pi G)^{-1/2}$, and $A(\phi)$ is an arbitrary function of the chameleon field ϕ. The potential $V(\phi)$ is assumed to be of the runaway form, i.e., it is monotonically decreasing [109] and satisfies,

$$\lim_{\phi\to\infty} V = 0, \quad \lim_{\phi\to\infty} \frac{V_{,\phi}}{V} = 0, \quad \lim_{\phi\to\infty} \frac{V_{,\phi\phi}}{V_{,\phi}} = 0 \ldots, \tag{3.2}$$

as well as

$$\lim_{\phi\to 0} V = \infty, \quad \lim_{\phi\to 0} \frac{V_{,\phi}}{V} = \infty, \quad \lim_{\phi\to 0} \frac{V_{,\phi\phi}}{V_{,\phi}} = \infty \ldots, \tag{3.3}$$

where $V_{,\phi} \equiv \frac{dV}{d\phi}$, etc. An example is the inverse power law potential

$$V(\phi) = M^{4+n} \phi^{-n}, \tag{3.4}$$

where M has units of mass and n is a positive constant.
The first thing to notice is that the Chameleon field is affected by the space-time curvature just like an ordinary field in the context of GR. Additionally, the Chameleon couples to matter in a non-minimal way present in $L_m(\psi, A^2(\phi)g_{\mu\nu})$, thus instead of field ψ being affected only by the space-time curvature, it will also be affected by the presence of the Chameleon field through the Jordan frame metric

$$\tilde{g}_{\mu\nu} = A^2(\phi)g_{\mu\nu}. \tag{3.5}$$

We are going to see below that this field also violates the Weak Equivalence Principle since the Chameleon force couples to different fields with different coupling constant. Let us for now derive the field equation of the Chameleon field by differentiating the action with respect to the field ϕ. We get

$$\delta S = \int d^4x\delta\phi \left[\sqrt{-g}\left\{\nabla^2\phi - \frac{dV}{d\phi}\right\} - \frac{\delta}{\delta\phi}L_m(\psi, A^2(\phi)g_{\mu\nu})\right], \tag{3.6}$$

where we can develop the second term by introducing the Jordan frame metric defined in eq. (3.5) as follows

$$\frac{\delta}{\delta\phi}L_m(\psi, A^2(\phi)g_{\mu\nu}) = \left(\frac{\sqrt{-\tilde{g}}}{2}\frac{\delta\tilde{g}_{\mu\nu}}{\delta\phi}\right)\frac{2}{\sqrt{-\tilde{g}}}\frac{\delta}{\delta\tilde{g}_{\mu\nu}}L_m(\psi, \tilde{g}_{\mu\nu}), \tag{3.7}$$

using the fact that

$$\begin{cases} \tilde{T}_{\mu\nu} = -\frac{2}{\sqrt{-\tilde{g}}}\frac{\delta}{\delta\tilde{g}_{\mu\nu}}L_m(\psi, \tilde{g}_{\mu\nu}) \\ \\ \frac{\delta\tilde{g}_{\mu\nu}}{\delta\phi} = 2\frac{d}{d\phi}\log(A)\tilde{g}_{\mu\nu} \\ \\ \sqrt{-\tilde{g}} = A^4(\phi)\sqrt{-g}. \end{cases} \tag{3.8}$$

By replacing this back into eq. (3.7) we get

$$\delta S = \int d^4x\delta\phi \left[\sqrt{-g}\left\{\nabla^2\phi - \frac{dV}{d\phi} + A^4\frac{d}{d\phi}\log(A)\tilde{T}\right\}\right], \tag{3.9}$$

where $\tilde{T}$ is the trace of the stress energy tensor in the Jordan frame, which finally gives

$$\nabla^2\phi = \frac{dV}{d\phi} - A^4\frac{d\log(A)}{d\phi}\tilde{T}. \tag{3.10}$$

Note that since matter fields, represented by ψ, couple universally to the metric $\tilde{g}_{\mu\nu}$, meaning that experiments involving measurements of the field ψ

are measured in the Jordan frame such as, for instance, the matter density $\tilde{\rho}$.
However, we need to express our result with respect to the stress energy tensor T in the Einstein frame (the frame corresponding to $g_{\mu\nu}$). Without lose of generality, it is assumed in the literature [109, 108, 119] that the function $A(\phi)$ takes the form

$$A = e^{\beta\phi/M_{\rm pl}}, \tag{3.11}$$

if we further assume an FLRW background metric with an equation of state defined as $\tilde{\rho} = \omega\tilde{p}$ and a continuity equation $\tilde{\nabla}^{\mu}\hat{T}_{\mu\nu} = 0$. The energy density in the Einstein frame ρ is defined as the quantity that is conformally related to $\tilde{\rho}$ and scales as $a^{-3(1+\omega)}$. It can be shown that [119]

$$\tilde{T} = \frac{1}{A^{3+\omega}}T. \tag{3.12}$$

Finally we can write the equation of motion in its final form as

$$\nabla^2\phi = V_{,\phi} + (1-3\omega)\frac{\beta}{M_{\rm pl}}\rho e^{(1-\omega)\beta\phi/M_{\rm pl}}. \tag{3.13}$$

Before we conclude it is worth mentioning that in the previous calculations we considered a single matter field ψ; we could have also considered a set of matter fields $\psi^{(i)}$ which do not interact with each other. Their metric in the Jordan frame will be

$$\tilde{g}^{(i)}_{\mu\nu} = e^{2\beta_i\phi/M_{\rm pl}}g_{\mu\nu}. \tag{3.14}$$

The equation of motion eq. (3.13) becomes [109, 119]

$$\nabla^2\phi = V_{,\phi} + \sum_i (1-3\omega_i)\frac{\beta_i}{M_{\rm pl}}\rho_i e^{(1-\omega_i)\beta_i\phi/M_{\rm pl}}. \tag{3.15}$$

We can now proceed with the description of the screening mechanism in the next Section.

3.3 Screening mechanism

As we mentioned earlier, the Chameleon field comes with a screening mechanism that allows the field to escape GR solar system tests and gives more freedom to MG at larger scales. In order to illustrate that, we can firstly

study a concrete example of non-relativistic matter ($\omega = 0$). Thus, eq. (3.13) becomes

$$\begin{cases} \nabla^2\phi = V_{\text{eff},\phi} \\ \\ V_{\text{eff}} = V(\phi) + \rho e^{\beta\phi/M_{\text{pl}}}. \end{cases} \tag{3.16}$$

From eq. (3.4) we can see that the Chameleon potential has no minimum. On the other hand, what matters for us is the effective potential defined in eq. (3.16). The minimum of the potential is defined as $V_{\text{eff},\phi}(\phi_{min}) = 0$. Which gives

$$V_{,\phi}(\phi_{\text{min}}) + \frac{\beta}{M_{\text{pl}}}\rho e^{\beta\phi/M_{\text{pl}}} = 0. \tag{3.17}$$

We can also define the mass of the Chameleon field as

$$m^2_{\text{min}} = V_{,\phi\phi}(\phi_{\text{min}}) + \frac{\beta^2}{M^2_{\text{pl}}}\rho e^{\beta\phi/M_{\text{pl}}}. \tag{3.18}$$

Since $V_{,\phi}(\phi)$ is negative and increasing, assuming $\beta > 0$ would imply that, the larger the density ρ is, the lower ϕ_{min} is and vice-versa. Moreover, we know that $V_{,\phi\phi}(\phi)$ is positive and increasing which would imply the larger the density ρ the larger the mass m_{min} and vice versa. The later shows that at higher densities the field Chameleon field is suppressed and therefore GR holds[109]. The behavior of the effective potential around its minimum is illustrated in fig. 3.1.

It is worth noting that the assumptions in eq. (3.4) which we imposed on the Chameleon potential are crucial to ensure the presence of the screening mechanism.

Before concluding, we study an approximate solution of the Chameleon field for compact objects as it will be crucial for our analysis in the second part of the thesis. Let us assume a compact object with spherical symmetry, thus eq. (3.16) becomes

$$\frac{d^2\phi}{dr^2} + \frac{2}{r}\frac{d\phi}{dr} = V_{,\phi} + \frac{\beta}{M_{pl}}\rho(r)e^{\beta\phi/M_{\text{pl}}}. \tag{3.19}$$

We also approximate the density within the compact object to ρ_c and the density of the matter that surround the object ρ_∞, that is

$$\rho(r) = \begin{cases} \rho_c & r < r_c \\ \\ \rho_\infty & r > r_c. \end{cases} \tag{3.20}$$

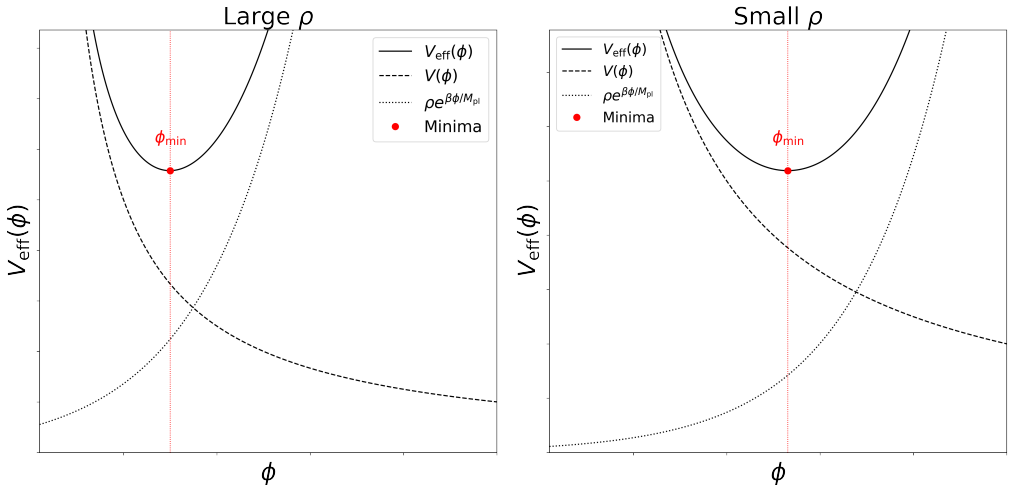

Figure 3.1: Effect of the density ρ on the shape of the effective potential and its minimum: the Larger the density, the lower the minimum and the larger the second derivative (equivalently m_{min}).

We also note the values of the field that minimize the effective potential given in eq. (3.16) by ϕ_c and ϕ_∞ for inside and outside the compact object respectively. Additionally, we need two boundary conditions for solving the second order differential equation. The first one is imposing non-singularity of the first derivative at $r = 0$. Moreover, we assume the effective potential to reach its outside minimum at $r \to \infty$ when the density is ρ_∞.

$$\begin{aligned} \frac{d\phi}{dr} &= 0 \qquad \text{as } r = 0, \\ \phi &\to \phi_\infty \qquad \text{as } r \to \infty. \end{aligned} \tag{3.21}$$

In order to obtain the solution for the region where $r > r_c$, we can approximate the differential equation to

$$\frac{d^2\phi}{dr^2} + \frac{2}{r}\frac{d\phi}{dr} \simeq m_\infty^2(\phi - \phi_\infty), \tag{3.22}$$

which has the solution

$$\phi(r) \simeq -\frac{r_c(\phi_\infty - \phi_c)}{r} e^{-m_\infty(r - r_c)} + \phi_\infty. \tag{3.23}$$

The above solution can be rewritten in a more convenient way[109] which

takes the form

$$\phi(r) \simeq \begin{cases} \phi_c & r < r_c \\ -\left(\frac{\beta}{4\pi M_{\rm pl}}\right)\left(\frac{3\Delta r_c}{r_c}\right)\frac{M_c e^{-m_\infty r}}{r} + \phi_\infty & r > r_c, \end{cases} \tag{3.24}$$

where M_c is the mass of the compact object at $r = r_c$, and Δr_c is the thin shell that forms as the field rolls down the effective potential at $r < r_c$, which can be shown [109] to be

$$\frac{\Delta r_c}{r_c} = \frac{\phi_\infty - \phi_c}{6\beta M_{\rm pl}\Phi_c} \ll 1, \tag{3.25}$$

where Φ_c is the Newtonian potential at $r = r_c$.
We can see from eq. (3.24) that the solution exists only if the condition eq. (3.25) is satisfied, which shows that the solution of the Chameleon field manifests only through an outside thin shell of the compact object. One may argue that this is only a feature of the regime where the object is assumed to be large enough to produce this effect. The above solution still holds for what is called the thick regime where the dimensions of the shell are comparable to the ones of the object, i.e., $\frac{\Delta r_c}{r_c} > 1$. In this case, the whole compact object contributes to the solution and in this case the outside solution is given as

$$\phi(r) \simeq -\left(\frac{\beta}{4\pi M_{\rm pl}}\right)\frac{M_c e^{-m_\infty r}}{r} + \phi_\infty. \tag{3.26}$$

One last thing to point out is that the Chameleon field induces a fifth force (as it can be seen from eq. (3.24)) that adds to the gravitational force in the Newtonian limit, which is given as

$$F_\phi = -\frac{\beta}{M_{\rm pl}}\nabla\phi. \tag{3.27}$$

In the second part of the Thesis we shall use the same logic to derive the solutions of the Chameleon field in galaxy clusters, as cosmologically the largest bounded structures, where we expect the thin shell solution to hold.

3.4 $f(R)$ models

In this Section we explore the $f(R)$ approach to MG. This modification considers a more general function of the Ricci Scalar R denoted as $f(R)$ in the action. This simple modification introduces higher order curvature terms

which affect the gravitational dynamics. One of the motivations for considering $f(R)$ gravity arises from the fact that GR requires the inculsion of the phenomenological cosmological constant, to explain the accelerated expansion of universe as mentioned in section 2.5, and it offers an alternative approach to gravitational interactions which could potentially explain the late time acceleration of the universe without introducing the DE component by hand. In these theories the curvature of spacetime behaves differently at large scales leading to an effective repulsive force that can drive the accelerated expansion. Additionally, some $f(R)$ models can mimic the effects of dark matter by parameterizing the theory in a way to account for gravitation, especially in rotation curves and cluster dynamics without assuming the existence of an additional form of matter [120]. Furthermore, theories of inflation typically require the introduction of a scalar field (the "inflaton") to drive this expansion. However, $f(R)$ gravity can achieve inflationary behavior through the curvature terms themselves, without needing an additional field, as in the well known Starobinsky model of inflation [121], where $f(R) = R+aR^2$ leads to a successful inflationary scenario [78, 70] . From the perspective of high energy physics, general relativity is not renormalizable [122] , which makes it incompatible with quantum field theory. This causes a serious problem for attempts to develop a quantum theory of gravity. In contrast, $f(R)$ naturally introduces higher-order curvature terms in the action, which makes the theory more tractable at high energies in extreme regimes such as near black hole singularities or in the very early universe. In fact it's been shown by Stelle in 1977 that the $f(R)$ theories are renormalizable though not unitary [123], which makes them an important step towards formulating a quantum theory of gravity.
Let's first define the action of the theory, and then derive the field equations

$$S = \int \sqrt{-g} d^4x \left[\frac{M_{pl}^2}{2} f(R) + L_m \right]. \tag{3.28}$$

Following the same approach used in section 1.3 we can get

$$f_R R_{\mu\nu} - \frac{1}{2} f g_{\mu\nu} + [g_{\mu\nu}\nabla^2 - \nabla_\mu \nabla_\nu] f_R(R) = \frac{1}{M_{\rm pl}} T_{\mu\nu}, \tag{3.29}$$

where we denoted $f_R \equiv \frac{df(R)}{dR}$.

In order to be able to see the dynamics of the extra curvature terms as a GR like formalism, eq. (3.29) can be rewritten as

$$\begin{aligned} R_{\mu\nu} - \frac{1}{2} R g_{\mu\nu} &= \frac{1}{M_{\rm pl} f_R(R)} \left[T_{\mu\nu} + T_{\mu\nu}^{eff} \right], \\ T_{\mu\nu}^{\rm eff} &= M_{\rm pl} \left[\frac{1}{2} g_{\mu\nu}(f - R f_R) - (g_{\mu\nu}\nabla^2 - \nabla_\mu \nabla_\nu) f_R \right]. \end{aligned} \tag{3.30}$$

From eq. (3.30) We can interpret the $f(R)$ gravity as another matter field with stress energy tensor $T_{\mu\nu}$ which does not vanish in vacuum. Thus, DE can be interpreted as a geometrical consequence that emerges from the other curvature term beside the Ricci scalar R. We can see that $f(R)$ scenarios introduce a new scalar filed term in the field equation, through taking the trace of eq. (3.29), which gives

$$f_R R - 2f + 3\nabla^2 f_R = \frac{1}{M_{\rm pl}} T, \tag{3.31}$$

which may be expressed as

$$\begin{cases} \nabla^2 f_R = V_{eff,f_R} \\ \\ V_{\rm eff} = \frac{1}{3}\left[2f_R f - \frac{1}{2}f_R^2 R + \frac{1}{M_{\rm pl}} T f_R\right]. \end{cases} \tag{3.32}$$

This shows that f_R can be looked at as a scalar field in this theory. It is worth noting that we have derived the previous equations without any loss of generality. However, $f(R)$ models that are relevant for this Thesis, i.e., those which have screening mechanism, are represented by a specific function $f(R)$ that meet several observational criteria. First, cosmology must replicate the behavior of ΛCDM at high redshifts where it has been tested by CMB data. Second, it should drive the cosmic acceleration at low redshifts with an expansion history similar to ΛCDM without the introduction of a cosmological constant. In addition, we should have enough parameters in the model to mimic a wide range of low-redshift phenomena that are consistent with observations. Lastly, it should include the ΛCDM as a limiting case to escape solar system tests[124]. The above can be satisfied if we impose the conditions

$$\begin{aligned} \lim_{R\to\infty} f(R) &= R + const., \\ \lim_{R\to 0} f(R) &= R. \end{aligned} \tag{3.33}$$

In other words, at early universe, we recover GR with a cosmological constant to match the data and to avoid any unwanted divergent at dense regions, while at late time regimes MG become significant only at low curvatures and do not dominate in other regimes. These models can also exhibit a chameleon like screening mechanism which becomes clear if we compare eq. (3.32) to eq. (3.4). We can see that, just like in the case of the Chameleon field, these models couple to matter and therefore the solution of the scalar field f_R is different for low and high density regions.
The question on how can we relate the field ϕ in the case of the Chameleon

Gravity to f_R in the $f(R)$ models can be answered simply by making the modification as shown in [125]:

$$f_R = e^{-\frac{2\beta}{M_{\rm pl}}\phi}. \tag{3.34}$$

By replacing this into eq. (3.32) and by looking at the coupling term between the trace of the stress energy tensor and the exponent, we can see that the equivalence is true when

$$\beta = \sqrt{1/6}, \tag{3.35}$$

and the value of the f_R in low density regions which we write as f_R0 is therefore

$$f_{R0} = e^{-\frac{2\beta}{M_{\rm pl}}\phi_\infty}. \tag{3.36}$$

We conclude this Chapter by making an important note, i.e. that the Chameleon screening presented here has two main parameters (if the matter density is fixed), which are the coupling constant β and the value of the field at large distances ϕ_∞, i.e., the parameter space of the chameleon field lies on a two dimensional plane. However, the $f(R)$ model we presented has only one parameter f_R0. Thus, it is more practical to study the Chameleon screening and then take the $f(R)$ model as a particular case that belongs to a one dimensional line in the Chameleon parameter space. These parameters are going to be our main focus in the second part of this Thesis while studying the phenomenology of CG in galaxy clusters.

Part II

Modified Gravity in Clusters of Galaxies

Chapter 4

Constraining MG using galaxy cluster dynamics

In the first part of the Thesis we've been dealing with GR and its application in the general framweork of cosmology, explaining why the evidence for DE and other occurrences represent motivations for considering MG scenarios. We have quoted some of the theories with different motivations for modifying GR, focusing on $f(R)$ and CG. In this Chapter we are going to constrain the Chameleon screening mechanism in galaxy clusters, essentially obtaining limits on the coupling strength and CG field behavior.

4.1 New data for constraining CG with Galaxy Clusters

As we have seen, two main parameters construct the chameleon field model in a galaxy cluster: the first one is β, which is the coupling constant between the chameleon field and matter density, and the latter, ϕ_∞, which is the intensity of the field at a larger distance away from the cluster. Under reasonable assumptions (e.g. [126]) these two parameters describe the modification of gravity completely. Also, the case of $\beta = \sqrt{1/6}$ within the Chameleon field scenario describes an $f(R)$ theory [127, 128].

We consider that the total mass distribution of a galaxy cluster can be parametrized by a NFW density model [129, 130, 131, 132, 133, 134]; under the assumption of hydrostatic equilibrium, the total gravitational potential of the cluster will affect the pressure of the hot gas [126]. We implement the formalism presented in [126, 135] to the XMM-Newton Cluster Outskirts Project X-COP data products [136, 137, 138, 139], which consists of 12 clusters with well-observed X-ray emission and high signal to noise ratio in the Planck

Sunyaev-Zel'dovich (SZ) survey [57], essentially providing both ICM temperature and pressure data over the large radial range of $0.2\,\mathrm{Mpc} \leq \mathrm{r} \leq 2\,\mathrm{Mpc}$. While in the current analysis, we probe individual galaxy clusters through hydrostatic equilibrium, a robust and complementary approach relies on the analysis of cosmological simulations [140, 141, 142, 143] to assess average or distribution statistics as a function of cosmic time. For instance, the authors in [140] study scaling relations in Chameleon type $f(R)$ models from simulations of galaxy clusters, and [144] study variations to the halo mass function.

This Chapter is organized as follows: in Section 4.2 we construct our model for the Chameleon field and show the solution of this field as applied to galaxy cluster with the assumption of the NFW profile, and at the end of the section we discuss the effect of the modification induced by the presence of Chameleon field on the Hydrostatic pressure. In Section 4.3 we briefly present the X-COP data and then construct the likelihood that we will use with the MCMC analysis to generate the chains that constrain our parameter space. In Section 4.4 we present our results and discuss them in detail while comparing our constraints with the ones obtained by other galaxy clusters' analyses (e.g. [126, 145]). Finally, we further derive our main conclusions in Section 4.5.

4.2 Modeling

In this section, we set the basis of our simulations, by specializing the screening mechanism described in the previous Chapter to the case we are about to investigate, and describing the CG field in galaxy clusters.

4.2.1 Screening Mechanism for $\phi_\infty \ll M_{\rm Pl}$

As we have seen previously, the Lagrangian of the theory includes the usual Einstein- Hilbert Lagrangian plus the scalar field, in addition to the Standard Model fields coupled minimally to gravity [108, 146, 147, 148, 149], which is written as

$$L = \frac{M_{\rm Pl}^2}{2} R + L_m(\tilde{g}_{\mu\nu}, \psi) + L_\phi \,, \tag{4.1}$$

where $L_\phi = -\frac{1}{2}(\partial\phi)^2 - V(\phi)$ and $M_{\rm Pl} = \frac{1}{\sqrt{8\pi G}}$; the Standard Model fields are represented by ψ, and $\tilde{g}_{\mu\nu} = A^2(\phi) g_{\mu\nu}$. As presented in section 3.3, the equation of motion for the field ϕ can be written [150] as

$$\nabla^2\phi = V'(\phi) - \frac{A'(\phi)}{A(\phi)} T \,, \tag{4.2}$$

where we have highlighted T as the trace of the stress-energy tensor of the standard model field ψ as well as the main source of the Chamaleon field dynamics, and we further assume that the field ϕ is static, targeting staticity in a formed object, such as a galaxy cluster. The field values depend on the matter component and thus the field behaves in different ways for different matter distributions. The framework of CG in cosmology suggests that the maximum value of the chameleon field at large distance (ϕ_∞) is very small compared to the plank mass M_{Pl}, that is $\frac{\phi_\infty}{M_{pl}} \ll 1$. Therefore we use the approximation $\frac{A'(\phi)}{A(\phi)} \simeq \frac{\beta}{M_{\rm Pl}}$(see eq. (3.11)) , here β is the coupling factor between the field ϕ and the stress-energy tensor T. Finally, we consider only pressureless non-relativistic matter fields, which implies $T = -\rho_m$. Therefore we can write,

$$\nabla^2\phi = V'_{\rm eff}(\phi)\,, \tag{4.3}$$

where

$$V_{\rm eff}(\phi) = V(\phi) + \frac{\beta\phi}{M_{\rm Pl}}\rho_m\,. \tag{4.4}$$

As pointed out in section 3.3, the form of the potential $V(\phi)$ should guarantee that the gravitational effect induced by this field will be suppressed when we have large matter densities, that is, the field ϕ is screened and GR is recovered. On the other hand, at lower densities, we want the effect of the field to become important, which will require us to impose that the potential $V(\phi)$ is a decreasing function of ϕ [108].

In the region where ϕ is un-screened, an additional fifth force is induced by the gradient of the Chameleon field,(see eq. (3.27))providing an additional contribution to the Newtonian potential while retaining hydrostatic equilibrium assumption in chameleon gravity.

4.2.2 Chameleon field in clusters of galaxies

In the following analysis, we assume that the total matter density distribution within the galaxy cluster can be modeled [129] following a NFW profile corresponding to

$$\rho(r) = \frac{\rho_s}{r/r_s(1+r/r_s)^2}\,, \tag{4.5}$$

where $\rho_{\rm s}$ and $r_{\rm s}$ are characteristic density and scale radius, respectively. The NFW model has been shown to provide a good description for simulated DM halos (see e.g. [151]) and for real clusters' data in ΛCDM (e.g. [152, 153]), while some other works have further suggested that the NFW profile performs well also in modified gravity scenarios, including chameleon gravity [154, 155, 156, 157].

We are interested in finding the solution for the chameleon Equation (4.3) in the presence of a matter density distribution given by Equation (4.5); in order to do that, we employ the semi-analytical approach followed by e.g. [126]. The idea is that below some radius r_c, the value of the scalar field in the interior minimizes the effective potential $V_{eff}(\phi)$ which represents the regime where the Chameleon force does not contribute and the solution is obtained by setting $\nabla\phi = 0$ on the left side of Equation (4.3). On the other hand, at larger distances, the potential $V(\phi)$ is negligible and the second term in (4.4) dominates the effective potential. The solution in this regime is obtained by solving $\nabla^2\phi = \beta\phi\rho_m/M_{\rm Pl}$. Therefore, we obtain the complete semi-analytical solution as,

$$\phi(r) = \begin{cases} \phi_s\,[r/r_s(1+r/r_s)^2] = \phi_{\rm int} \simeq 0 & r < r_c \\ -\frac{\beta\rho_s r_s^2}{M_{\rm Pl}}\frac{\ln(1+r/r_s)}{r/r_s} - \frac{C}{r/r_s} + \phi_\infty = \phi_{\rm out} & r > r_c\,. \end{cases} \tag{4.6}$$

In the equation above, ϕ_s is a constant that depends on the characteristic density and the parameters of the potential $V(\phi)$. The integration constant C and the radius r_c can be specified by imposing the continuity of the solution and its first derivative at $r = r_c$. Thus we have [126],

$$1 + \frac{r_c}{r_s} \simeq \frac{\beta\rho_s r_s^2}{M_{\rm Pl}\phi_\infty}\,, \tag{4.7}$$

$$C \simeq -\frac{\beta\rho_s r_s^2}{M_{\rm Pl}}\ln(1+r/r_s) + \phi_\infty r/r_c\,. \tag{4.8}$$

The *screening* radius r_c represents the transition below which the Chameleon field is screened, and as shown in Equation (4.7), it is completely determined by the other parameters of the model. In particular, the screening radius is strongly dependent on the mass of the cluster $M_{500} \propto r_s^3\rho_s$ (see Equations (4.19) and (4.20)). This implies that in massive clusters the screening mechanism tends to be very efficient, while the fifth force is more active in lower mass halos (e.g. [158]).

Note that the current formalism assumes coupling of the Chameleon field to both the dark matter and baryonic mass components and that the total mass of the cluster is modeled using a single NFW mass profile. This formalism is equivalent to that followed in the earlier works [145, 126] and is an approximation that the contribution of the baryonic component to the total mass is negligible in the radial ranges explored and that a simple NFW profile is sufficient to model the total mass accurately. Although there is a clear possibility to introduce varied coupling for the different mass components and the field, this is beyond the scope of the thesis. However, it is straightforward to model the gas mass, which accounts for the largest contribution to

the baryonic mass, that does not couple with the chameleon field, while the dark component does (see for example [159]) and perform the analysis, which we discuss in Section 4.4.6. So far we have described the chameleon formalism within the galaxy cluster sourced only by the self-screening. However, it is important to point out that, the inter-cluster environmental density distribution can generate an additional contribution to the fifth force [160, 144]. This in turn is the interplay between the external and the internal densities distinguished by a scale. For example, [160] employ a scale of $r_{\rm in/out} = 8\,{\rm h}^{-1}{\rm Mpc}$ (see also [161]) and average over the environmental effects. Taking into account the strong local constraints, for example, (e.g. $|f_{R0}| \sim 5 \times 10^{-7}$ [162]), the mass ranges ($\geq 10^{14} M_{\odot}$) of the local ($z \leq 0.1$) galaxy clusters utilized in this work, we infer the environmental effects to be relatively small, providing only a mild weakening of our constraints.

4.2.3 $f(R)$ analogy with Chameleon field

As we have seen in the first part of this Thesis, $f(R)$ [163] is one of the most investigated alternatives to GR at the cosmological level; in this class of models, the Einstein-Hilbert action is modified by adding a generic function of the Ricci scalar:

$$S = \int {\rm d}^4x\sqrt{-g}\frac{1}{16\pi G}\left[R + f(R)\right] + S_m[\psi_i, g_{\mu\nu}]\,. \tag{4.9}$$

As previously discussed in section 3.4, the functional form of $f(R)$ can be chosen in such a way that the background ΛCDM expansion history is reproduced as close as desired (see e.g. [124]). The derivative of the function $f_R = \partial f_R/\partial R$ plays a role of a dynamical scalar field which, under certain conditions can be conformally recast into a scalar-tensor model exhibiting chameleon screening (see e.g. [164]). This is possible in particular if the scalar field $f_R = \partial f_R/\partial R$, called the *scalaron*, has a large positive effective mass at high curvature[165].

The field equation for f_R is [124]

$$\Box f_R = \frac{\partial V_{\rm eff}(f_R)}{\partial f_R}\,, \tag{4.10}$$

which is analogous to Equation 4.3 with the replacement:

$$f_R = \exp\left(-\frac{2\beta\phi}{M_{\rm Pl}}\right)\,, \tag{4.11}$$

and $\beta = \sqrt{1/6}$ [126, 166]. The value of the scalar field for the background today $f_{R0} = \bar{f}_R(z=0)$ is proportional to the present value of the chameleon field at infinity as $f_{R0} = -\sqrt{\frac{2}{3}}\frac{\phi_\infty}{M_{\rm Pl}}$.

In the last decades, several works have placed constraints on $f(R)$ gravity using different probes, both at astrophysical (e.g. [162, 167, 157, 168]) and at cosmological (e.g [126, 144, 145, 169, 170, 171, 172, 173]) scales. Currently, the most stringent bounds on the scalaron are of the order of $f_{R0} \lesssim 10^{-8}$, for the Hu& Sawicki functional form of $f(R)$ ([124]), from galaxy morphology [174], while cosmological analyses limit the background field to be $f_{R0} \lesssim 10^{-6}$ (e.g. [175]).

4.2.4 Hydrostatic Equilibrium

For a spherical system that contains gas with pressure P and density ρ_g, the hydrostatic equilibrium equation is given by,

$$\frac{1}{\rho_g}\frac{\mathrm{d}P(r)}{\mathrm{d}r} = -\frac{GM(<r)}{r^2}\,, \tag{4.12}$$

where $M(r)$ is the mass enclosed within the radius r, and the above equation represents the balance between the force induced by the gas pressure and the gravitational force. However, in the current MG scenario, we have an additional force given by Equation (3.27) induced by the existence of the Chameleon field, which contributes as a new term in the hydrostatic equilibrium equation as [126],

$$\frac{1}{\rho_g}\frac{\mathrm{d}P(r)}{\mathrm{d}r} = -\frac{GM(r)}{r^2} - \frac{\beta}{M_{\rm Pl}}\frac{\mathrm{d}\phi(r)}{\mathrm{d}r}\,, \tag{4.13}$$

which upon integration provides

$$P(r) = P_0 - \mu m_p \int_0^r n_e(r)\left[\frac{GM(r)}{r^2} + \frac{\beta}{M_{\rm Pl}}\frac{\mathrm{d}\phi(r)}{\mathrm{d}r}\right]\mathrm{d}r\,, \tag{4.14}$$

Where μ is the mean molecular weight, P_0 is an integration constant, i.e., pressure at $r = 0$, and $n_e(r)$ is the electron density at radius r. We further assume the electron density to follow the Vikhlinin profile [176, 177],

$$n_e(r) = n_0 \frac{\left(\frac{r}{r_1}\right)^{-\alpha_v/2}\left[1+(\frac{r}{r_2})^{\gamma_v}\right]^{-\epsilon_v/2\gamma_v}}{\left[1+(\frac{r}{r_1})^2\right]^{3\beta_v/2-\alpha_v/4}}\,, \tag{4.15}$$

where we fix $\gamma_v = 3$ as suggested in [176]. The electron density profile above thus contains 6 parameters. While the original Vikhlinin profile contains 9 parameters, it was earlier validated that the 6-parameter reduced form is sufficient for the dataset utilized here [178].

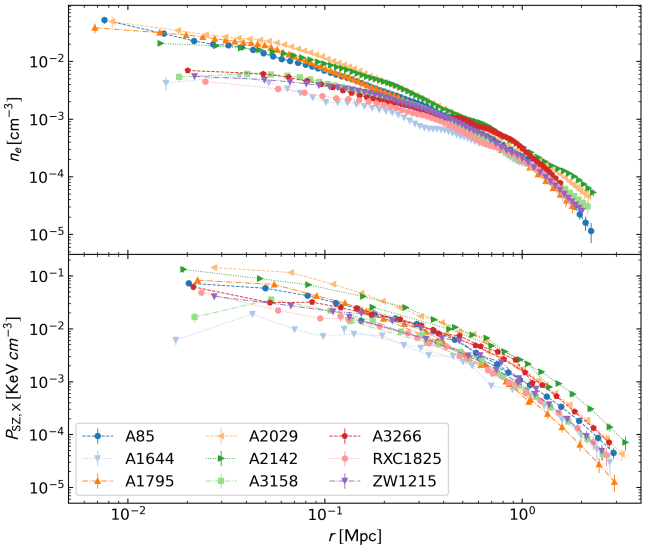

Figure 4.1: *Top*: Radial profiles of the electron density [139]. *Bottom*: Pressure data obtained using the Compton effect ($P_{\rm SZ}$) and the X-ray observations ($P_{\rm X}$) [137]. We show the data for all the nine clusters we have utilized in the current analysis.

4.3 Data and Likelihood

4.3.1 X-COP clusters

We utilize 9 X-COP clusters [137], following the formalism utilized in an earlier work [178, 179].While a total of 12 clusters are available in the X-COP compilation, in the current work we use only 9 of them excluding A644, A2255, and A2319. The 3 excluded clusters do not favor the NFW mass profile which is an integral assumption in obtaining the semi-analytical expressions for the field in the formalism adopted here. We however include A1644 which is reported to perform equivalently for NFW and the best-fit Hernquist mass profile. We defer the study of the effects of mass profile assumptions on the constraints on the screening mechanisms to the next Chapter We show the final datasets of the electron density (*top*), and pressure obtained using both X-ray and SZ methods [180] (*bottom*) in Figure 4.1.

4.3.2 Likelihood

The complete formalism introduced in Section 4.2 is described by 10 parameters; 2 defining the Chameleon field (β and ϕ_∞), 2 for the NFW profile (ρ_s and r_s), the remaining 6 parameters are from the expression of the electron density given by Equation (4.15). The individual likelihood ($-2\ln\mathcal{L}$) for the pressure and electron density data are then written as,

$$\chi^2_P = \left(\mathbf{P}^{\rm obs}_{\rm SZ} - \mathbf{P}_{\rm SZ}\right)\mathbf{\Sigma}_P^{-1}\left(\mathbf{P}^{\rm obs}_{\rm SZ} - \mathbf{P}_{\rm SZ}\right)^T + \ln|\mathbf{\Sigma}_P| + \sum_i \left[\frac{\left(P_X(r_i) - P^{\rm obs}_{X,i}\right)^2}{\sigma^2_{P_{X,i}} + \sigma^2_{\rm int}} + \ln\left(\sigma^2_{P_{X,i}} + \sigma^2_{\rm int}\right)\right]. \tag{4.16}$$

$$\chi^2_{n_e} = \sum_i \frac{(n_e(r_i) - n^{obs}_{e,i})^2}{\sigma^2_{n_{e,i}}}, \tag{4.17}$$

respectively. The total χ^2 function is then the summation of individual contributions, upon which we perform the Bayesian analysis and is given by,

$$-2\ln\mathcal{L}^{\rm tot} \equiv \chi^2(\Theta_{n_e}, \Theta_{\rm NFW}, \Theta_{\rm MG}) = \chi^2_{\rm P} + \chi^2_{n_e} \tag{4.18}$$

wherein $\Theta_{n_e} = \{n_0, r_1, r_2, \alpha_v, \beta_v, \epsilon_v\}$, $\Theta_{\rm NFW} = \{M_{500}, c_{500}\}$ and $\Theta_{\rm MG} = \{\phi_{\infty,2}, \beta_2\}$. Refer to [178, 179], for further details on the likelihood and the inclusion of the intrinsic scatter ($\sigma_{\rm int}$) parameter.

Therefore, we perform an MCMC analysis over a 10-dimensional parameter space $(n_0, r_1, r_2, \alpha, \beta, M_{500}, c_{500}, \phi_{\infty,2}, \beta_2)$, where the two parameters β_2 and $\phi_{\infty,2}$ are compactified functions of β and ϕ_∞, respectively, and are given by $\beta_2 = \beta/(1+\beta)$ and $\phi_{\infty,2} = 1 - \exp(-\phi_\infty/10^{-4}M_{\rm Pl})$. These new scaled parameters run in the interval $[0,1]$, making the interpretation of the results straightforward. It is also convenient to use M_{500} and R_{500} instead of ρ_s and r_s which are related through the following relations [126]:

$$r_s = \frac{1}{c_{500}}\left[\frac{M_{500}}{(4\pi/3)\Delta_c\rho_c}\right]^{1/3} \tag{4.19}$$

$$\rho_s = \frac{M_{500}}{4\pi r_s^3}\left(\ln(1+c_{500}) - \frac{c_{500}}{c_{500}+1}\right)^{-1} \tag{4.20}$$

where $c_{500} = R_{500}/r_s$ is the concentration parameter, and we have also $M(r < R_{500}) = M_{500} = \frac{4\pi}{3}R^3_{500}\Delta_c\rho_c$, where $\Delta_c = 500$ and ρ_c is the critical density at the cluster redshift.

We emphasize that in our analysis we implement two different priors on the mass parameter M_{500}; however we also perform the analysis without any

restriction on the mass, unlike previous work on other clusters (e.g. Coma cluster in [126]), and therefore we anticipate testing possible degenerate scenarios in the posterior parameter space (allowed at some range of the virial mass), this is discussed at length in the Section 4.4.5.

4.3.3 Weak Lensing mass priors

CG belongs to a subset of scalar-tensor theories for which the gravitational potential inferred by lensing techniques corresponds to the Newtonian potential (i.e. the contribution of the fifth force does not affect null geodesics). As such, we can implement the information provided by lensing estimation as prior on the "true" cluster mass M_{500}, as done in e.g. [126, 145]. We utilize the estimates of M_{500} obtained using weak lensing analyses in [181], wherein no information on the shape (c_{500}) of the mass profile is available. However, we find that mass information is available only for five clusters in the sample, A85, A1795, A2029, A2142, and ZW1215. In Table 4.1, we show the mean and 1σ uncertainties on M_{500} for these clusters, taken from [181]. We beforehand anticipate that the constraints on mass parameters we shall obtain using the X-COP data will be much tighter than the uncertainty of the weak lensing masses we use as priors.

Table 4.1: We show the weak lensing masses utilized as mass priors for the 5 clusters available from [181]. We utilize the mass estimated using the NFW mass profile for consistency, please see the Table A2 in [181]. See also Section 4.4.5 for more comments.

Cluster	$M_{500}[10^{14}\,M_{\odot}]$
A85	5.7 ± 2.2
A1795	9.3 ± 2.2
A2029	12.1 ± 2.5
A2142	9.7 ± 2.3
ZW1215	3.5 ± 2.2

We perform a full Bayesian analysis utilizing Equations (4.16) and (4.17) to define the likelihood, through the publicly available `emcee`[1] package [182, 183], which implements an affine-invariant ensemble sampler. To analyze the MCMC chains we utilize either the `corner` and/or `GetDist` [2] [184] packages.

[1] http://dfm.io/emcee/current/
[2] https://getdist.readthedocs.io/

Also, we impose uniform flat priors on all the parameters, specifically for the modified gravity parameters $\{\beta_2, \phi_{\infty,2}\} \in [0.001, 1.0]$. As the current analysis provides posteriors of exclusion within the parameter space, always including the GR scenario, to the first order we refrain from performing any model selection, which is bound to select GR with higher preference.

Finally, we implement a simple importance sampling-like routine to combine the constraints in the $\Theta_{\rm MG}$ parameter space, obtained using the individual clusters. Given that the parameters $\Theta_{\rm NFW}$ and Θ_{n_e} are cluster-specific and are not expected to affect the joint constraints on the $\Theta_{\rm MG}$ parameters which are of a global theory. Therefore, we combine the MCMC samples of the $\Theta_{\rm MG}$ parameters obtained from each of the clusters where the sample density represents the values of the posterior (Bayesian confidence levels). We take a sub-sample of thinned MCMC samples of equal size and re-sample the joint posteriors. Essentially, this approach is equivalent to marginalizing all the cluster-specific parameters, while not being able to see the effect of the joint analysis on them. The results of the combined analysis are given in Section 4.4.3.

4.4 Results

We begin by presenting the constraints on the $\{\phi_{\infty,2},\ \beta_2\}$ parameter space for each of the nine clusters as shown in Figure 4.2, utilizing the *internal mass prior*, elaborated in the next paragraph. The blue and light blue regions depict the allowed parameter space at 2σ and 3σ, respectively, while the white region consequently is excluded by the current data at 3σ confidence level. We can already notice for all clusters that at low β_2 (equally β), $\phi_{\infty,2}$ is unconstrained: as the coupling constant becomes negligible, the Chameleon field is decoupled from matter and can no longer be constrained. Meanwhile, at large values of β, that is when $\beta_2 \simeq 1$, the coupling is too strong that the entirety of the clusters will be screened, i.e, the screening radius is larger than the size of the cluster in which case also all values of $\phi_{\infty,2}$ are allowed. We also find that at low values of β_2, a slightly larger part of the parameter space is excluded compared to the results presented in [126] and [145], which in our results extends to $\beta_2 \sim 0.2$. In Figure 4.2, this lower limit is what we see as an almost vertical line in the contours that separates the blue allowed region from the white excluded one for lower values of β_2. On the other hand, compared to the same previous results, we find that the lowest possible values for $\phi_{\infty,2}$ are also lower, which further reduces the allowed region providing tighter constraints in our analysis. This is mainly due to the effect of the internal mass prior, as we will discuss below.

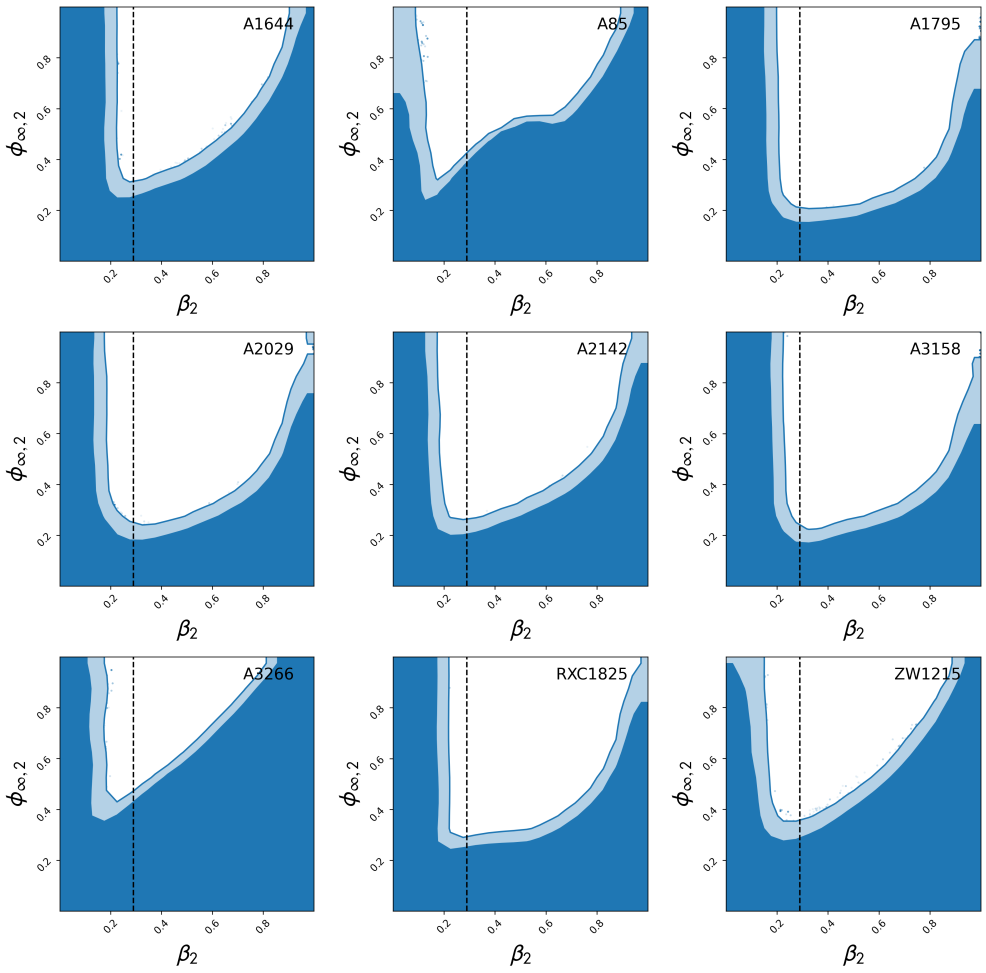

Figure 4.2: $95\%, 99\%$ C.L. contours for all the clusters utilizing the internal mass prior. The vertical line shows the $\beta_2 \sim 0.29$, corresponding to the $f(R)$ scenario where $\beta = \sqrt{1/6}$.

We also point out that in the plots an exponential-shaped bound appears in all of the posteriors of $(\phi_{\infty,2}, \beta)$, which is due to the fact that the formalism inherently takes into account the assumption that the critical radius r_c is a positive quantity. From Equation (4.7) it can be shown that this is equivalent to regions below the curve of the following equation,

$$\phi_{\infty,2} = 1 - \exp\left(-\frac{\beta_2}{1-\beta_2}\frac{\rho_s r_s^2}{10^{-4} M_{\rm Pl}^2}\right), \tag{4.21}$$

As mentioned before, the contours of Figure 4.2 are obtained by adding a prior on the parameter M_{500}. This is because utilizing only the hydrostatic equilibrium data leads to a strong degeneracy in the $\{M_{500}, \beta_2\}$ parameter space, which prevents to place any stringent bounds in most of the cases. In earlier analyses this degeneracy was broken by aiding the hydrostatic data with the mass priors obtained from weak lensing analyses. We further elaborate on this in the Section 4.4.5 (c.f. Figure 4.6).

In order to assess the constraints while excluding this degeneracy we eliminate the lower mass regions by considering a lower limit of $\beta_2 > 0.5$ and constrain the posteriors for the $\{M_{500}, c_{500}\}$, following which we construct the mass and concentration priors, also taking into account the corresponding covariance and re-perform the analysis by expanding the range of $\beta_2 \in (0.0, 1.0)$, as shown in Figure 4.2. Hereon we denote this prior as *internal mass prior* and elaborate in Section 4.4.2. We find that this degeneracy is usually present within $\beta_2 < 0.5$, corresponding to $\beta < 1$, accounting for a decrease in the values of M_{500} while the values of β increase, following the expression of the thermal pressure in Equation (4.14). In clusters A85 and RXC1825 however, we find this degeneracy to extend beyond $\beta > 1$. In particular, for A85, we see that the internal mass prior is completely unable to even reduce the degenerate region.

We then show the quantitative results of our analysis in Table 4.2 we show the results of our analysis for the nine X-COP clusters used in this Chapter. We present in the first column the 68% C.L. of the concentration parameter c_{500} and the mass M_{500} with the internal mass prior elaborated above. We also present the 95% C.L. limits on the value of the field $\phi_{\infty,2}$ for $\beta = \sqrt{1/6}$, which corresponds to the $f(R)$ sub-class of Chameleon model, presented in Section 4.2. In the subsequent columns we present the values at 95% C.L. we obtain for the field $\phi_{\infty,2}$ when imposing the weak lensing mass prior presented in Figure 4.4 and no mass prior, respectively, which we added for completeness. Within parentheses we show the conversion of $\phi_{\infty,2}$ into $|f_{R0}|$ to get explicit constraints on $f(R)$ models. As can be seen, comparing the internal mass prior and no prior scenario, the constraints

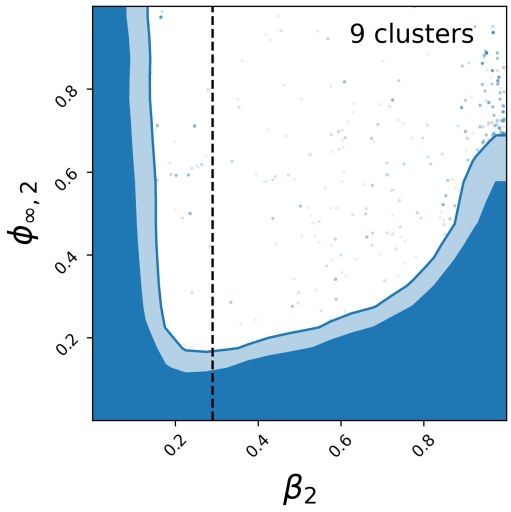

Figure 4.3: 95% and 99% C.L. contours for joint constraint utilizing the internal mass priors for 9 of the clusters. The dashed vertical line represents the $\beta = \sqrt{1/6}$, corresponding to the $f(R)$ scenario.

deteriorate substantially for all the clusters except A85 and A3158. In the case of A85, these posteriors are dominated by the presence of the degeneracy in $\{M_{500}, \beta_2\}$ parameter space. On the other hand, cluster A3158 shows the least observed degeneracy. As for mass profile constraints, c_{500} and M_{500}, presented in the first two columns of Table 4.2, are the same as the GR values up to a 1σ confidence level [178], they are very much in agreement with those estimated for DHOST gravity as presented therein.

One can also notice that in the case where we consider an internal mass prior the constraints get considerably tighter, for instance, the A1795 field value is eight times tighter than the one with no mass prior and three times than the one with the weak lensing prior (which is yet a good constraint compared to the one with no mass prior). Also, we point out that the two-dimensional posteriors are visually much tighter than those previously presented for Coma Cluster [126] and XMM Clusters in [145]. We later perform a more qualitative comparison for the $|f_{R0}|$, in the $f(R)$ scenario.

4.4.1 Constraints using weak lensing mass prior

In this section, we present the constraints obtained on the five clusters for which the weak lensing mass priors are included from the results of [181], namely A1795, A2029, A2142, A85, and ZW1215. While aiding in the analysis as an independent prior on the mass of the cluster, this also reduces the

Table 4.2: Constraints on parameters $\{c_{500}, M_{500}\}$ and $\phi_{\infty,2}$ at 68% and 95% C.L., respectively, from the analysis of each cluster in the sample. The limits are obtained with 3 different methods: from columns two to four, the inclusion of an internal mass prior to avoid the statistical degeneracy between mass and MG parameters, as discussed in Appendix 4.4.5. Column five: WL mass prior - which is available only for five clusters. Column six: no mass prior is taken into account. Note that the bounds on M_{500} and c_{500} are shown only for the first case. The constraints on $\phi_{\infty,2}$ are all presented for $\beta = \sqrt{1/6}$ which corresponds to $f(R)$ gravity. The corresponding bounds on the parameter $|f_{R0}|$ are shown inside the parentheses.

Cluster	Internal mass prior			WL mass prior	No mass prior
	c_{500}	M_{500} $[10^{14}\,M_\odot]$	$\phi_{\infty,2}(\lvert f_{R0}\rvert\,[10^{-5}])$		
A85	$2.05^{+0.07}_{-0.07}$	$6.13^{+0.18}_{-0.18}$	0.272 (2.592)	0.279(2.671)	0.276(2.637)
A1644	$1.13^{+0.11}_{-0.14}$	$2.95^{+0.20}_{-0.20}$	0.226 (2.092)	/	0.942(23.25)
A1795	$3.17^{+0.14}_{-0.14}$	$4.48^{+0.15}_{-0.15}$	0.146 (1.289)	0.319(3.137)	0.874(16.91)
A2029	$3.20^{+0.13}_{-0.13}$	$7.70^{+0.24}_{-0.24}$	0.208 (1.904)	0.396(4.117)	0.942(23.25)
A2142	$2.22^{+0.08}_{-0.08}$	$8.32^{+0.19}_{-0.19}$	0.198 (1.802)	0.213(1.956)	0.498(5.627)
A3158	$1.98^{+0.14}_{-0.14}$	$3.96^{+0.16}_{-0.16}$	0.216 (1.987)	/	0.281(2.694)
A3266	$1.61^{+0.11}_{-0.11}$	$7.21^{+0.28}_{-0.32}$	0.245 (2.295)	/	0.804(13.30)
RXC1825	$2.54^{+0.20}_{-0.24}$	$3.90^{+0.17}_{-0.15}$	0.146 (1.289)	/	0.358(3.619)
ZW1215	$1.40^{+0.09}_{-0.09}$	$7.43^{+0.29}_{-0.29}$	0.342 (3.417)	0.892(18.17)	0.567(6.834)
Joint	–	–	0.106 (0.915)	0.130 (1.139)	–

aforementioned degeneracy between the $\{\beta_2, M_{500}\}$ parameters. The constraints on the modified gravity parameters are shown in Figure 4.4. Note that for the cluster ZW1215 alone the inclusion of the WL prior does not aid

the constraint and on the other hand, slightly deteriorates the upper limits. This is clearly the case, as the prior itself is an estimated lower value aiding the degeneracy region, with a mass of order $3.5\,[10^{14}\,M_{\odot}]$ [3]. However, this does not hinder our ability to constrain the modified gravity parameters in the joint analysis, as discussed in Section 4.4.3. And it is apparent that the degeneracy that remains in the A85 cluster does not affect the joint constraint being guided by the other cluster.

As expected, we notice that the WL mass prior is capable of reducing the degeneracy elaborated earlier and making the posteriors in the $\{\phi_{\infty,2}, \beta_2\}$ slightly more constrained. Note however that the WL mass estimates do present a mass bias ($\mathrm{b} = M_{500}^{\mathrm{WL}}/M_{500}^{\mathrm{HS}}$) which is slightly larger than unity ($b \sim 1.18 \pm 0.12$) [137] at R_{500}. However, in terms of the constraints, even the inclusion of the WL mass prior is not able to remove the degeneracy completely, which can be seen as a mild bump in the posteriors presented in Figure 4.4. This is clearly due to the larger uncertainties on the WL masses in comparison to the constraints on M_{500} obtained from the hydrostatic equilibrium. Our formalism here validates that having a well-constrained independent mass estimate from the WL method, where the weak lensing potential is unaffected by the chameleon gravity and can be very beneficial for constraining the parameters.

4.4.2 Parameter degeneracy

Alongside obtaining the constraints on $\{\phi_{\infty,2}, \beta_2\}$ parameters, we also comment on the degeneracy(s) that we notice between the cluster mass profile parameters and the modified gravity parameters. As can be seen in Figure 4.6, an increase in β_2 or $\phi_{\infty,2}$ is compensated by lower values of M_{500}. This is not surprising, given the structure of the modified Newtonian potential in Equation (4.14). This degeneracy is also visible in the marginalized posterior distribution of $\phi_{\infty,2}$ and β_2 as a bump, highlighting the necessity of a mass prior to hydrostatic equilibrium data. In fact, we can notice that the degeneracy reduces as soon as we add additional information on M_{500}, and the tighter this mass prior, the lesser the degeneracy we have. Earlier hydrostatic equilibrium analysis which always considered the WL counterpart did not find such a degeneracy, for instance using COMA cluster in [126] and XMM cluster in [145].

We can also see this quantitatively from the condition we impose in our model to estimate the *screening* radius, which gives a direct relation be-

[3] Note that [181] also present the weak lensing mass for the ZW1215 cluster, including others using varied methods, which is higher $\sim 7 \times 10^{14}[M_{\odot}]$.

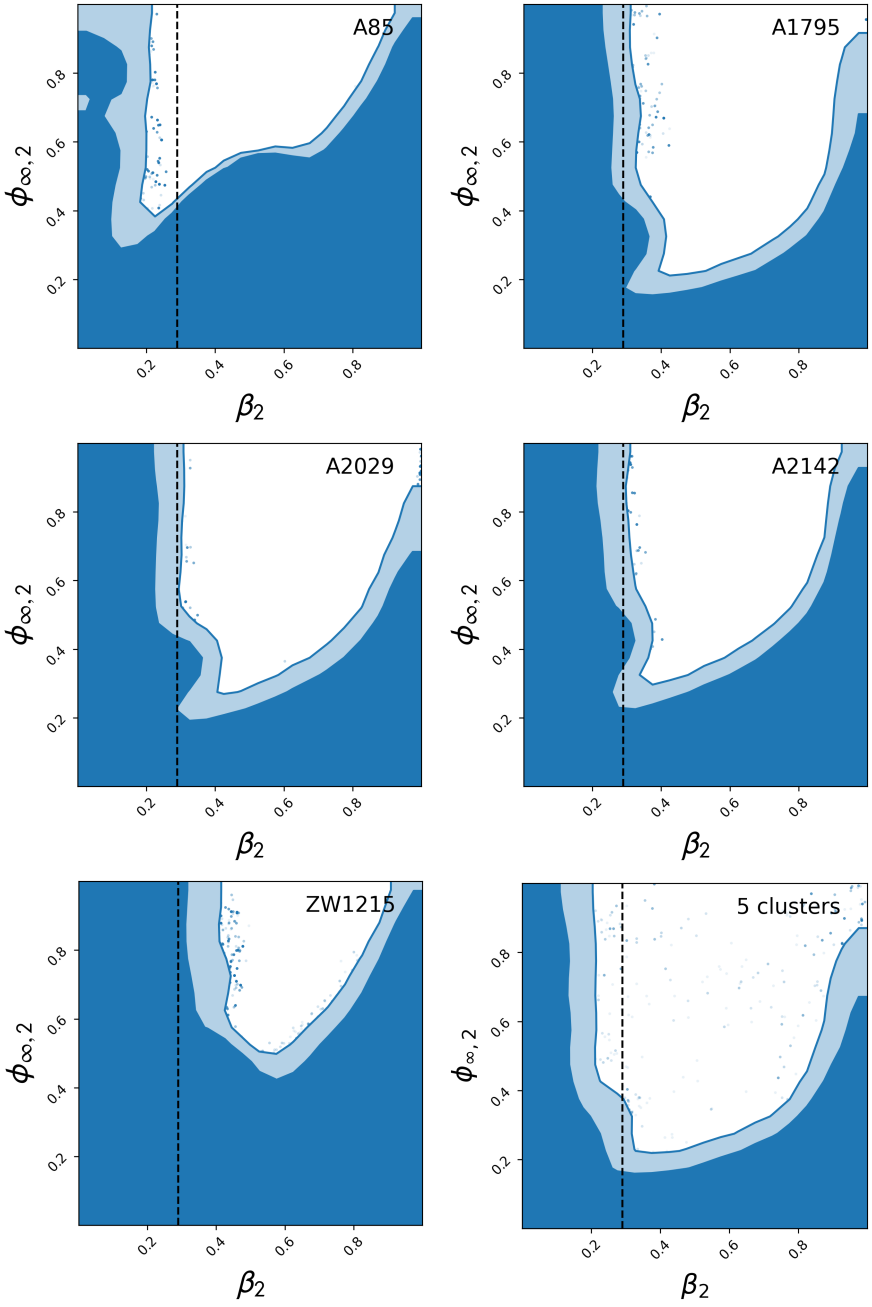

Figure 4.4: 95% and 99% C.L. contours for weak lensing priors for 5 of the clusters. In the lower right panel, we present the joint constraint obtained by combining all five clusters. The dashed vertical line represents the $\beta = \sqrt{1/6}$, corresponding to the $f(R)$ scenario.

tween M_{500} and β. In particular, replacing Equations (4.19) and (4.20) into Equation (4.7) one can write,

$$1 + \frac{r_c}{r_s} \sim \frac{1}{M_{500}^{-5/2}} \frac{\beta}{\phi_\infty} f(c_{500}) \tag{4.22}$$

Here $f(c_{500})$ is a function that only depends on the shape of the profile (c_{500}). At this stage, if we impose the condition that maps all negative r_c to $r_c \sim 0$ we get from above $\frac{\beta}{\phi_\infty} \sim M_{500}^{-5/2}$, this means that when the coupling constant β is low, the mass gets higher, which creates a region where the higher the mass, the lower the coupling and vice versa, as can be seen in Figure 4.6. Also within the hydrostatic equilibrium equation, the contribution of the gravitational force and the fifth force, are scaled by M_{500} and β, respectively. The summation of these two forces provides the derivative of the pressure and not knowing the integration constant $P(r = 0)$ beforehand allows only the shape to be constrained and hence the degeneracy between these two forces is propagated to the corresponding parameters.

One can also notice in the $\{\phi_{\infty,2}, M_{500}\}$ plot of Figure 4.6 that the same degeneracy holds: lower values of the mass correspond to slightly higher $\phi_{\infty,2}$ (equally ϕ_∞). This region appears only for low mass values and coupling constant $\beta_2 < 0.5$ (i.e., $\beta < 1.0$). As for the higher masses limit, this degeneracy disappears with the coupling strength approaching $\beta_2 \to 0$. Therefore to avoid such a statistical degeneracy we construct an internal mass prior based on the mass values we get for $\beta_2 > 0.5$ and then run the MCMC chain again to get the new posteriors, and this will erase the degeneracy issue as shown in Figure 4.2. Alternatively, adding the WL mass prior will remarkably reduce the degeneracy region as shown in Figure 4.6 and the posteriors are shown in Figure 4.4.

4.4.3 Joint analysis

Considering that the clusters utilized in the analysis are independent datasets, we explore the possibility to obtain joint constraints on the modified gravity parameters $\{\phi_{\infty,2}, \beta_2\}$. In principle, the background field should evolve in cosmic time. However, given the small redshift range ($0.04 \leq z \leq 0.09$) spanned by the sample, we can safely neglect any redshift dependence and assume $\phi_\infty(z) \sim \phi_\infty(z = 0)$, essentially constraining the local value of the field. In Figure 4.3 and the lower right panel of the Figure 4.4, we show the joint constraints using 9 clusters and 5 clusters with the WL mass priors, respectively. Firstly, the overall posterior parameter space in Figure 4.3 is greatly reduced when the 9 clusters are combined displaying the ability of

the current hydrostatic data to constrain the chameleon screening model, improving the constraints from the earlier analysis in [126, 145]. Note that the internal mass prior plays a very important role in allowing such tight constraints. The joint constraints using the 5 clusters using the WL mass prior as well is a tighter constraint with a mild residual of the degenerate region.

4.4.4 Joint constraints on $f(R)$ gravity

In the following we use the results of our joint analysis of the chameleon parameter space to place constraints on the background *scalaron* field f_{R0}, neglecting the redshift dependence. Starting from the joint posteriors of Figure 4.3 and Figure 4.4, we consider the slice of parameter space $(\beta_2, \phi_{\infty,2})$ for a constant value of $\beta_2 \sim 0.29$ (i.e. $\beta = 1/\sqrt{6}$). We then derive the corresponding posterior $P(\phi_\infty|\beta = 1/\sqrt{6})$, which is further related to f_{R0} as a particular case of the chameleon coupling, discussed at the end of Section 4.2. In Figure 4.5 we plot the distributions $P(f_{R0})$ for the nine-clusters joint case, assuming internal mass priors (*top*), and for the combination of five clusters with weak lensing priors on M_{500} (*bottom*). The colored areas in gray indicate the regions corresponding to the 95% C.L. As already mentioned, the mass priors play a fundamental role in breaking the degeneracy among the model's parameters. In the case of weak lensing information, the priors are not sufficient to remove all the degeneracy, resulting in a bump in the *scalaron* distribution of individual clusters. Although the individual clusters in the case of WL priors show a bimodal distribution (except for A85), the joint analysis however is capable to providing a tighter constrain owing to the fact that the second mode in the posterior distribution is spread across the values of the $\phi_{\infty,2}$ and consequently in f_{R0}. As our final constraints, we quote,

$$|f_{R0}| < 9.1 \times 10^{-6}\,,$$

at 95% C.L. for the nine-clusters combined analysis, and similarly

$$|f_{R0}| < 1.1 \times 10^{-5}\,,$$

for the five-cluster weak lensing case.

Within the posteriors of the $\phi_{\infty,2}$ shown in the bottom panel of the Figure 4.5, one could distinguish three distinct contributions (except for A85). The first peak which mainly contributes to joint constraint is marginalized for M_{500} that does not include the degeneracy, with either of $\{\phi_{\infty,2}, \beta_2\}$. While the second peak is an outcome of slightly lower masses, and larger values of

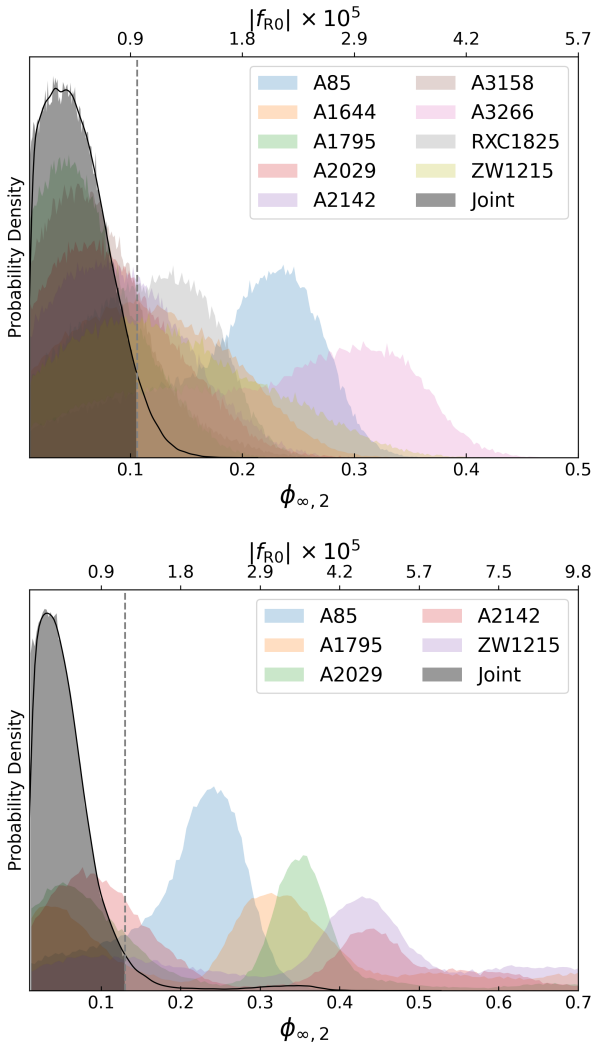

Figure 4.5: Probability distributions for $\phi_{\infty,2}$ (f_{R0} depicted on the top axis) obtained for the specific case of $\beta = 1/\sqrt{6}$ for all the clusters within the compilation and the consequent 95% C.L. regions for the joint analysis (shaded in gray). *Top*: 9 clusters with an internal mass prior. *Bottom*: 5 clusters for which a WL mass prior was available. Please note the difference in the limits of axes in the two figures.

the c_{500} parameter, essentially implying a modification to the shape of the mass profile. Finally, the extended tail of the distribution seen for $\phi_{\infty,2} > 0.5$ is due to the mild degeneracy between $\{\phi_{\infty,2}, M_{500}\}$, for even lower values of M_{500}. However, in the joint analyses, the latter two features do not amplify being varied nonoverlapping distributions.

Earlier in [126], a constraint of $|f_{R0}| < 6 \times 10^{-5}$ was set using the hydrostatic and weak lensing observables of the coma cluster at $z = 0.02$, which is even more local compared to the redshift range $z \in \{0.04, 0.09\}$ of current X-COP clusters. In this context all the individual clusters in the current analysis provide a tighter constraint (see column 4 of Table 4.2) and almost an order tighter joint constraint when combining all the data. Our constraint here is also tighter w.r.t. the 58 stacked cluster analysis in [145], which considers XMM cluster survey and CHFTLenS weak lensing observations in a large redshift range of $z \in \{0.1, 1.2\}$. In principle, such a joint analysis does not consider cosmological evolution in the field. Other works that used galaxy clusters estimated $|f_{R0}| < 10^{-5}$ (e.g. [170, 171]); moreover, [158] forecasted a value of $|f_{R0}| < 10^{-6}$ from the combination of lensing and kinematics mass profile reconstructions of a reasonable sample (~ 10) of clusters. Our analysis confirms that constraints of the same order of magnitude can be reached with a combination of high-quality X-ray cluster data with physically motivated priors in the cluster masses. It is also worth noticing that the bounds derived here are *model-independent*, i.e. no particular functional form for $f(R)$ has been assumed.

4.4.5 Effects of Mass prior

In this Section, we briefly comment on the different priors choices and systematics due to the electron density data modeling, considering cluster A2142 as an exemplar. In fig. 4.6, we compare the posteriors obtained with and without the inclusion of the mass priors. The strong degeneracy between the mass of the cluster (M_{500}) and the chameleon parameters, can be clearly noticed in the contours shown in blue, deforming the 2-dimensional Gaussian expectation in the M_{500} parameter space. When the WL mass prior is added (shown in red), the degeneracy region shrinks providing more exclusion region in the chameleon parameters. This is completely independent of any analysis choices made and only due to the WL mass prior which is an independent observable, therefore aiding to the constraints. In blue, we show the posteriors when the internal mass prior is considered. As elaborated in Section 4.4, this prior is taken from the posterior, when the MCMC analysis is performed with a $\beta_2 > 0.5$ limit. And as expected the mass degeneracy is completely eliminated finding much tighter constraints in the exclusion

region. Note that both the mass priors do not modify the constraints of the chameleon parameters for $\beta_2 > 0.5$.

4.4.6 Effects of gas mass and fixing density (n_e) profiles

In Figure 4.7, we show as an example the comparison of the contours showing the constraints when the electron density parameters are allowed to vary in MCMC analysis against the case when they are fixed to the mean values obtained from the former case. We find that the uncertainty in the electron density parameters does not add to the overall uncertainty in the chameleon parameter space. This can be understood straightaway as there is no expected coupling to the gas density and the mass profile of the dark matter is modeled via the NFW profile and is assumed to be equivalent to the total mass of the cluster. Noting this as an advantage, we first perform the analysis marginalizing the electron density parameters and later fixing them to obtain our final results presented in Section 4.4. This essentially helps to span the $\{\phi_{\infty,2},\, \beta_2\}$ parameter space effectively in comparison to the case when all the 10 parameters are allowed to vary, where the posteriors might be affected by the sampling methods.

As discussed earlier in Section 4.2, we test for the possibility to model the gas mass and the dark matter components separately assuming that only the dark matter couples with the chameleon field. We show the results of the same in Figure 4.8, which can be contrasted against Figure 4.6 for the same cluster assuming one mass profile that models both the gas and dark matter components coupled to the field. We verify that this scenario, which is capable of mildly addressing the degeneracy between the M_{500} and the β_2 parameter, eventually does not affect the final constraints on the chameleon parameters. Also reflecting as a change in the vertical cutoff for the lower values of β_2, which is partially due to the reduction in degeneracy. Also implying that when the coupling between the baryons (gas) and chameleon is not accounted for correctly, considering a single mass profile as a proxy for both dark and baryonic components is a more conservative approach.

4.4.7 Alternative weak lensing mass priors

As noted earlier in Sections 4.3 and 4.4, [181] provide weak lensing mass estimates using both the NFW density profile assumption ($M_{500}^{\rm NFW}$) and an alternative method, fitting the mean convergence within an aperture radius ($M_{500}^{\rm ap}$), which is independent of the mass profile assumptions. Firstly, we

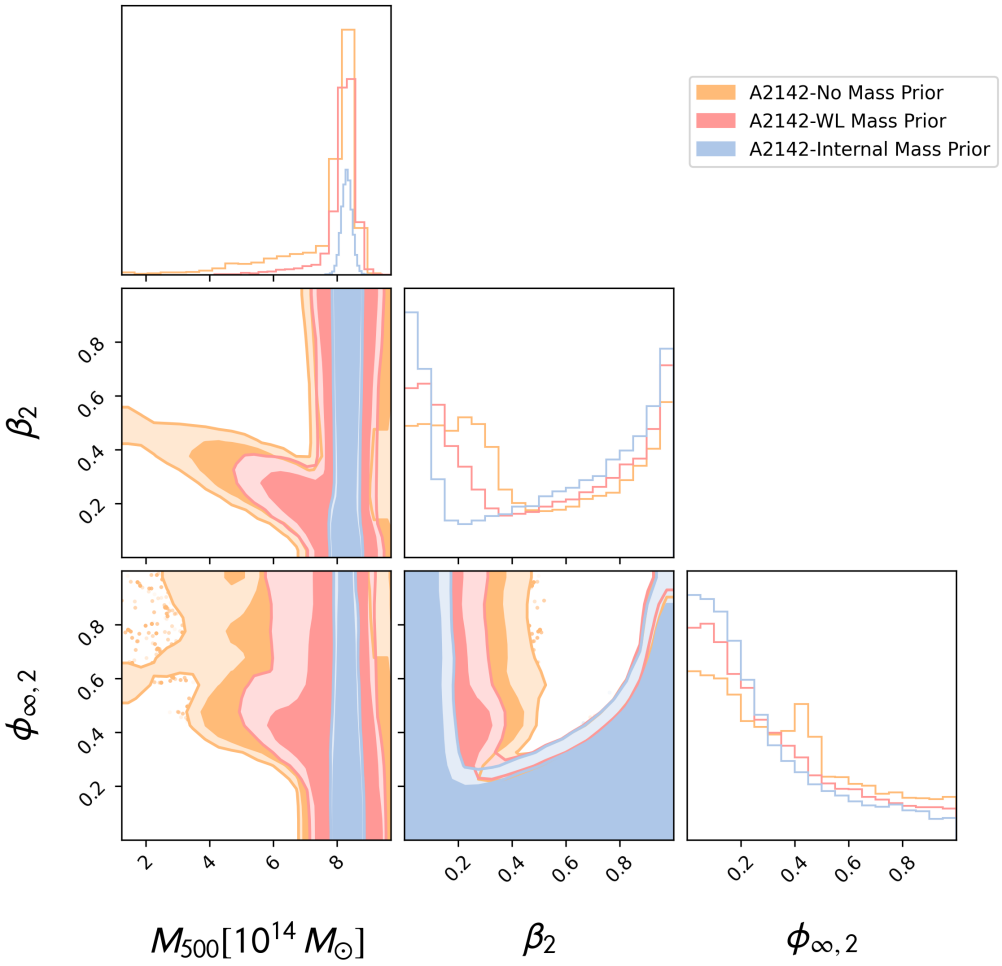

Figure 4.6: We show the 95% and 99% C.L. contours for A2142 cluster, where the orange contours represent the ones with no mass prior is taken into account, the red ones with the weak lensing mass prior and the blue ones correspond to the internal mass prior case . We notice that the degeneracy region gets reduced when we have an additional mass prior.

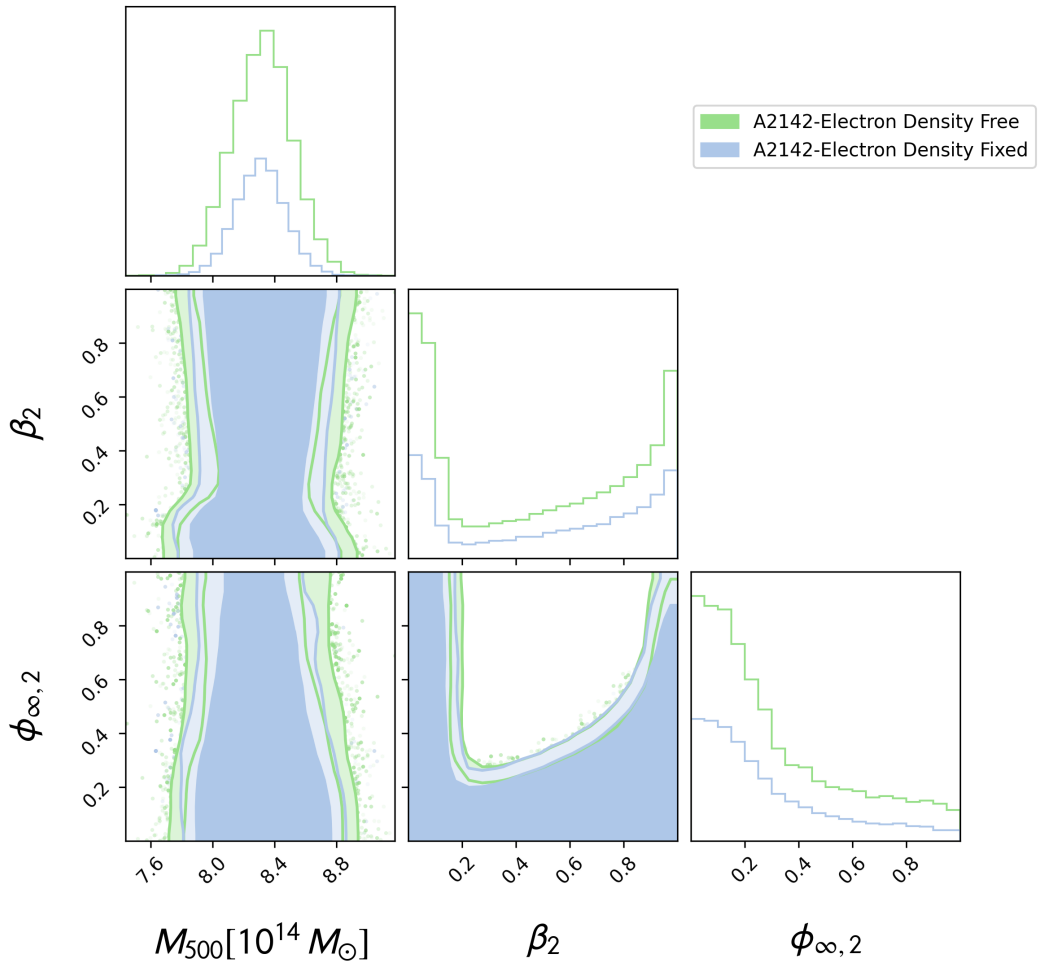

Figure 4.7: We show the 95% and 99% C.L. contours for A2142 cluster, wherein the blue contours represent analysis where electron density parameters are fixed. The green contours show the case where the electron density parameters are marginalized upon.

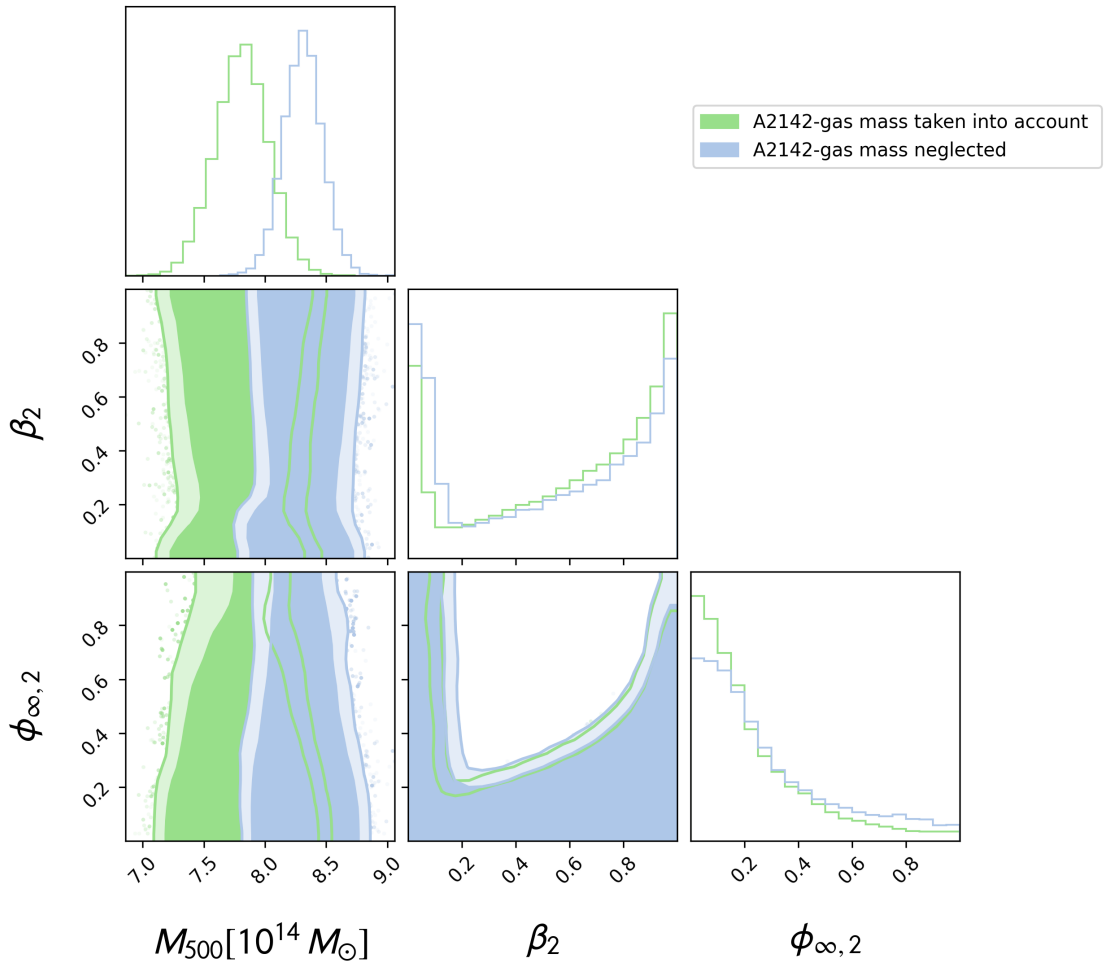

Figure 4.8: We show the 95% and 99% C.L. contours for A2142 cluster, wherein the blue contours represent analysis where the gas mass is neglected. The green contours show the case where the gas mass is taken into account in the total pressure.

notice that the two masses presented therein are mostly in agreement, and utilizing either of them does not change our final constraints, except for the cluster ZW1215 with $M_{500}^{\rm ap} \sim 2 \times M_{500}^{\rm NFW}$. We validate that replacing the ZW1215 prior in Table 4.1 with the higher $M_{500}^{\rm ap}$, considerably improves the exclusion region, however, the joint constraint remains unaltered. Therefore, we remain to present our final results with the WL mass priors as the values of M_{500} found assuming the NFW mass profile.

4.4.8 $c(M)$ relationships as priors

Since two of the main parameters in our study are c_{500} and M_{500}, we can straight away compare our constraints with the well-established scaling relationships between the concentration c_{200} and the corresponding mass M_{200} in galaxy clusters [185, 186]. These relations can be extended to the case of Modified Gravity namely in the case of Hu-Sawicki $f(R)$ model used above, see [187, 188]. As elaborated in [187] the current relation [185] holds also for all but low masses at low redshifts and within the $f(R)$ case considering small values of $|f_{R0}|$. Both these conditions are met for the nine clusters used in our analysis (see Table 4.2). Since we have this well-known relation between the concentration and the mass validated against the independent analyses of the clusters, one could utilize it as a prior when assessing the modified gravity parameters, perhaps eliminating some degeneracy in the posteriors. However, note that the dispersion of the scaling relation is larger by an order $\gtrsim 2$ for at least 6 of the clusters which are well within the 1σ region, and for 3 other clusters the constraints are in agreement at $\sim 2\sigma$. We show a comparison of our constraints and the scaling relation taken from [186] in fig. 4.9, for the case without any mass prior and with the internal mass prior, in open and filled markers, respectively. We see from the plot that the internal mass prior shifts the masses towards higher values and makes the mass tighter (see section 4.4.2), as expected. However, this also validates that adding the scaling relation as a prior would have a mild to no effect on the position of these clusters in the $c(M)$ space. Note for example, that cluster A1644 which is the most discrepant with respect to the scaling relation also prefers a mass model other than NFW [137]. Therefore, we defer the analysis utilizing the scaling relation as prior to future work, assessing also the effects of assumed mass models on mass and modified gravity parameters, simultaneously.

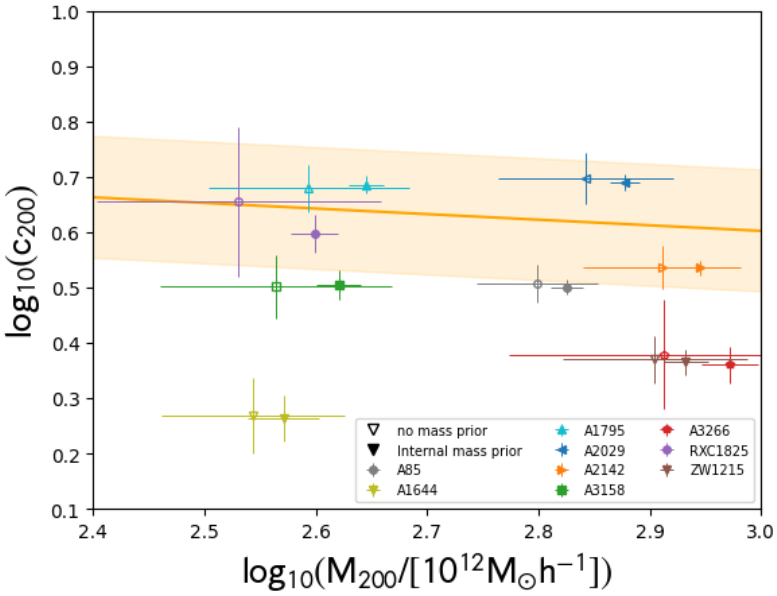

Figure 4.9: We plot the $c_{200}(M_{200})$ relation against the nine cluster in our analysis. The solid orange line represents the relation in [186] with a lognormal scatter of 0.11 dex shown as the shaded region.

4.5 Conclusion

In this Chapter, we have implemented a formalism which follows what it has been done in previous works [126, 145], to test the Chameleon screening in galaxy cluster utilizing the hydrostatic equilibrium data. We have constrained the two parameters describing the Chameleon field, the coupling constant β and the value of the field at infinity ϕ_∞ by analyzing the dynamics of 9 galaxy clusters in the X-COP sample. The Chameleon field manifests as a fifth force beyond a certain critical screening radius within a cluster that adds up to the gravitational potential. By performing a full Bayesian analysis of the X-ray-emitting gas pressure and the SZ pressure, along with the electron density, we obtain limits on the aforementioned parameters, essentially excluding a part of the parameter space for this modified gravity scenario. We summarize the results as follows.

- We find that adding a physically motivated mass prior to our analysis will give a remarkably tight constraint, breaking the degeneracy among model parameters (see also Section 4.4.5). For instance, as the main result we present, Figure 4.2, where we construct an internal mass prior by eliminating the low mass degenerate regions and use the posterior

as a prior in the new MCMC chains, obtaining very tight constraints on $\{\beta, \phi_\infty\}$ compared to previous analysis of Coma Cluster [126] and stacked analysis of XMM Clusters [145].

- We have then included additional information on M_{500} from weak lensing analysis in [181] (see Figure 4.4). While the results are comparable to what we obtained with the internal mass prior, the weak lensing data are not tight enough to remove the degeneracy completely.

- We present our final results in Table 4.2 where we show all the constraints obtained using different mass priors and report a joint constraint eventually on the $f(R)$ class of models presented in Section 4.2.

- We note that marginalizing or fixing the electron density profile shows no effect on the constraints obtained for the chameleon parameters (see Figure 4.7).And briefly discuss the change in constraints when gas mass is included in the analysis without being coupled to the Chameleon field.

It is worth pointing out that we have considered only clusters for which the total mass profile (in GR) is well described by the NFW model. Although this choice is physically well motivated, it is important to explore the effect of different mass parameterizations that may better describe the total matter distribution within galaxy clusters in theories of gravity alternative to GR. Indeed the NFW model, despite its wide range of applicability over different scales, might not be the best profile to reproduce the mass distribution of halos in a modified gravity scenario (see e.g. [189] and references therein). In particular, the efficiency of the screening mechanism in chameleon gravity is strictly dependent on the mass model, as one can see from Equation (4.4). Finally, in Section 4.4.8 we make a validation of our constraints with the concentration-mass scaling relation present in the literature.

Chapter 5

Mass modeling of Galaxy Clusters in Modified Gravity

In the previous chapter, based on an analysis already performed in [137], the NFW mass density profile was assumed to describe the total mass density distribution of a compilation of galaxy clusters[137]. Nevertheless, this assumption was valid in the GR context only for 9 of the clusters. For the rest of them, the NFW mass density profile is not the preferred model, for instance, favouring an Isothermal or a Hernquist mass profile. This preference for a different mass mode other than NFW can yield a strong effect on the Chameleon field profile – and resulting fifth force – with the shape of the matter density. Allowing one to test the rich phenomenology of the screening mechanism at galaxy cluster scales for additional mass density models is tantamount.

In this Chapter we investigate the effect of the mass modeling when constraining Chameleon gravity at cluster scales by current mass measurements. In order to test the viability and effect of several mass density models on the Chameleon screening, we first implement a semi-analytical approximation to obtain the solution of the Chameleon field equation for six different mass model assumptions. The semi-analytical approximation provides a rather simple and computationally cost-efficient way to implement the screening mechanism for operative purposes, with respect to the full numerical solution. Moreover, it is a powerful tool to study the relationship among the parameters of the mass profile and of the Chameleon field, highlighting the main physical properties of the screening mechanism. To validate our semi-analytical approach we also perform a comparison with a full numerical solution, successfully confirming that the former can adequately reproduce the behavior of the fifth force.

The Chapter is structured as follows: section 5.1 reviews the basic the-

ory of the Chameleon gravity and the screening mechanism, further presenting the mass models adopted and the semi-analytical approximation in section 5.1.1 and section 5.1.2, respectively. In section 5.2, the solutions for the field profile and its derivative are displayed and tested against the numerical solutions in section 5.3. In section 5.4 we present the constrains obtained on two remaining clusters that prefer Isothermal mass profile.

5.1 Theory

The Chameleon field theory [108], and respective phenomenological effect, are studied in the context of galaxy clusters obeying the assumptions: *i)* the cluster possesses radial symmetry, and *ii)* both dark matter and baryonic matter are modelled with the same total mass profile [4]. Let us start by describing the Chameleon mechanism.

5.1.1 Mass models

In order to describe the mass distribution of a galaxy cluster, one has to resort to a mass density profile, ρ. So far, the majority of the studies of Chameleon gravity at cluster scales in the literature relied on the standard NFW density model. However, not all galaxy clusters are best described by the latter[1] Bayesian evidence $\lesssim 2.5$.. It is then tantamount to extend the analysis to alternative mass density models, and explore the respective Chameleon screening phenomenology in order to assess its constraints and thus investigate whether such mass models could be validated in the CG context.

As stated, while the NFW mass density model is able to provide an adequate fit to the total mass distribution of galaxy clusters, some discrepancies have been found, both in simulations and observations, concerning the inner shape of cluster-size halos (*e.g.* [190, 191]) especially when baryonic feedback is considered. Moreover, it is not completely clear if the NFW mass density model is a good description of halos in modified gravity scenarios (see *e.g.* [189] and references therein), even if some works indicate that it performs well in reproducing the mass distribution in chameleon gravity (*e.g.* [154]).

In this Chapter, besides the NFW profile, five additional mass-density models will be considered. These are: *b*NFW [192], generalised NFW [193] (*g*NFW), Burkert [194], Isothermal [195] and Einasto [196]. All these mass density models are characterized by a central density, $\rho_{\rm s}$, and a scale radius,

[1]Bayesian analysis done in [137], suggests that the three clusters in the GR case prefer either Isothermal and Burket profiles, albeit a weak preference, with the change in

r_s, which vary between halos of different sizes. To solve the field **??**, we apply and generalise the same method as earlier implemented in [126, 197, 4, 158, 166], which can be summarized as follows.

Assuming radial symmetry, the procedure relies on a semi-analytical approximation (see [192]) by solving **??** in the outskirts of the galaxy cluster where the Chameleon field becomes important (low-density regime). The Chameleon field is assumed to be negligible in the innermost region, where the field is screened (high-density regime). The transitional screening radius between the two regions, r_c, can be determined by imposing the continuity of $\phi(r)$ and its first derivative at r_c (*aka* junction condition). The resulting screening equation relates the parameters of the Chameleon model (β and ϕ_∞) and that of the mass model (ρ_s and r_s).

The aforementioned NFW profile is described by,

$$\rho(r) = \frac{\rho_s}{\frac{r}{r_s}\left(1+\frac{r}{r_s}\right)^2} , \tag{5.1}$$

which, while simple, has been extensively used to describe the mass distribution of galaxy clusters and constrain the parameters of the Chameleon field.

A straight forward extension of the NFW profile – (bNFW [192]) – is obtained by considering a generic integer exponent $b > 2$ in the denominator of eq. (5.1)[2]:

$$\rho(r) = \frac{\rho_s}{\left(\frac{r}{r_s}\right)\left(1+\frac{r}{r_s}\right)^b} . \tag{5.2}$$

Another, more advanced, generalization of the NFW model is the *generalised* NFW (gNFW) profile, which is characterized by a real slope $0 < \gamma < 2$ as

$$\rho(r) = \frac{\rho_s}{\left(\frac{r}{r_s}\right)^\gamma\left(1+\frac{r}{r_s}\right)^{3-\gamma}} . \tag{5.3}$$

The second distinct mass density profile under consideration is the so-called Burket profile [194],

$$\rho(r) = \frac{\rho_s}{\left(1+\frac{r}{r_s}\right)\left[1+\left(\frac{r}{r_s}\right)^2\right]} . \tag{5.4}$$

[2]For $b = 3$ this is the so-called Hernquist profile [198].

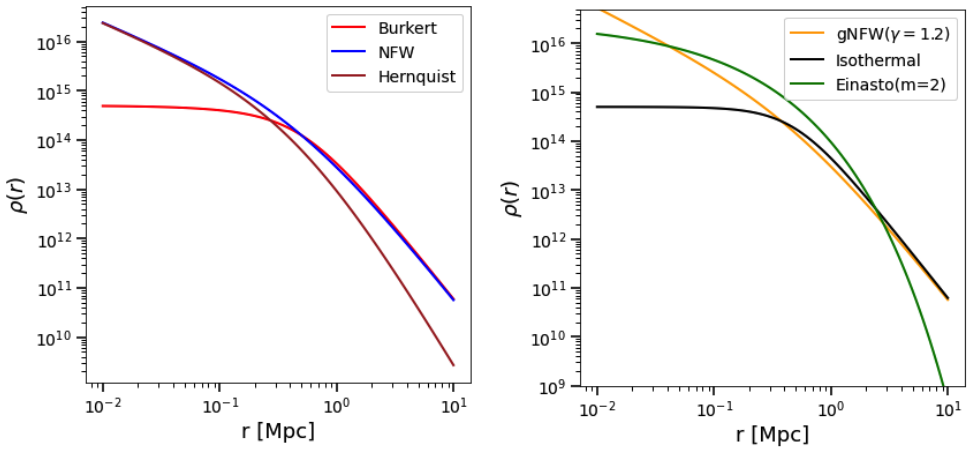

Figure 5.1: Density profile models, for a halo with $\rho_s = 5 \times 10^{14} M_\odot/\mathrm{Mpc}^3$ and $r_s = 0.5\,\mathrm{Mpc}$. Left: Burkert, NFW, Hernquist (b-NFW with $b = 3$); Right: gNFW with $\gamma = 1.2$, Isothermal and Einasto with $m = 2$.

The Isothermal mass density model [137, 195] is described by

$$\rho(r) = \frac{\rho_s}{\left[\left(\frac{r}{r_s}\right)^2 + 1\right]^{3/2}} \,. \tag{5.5}$$

Finally, the Einasto model [196] comes as,

$$\rho(r) = \rho_s \exp\left\{-2m\left[\left(\frac{r}{r_s}\right)^{\frac{1}{m}} - 1\right]\right\} \,, \tag{5.6}$$

where $m \in \mathbb{N}$ is a characteristic exponent.

In Fig. 5.1 the density profiles for all the models introduced above are shown for a reference value of the critical density $\rho_s = 5 \times 10^{14} M_\odot/\mathrm{Mpc}^3$ and a scale radius $r_s = 0.5\,\mathrm{Mpc}$. The Isothermal, Burkert and Einasto profiles flatten to a constant value for $r \to 0$, while the NFW and its generalizations exhibit a cusp, diverging at small radii. Increasing b in the b-NFW models provides a faster suppression of the density at large r, whereas an increase of the m parameter in the Einasto model results in a shallower profile. In total, the set of density models captures a quite broad range of behaviors. While there are additional assumptions that one could utilize for the mass density profiles of galaxy clusters, we find the above selection to be sufficiently extensive for the current analysis: test the effect of the Chameleon mechanism on the shape of the mass distribution.

5.1.2 Field solutions

As a recall, eq. (4.3) is solved by considering two regions. Deep within the massive source – the centre of the galaxy cluster (high-densities) –, the scalar field is everywhere close to its minimum value, and field gradients are negligible $\nabla^2\phi \approx 0$ (see *e.g.* [108] for details). Thus, from eq. (4.3) and assuming the power-law potential, the scalar field inside the source can be approximated as,

$$\phi_{\rm int}(r) \approx \left(\beta \frac{\rho(r)}{n\Lambda^{4+n}M_{\rm Pl}}\right)^{-\frac{1}{n+1}} , \tag{5.7}$$

where the absence of gradient at the centre of the mass distribution effectively screens the fifth force (see below), assuming $\phi_{\rm int}(r) \simeq 0$ and hence $\phi_{\rm int}(r) \ll \phi_\infty$ in the following. On the other hand, towards the outskirts of the source, the gradient of the field grows and leads to a fifth force given by

$$F_\phi = -\frac{\beta}{M_{\rm Pl}}\frac{{\rm d}\phi}{{\rm d}r} . \tag{5.8}$$

Wherein the above expression corresponds to a faraway region from the massive body – low-density regime – and the Laplacian term dominates over the field's potential, which decreases quickly (*i.e.* $\partial V(\phi)/\partial\phi \ll \nabla^2\phi$). The equation of motion for the Chameleon field in this region can then be expressed as,

$$\nabla^2\phi_{\rm ext} \approx \beta\frac{\rho}{M_{\rm Pl}} . \tag{5.9}$$

Assuming that the matter density model can be written as $\rho(r) = \rho_{\rm s}\, f(x)$, where $x = r/r_{\rm s}$, which is valid for all the mass models presented above, eq. (5.9) can be expressed as

$$x^2\frac{{\rm d}\phi_{\rm ext}}{{\rm d}x} = \frac{\beta r_{\rm s}^2\rho_{\rm s}}{M_{\rm Pl}}\int f(x)\, x^2\, {\rm d}x + C_{\rm s} , \tag{5.10}$$

where $C_{\rm s}$ is an integration constant. We now distinguish two cases: *a*) when the field in the interior region is screened (the aim of this work) and *b*) when it does not reach the minimum of the effective potential (*i.e.* no interior solution). Case *b*) is equivalent to a zero screening radius – or negative – thus, $\phi(r)$ will not be screened, and the 'exterior' solution is valid everywhere. The constant of integration in this scenario can be determined by fixing the boundary conditions.

The gravitational potential, Φ, in Chameleon gravity, comes as,

$$\frac{\mathrm{d}\Phi}{\mathrm{d}r} = \frac{GM(r)}{r^2} + \frac{\beta}{M_{\rm Pl}}\frac{\mathrm{d}\phi}{\mathrm{d}r} = \frac{G}{r^2}\left[M(r) + \frac{\beta}{G\,M_{\rm Pl}}\,r^2\,\frac{\mathrm{d}\phi}{\mathrm{d}r}\right]$$
$$\equiv \frac{G}{r^2}\left[M(r) + M_{\rm eff}(r)\right] \ , \tag{5.11}$$

i.e., up to a constant, the field gradient times r^2 acts as an additional effective mass contribution sourced by the fifth force. As such, one can require that this contribution is zero when the mass profile itself is zero at $r \to 0$. In other words, the field gradient should diverge slower than r^2 at the origin. In the case of a screened field, the integration constant is obtained by imposing continuity at the screening radius $r_{\rm c}$: a match between the inner and the outer profiles and the first derivative(s).

5.2 Solutions for different mass profiles

In this section, a brief description of the formalism to obtain the semi-analytic solutions of the field and its derivatives is provided, for the different mass density models considered here. For notation simplicity, $\mathcal{B} = \beta\rho_{\rm s}r_{\rm s}^2/M_{\rm Pl}$ is introduced. Schematically, the procedure for computing the semi-analytic solution for any mass density model is as follows: i) obtain the exterior solution for the field as defined in eq. (5.9), assuming spherical symmetry, which depends on two free parameters $r_{\rm c}$ and $C_{\rm s}$, ii) these two free parameters are now obtained by fixing the boundary conditions at $r = r_{\rm c}$ within which the field is assumed to be negligible. Now one can put together interior $\phi_{\rm int}(r)$ and the $\phi_{\rm ext}(r)$ to obtain the solution of $\phi(r)$ in the entire radial range of the object and outside.

5.2.1 NFW-type solutions

The expression for the chameleon field in the case of NFW and *b*NFW has already been presented in previous works (*for instance,* [192, 145, 158]). For the sake of brevity, we briefly review the spherical solution to the field outside the screening where $r > r_c$, further providing the matching conditions (*i.e.* the screening equation) with the interior solution $\phi_{\rm int} \simeq 0$. The field gradient, which enters in the expression of the fifth force is given by,

$$\frac{\mathrm{d}\phi_{\rm ext}}{\mathrm{d}r} = \frac{(x+1)^{1-b}(x-bx-1)}{x^2(b-1)(b-2)}\mathcal{B} + \frac{C_{\rm s}}{r_{\rm s}x^2} \ . \tag{5.12}$$

Integrating the above expression yields the exterior solution to the field profile as,

$$\phi_{\rm ext}(x) = \frac{(1+x)^{2-b}}{x(b-1)(b-2)}\mathcal{B} - \frac{C_{\rm s}}{x} + \phi_\infty \ . \tag{5.13}$$

Here ϕ_∞ denotes the asymptotic value of the chameleon field. Assuming that the field is negligible ($\phi_{\rm int} \simeq 0$) within the interior (*i.e.* $r < r_{\rm c}$), and enforcing the continuity between the exterior and interior solutions at $x_{\rm c} \equiv r_{\rm c}/r_{\rm s}$ one obtains,

$$\begin{aligned} x_{\rm c} &= \left(\frac{\phi_\infty(b-1)}{\mathcal{B}}\right)^{\frac{1}{1-b}} - 1 \ , \\ C_{\rm s} &= \frac{(1+x_{\rm c})^{1-b}(1-x_{\rm c}+b\,x_{\rm c})}{(b-1)(b-2)}\mathcal{B} \ . \end{aligned} \tag{5.14}$$

Amongst the above equations, the solution to the former, which we term as screening function ($\rm f_s(r)$), provides us with the screening radius ($r_{\rm c}$). In the case where the field is not screened, the exterior solution holds at any $r > 0$, with the integration constant given by,

$$C_{\rm s} = \frac{\mathcal{B}}{(b-1)(b-2)} \ , \tag{5.15}$$

which is strictly valid for $b > 2$. For the $b = 2$ case, the NFW case, the exterior field gradient:

$$\frac{{\rm d}\phi_{\rm ext}}{{\rm d}r} = \frac{\mathcal{B}}{r_{\rm s}\,x^2}\left[\frac{1}{x+1} + \ln(x+1)\right] + \frac{C_{\rm s}}{r_{\rm s}\,x^2} \ , \tag{5.16}$$

and the field profile:

$$\phi_{\rm ext}(x) = -\frac{1+\ln(x+1)}{x}\mathcal{B} - \frac{C_{\rm s}}{x} + \phi_\infty \ , \tag{5.17}$$

with the junction conditions at the matching radius, $x_{\rm c}$[3]

$$x_{\rm c} = \left[\frac{\mathcal{B}}{\phi_\infty} - 1\right] \ , \quad C_{\rm s} = -\phi_\infty - \mathcal{B}\ln\left(\frac{\mathcal{B}}{\phi_\infty}\right) \ . \tag{5.18}$$

The unscreened solution is obtained by imposing $C_{\rm s} = -\phi_\infty$. Finally, the field profile associated with the gNFW matter density comes as:

$$\frac{{\rm d}\phi_{\rm ext}}{{\rm d}r} = \frac{\mathcal{B}}{r_{\rm s}x^2}\left[\frac{x^{3-\gamma}}{3-\gamma}\,{}_2F_1(3-\gamma, 3-\gamma, 4-\gamma, -x) + 1\right] + \frac{C_{\rm s}}{r_{\rm s}^2x^2} \ , \tag{5.19}$$

[3]Note that the set of equations differs from the one of [126] due to a different definition of the normalization constant $C_{\rm s}$.

and

$$\begin{aligned}\phi_{\rm ext}(x) = &-\frac{\mathcal{B}}{x}\left[\frac{x^{3-\gamma}(1+x)^{\gamma-2}-2-x+\gamma}{\gamma-2}\right.\\ &\left.+\frac{x^{3-\gamma}}{3-\gamma}\,{}_2F_1(3-\gamma,3-\gamma,4-\gamma,-x)-\frac{C_{\rm s}}{r_{\rm s}\,x}+\phi_\infty\right.\,.\end{aligned} \tag{5.20}$$

with the junction conditions given by

$$\begin{aligned}x_c &= \left[1-\left(1+\left(\frac{\phi_\infty}{\mathcal{B}}\right)(\gamma-2)\right)^{1/(2-\gamma)}\right]^{-1}-1\,,\\ C_{\rm s} &= -\mathcal{B}r_{\rm s}\left[\frac{x_{\rm c}^{3-\gamma}}{3-\gamma}\,{}_2F_1(3-\gamma,3-\gamma,4-\gamma,-x_{\rm c})+1\right]\,.\end{aligned} \tag{5.21}$$

When the field is in the unscreened regime, no real positive solutions for the screening radius $r_{\rm c}$ can be found. The integration constant of the exterior field eq. (5.10) is then given by $C_{\rm s} = -\mathcal{B}\,r_{\rm s}$. It is worth pointing out that in eqs. (5.14) and (5.21), $r_{\rm c}$ can be explicitly expressed as a function of ϕ_∞. Such a relation is, however, not straightforward for all models.

5.2.2 Burkert solutions

For the Burkert model, the exterior field gradient is:

$$\frac{{\rm d}\phi_{\rm ext}}{{\rm d}r} = \frac{C_{\rm s}}{r_{\rm s}\,x^2}+\frac{\mathcal{B}}{r_{\rm s}\,x^2}\left[\frac{1}{4}\ln\left(x^2+1\right)+\frac{1}{2}\ln(x+1)-\frac{1}{2}\tan^{-1}(x)\right]\,, \tag{5.22}$$

and the field profile can be written as,

$$\begin{aligned}\phi_{\rm ext}(x) = &-\frac{C}{x}+\frac{\mathcal{B}}{4\,x}\left[(x-1)\ln\left(x^2+1\right)\right.\\ &\left.+2(x+1)\Big(\tan^{-1}(x)-\ln(x+1)\Big)\right]\\ &-\frac{\pi}{4}\mathcal{B}+\phi_\infty\,.\end{aligned} \tag{5.23}$$

Note that the factor $\mathcal{B}\,\pi/4$ ensures $\phi \to \phi_\infty$ for $x \to \infty$, and the matching with the inner solution is obtained when

$$C_{\rm s} = \frac{1}{4}\mathcal{B}\left[-\log\left(x_{\rm c}^2+1\right)-2\log(x_{\rm c}+1)+2\tan^{-1}(x_{\rm c})\right]$$

Finally, the screening equation is given as,

$$\ln\left[\frac{x_{\rm c}^2+1}{(x_{\rm c}+1)^2}\right]+2\tan^{-1}(x_{\rm c}) = \pi-4\frac{\phi_\infty}{\mathcal{B}}\,, \tag{5.24}$$

where the matching conditions to get r_c cannot be solved analytically. In the top panel of Fig. 5.2 we show the screening function $\mathrm{f_s(x_c)/f_s(0)}$, with

$$\mathrm{f_s}(x_\mathrm{c}) = \ln\left[\frac{x_\mathrm{c}^2+1}{(x_\mathrm{c}+1)^2}\right] + 2\tan^{-1}(x_\mathrm{c}) - \pi + 4\frac{\phi_\infty}{\mathcal{B}}\,,$$

plotted for varying values of $\frac{\phi_\infty}{\mathcal{B}}$. Wherein each profile has been normalised to its value at $r = 0$. The intersection of the screening function profiles at $\mathrm{f_s(r_c)} = 0$ provides the screening radius r_c for a given value of $\frac{\phi_\infty}{\mathcal{B}}$. It is illustrative to notice that for $\frac{\phi_\infty}{\mathcal{B}} \gtrsim 0.785 \sim \pi/4$, there exists no solution to the screening function and the entire cluster is unscreened. As it can also be seen by the structure of eq. (5.24), the solution for the screening radius r_c demands $\frac{\phi_\infty}{\mathcal{B}} \leqslant \pi/4$, *i.e.* the *rhs* should be greater or equal to zero since the *lhs* is a monotonically-increasing function of $x_c = r_c/r_s$, which is zero for $r_c = 0$, thus, strictly positive for $x_c > 0$. As mentioned earlier, this corresponds to the case where the field is unscreened and the entire cluster experiences the fifth force.

5.2.3 Isothermal solutions

The Isothermal mass density model's field gradient is

$$\frac{\mathrm{d}\phi_\mathrm{ext}}{\mathrm{d}r} = \left[C_\mathrm{s} - \mathcal{B}\left(\frac{x}{\sqrt{x^2+1}} - \ln\left(\sqrt{x^2+1}-x\right)\right)\right]\frac{1}{r_\mathrm{s}x^2}\,, \tag{5.25}$$

which, after integration, results in the following field profile

$$\phi_\mathrm{ext}(x) = -\frac{\ln(\sqrt{x^2+1}+x)}{x}\mathcal{B} - \frac{C_\mathrm{s}}{x} + \phi_\infty\,, \tag{5.26}$$

where $C_\mathrm{s} = \phi_\infty\, x_\mathrm{c} - \mathcal{B}\ln(\sqrt{x_\mathrm{c}^2+1}+x_c)$. Repeating the process explained in section 5.2, the screening equation is given by,

$$\sqrt{x_\mathrm{c}^2+1} = \frac{\mathcal{B}}{\phi_\infty}\,, \tag{5.27}$$

which has a solution only when $(\mathcal{B}/\phi_\infty)^2 > 1$.The resulting screening radius is

$$r_\mathrm{c} = r_\mathrm{s}\sqrt{\left(\frac{\mathcal{B}}{\phi_\infty}\right)^2 - 1}\,. \tag{5.28}$$

Note that in the unscreened regime (*i.e.* $x_\mathrm{c} = 0$) the constant vanishes, $C_\mathrm{s} = 0$. In the bottom panel of Fig. 5.2 we show the screening function profiles for the Isothermal mass density profile corresponding to eq. (5.28), $\mathrm{f_s}(x_\mathrm{c}) = \sqrt{x_\mathrm{c}^2+1} - \mathcal{B}/\phi_\infty$. In contrast to the Burkert profile, we find that there always exists a solution to the screening function even in the limit $\frac{\phi_\infty}{\mathcal{B}} \to 1$.

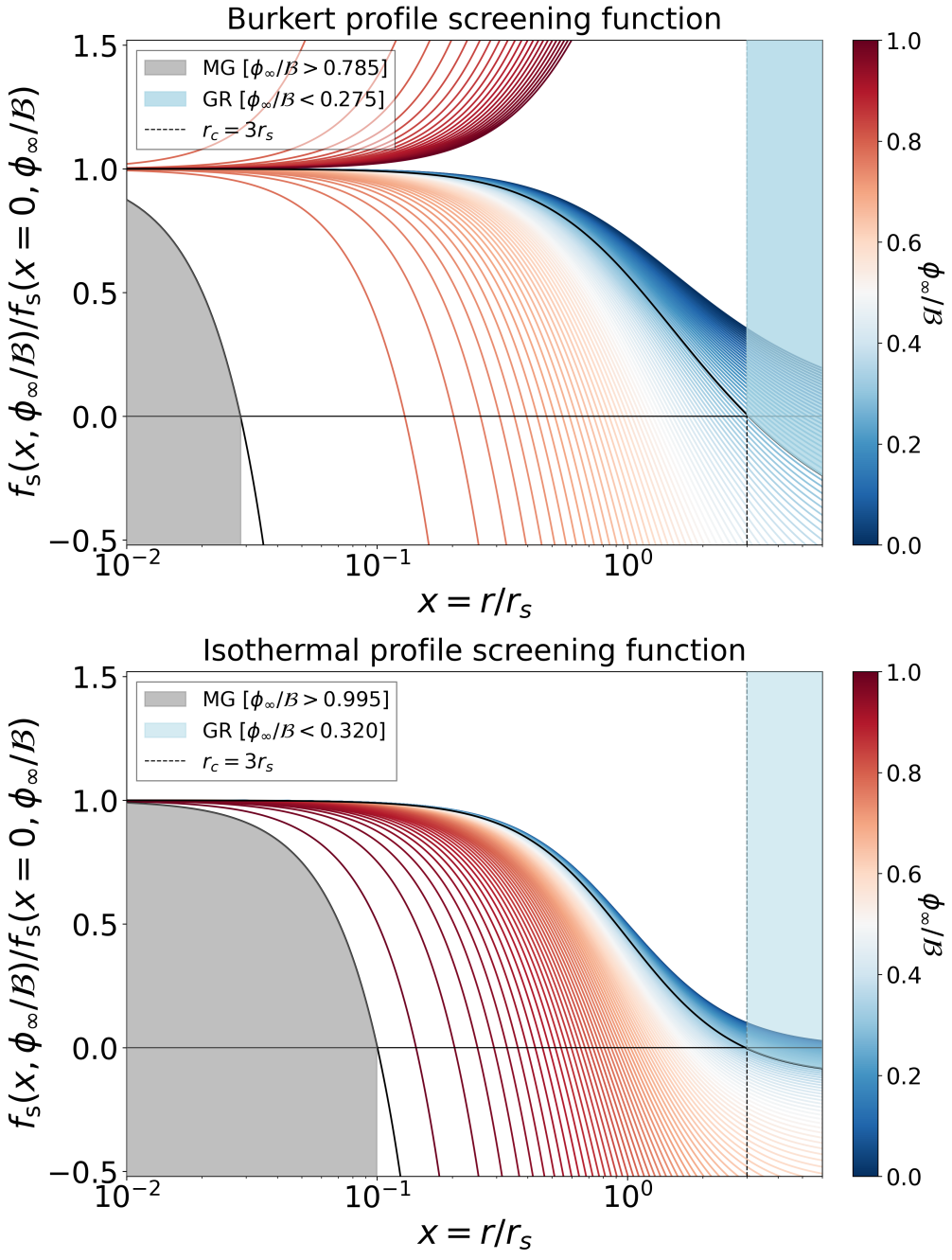

Figure 5.2: Variation of the screening function ($f_s(x)$) as a function of $\frac{\phi_\infty}{\mathcal{B}}$, for Burkert (*top*) and Isothermal (*bottom*) profiles. The vertical dashed line marks the solution when the screening radius $r_c = 3r_s$ for a given value of $\frac{\phi_\infty}{\mathcal{B}}$ for the respective mass models. The intersection of each profile with the $f_s(x) = 0$, provides the value of r_c, within which the effects of the Chameleon field are screened. To avoid the sign ambiguity of the screening function we show the re-scaled $f_s(r)/f_s(r = 0)$.

5.2.4 Einasto solutions

The gradient of the Chameleon field for the Einasto mass density model is given by

$$\frac{\mathrm{d}\phi_{\mathrm{ext}}}{\mathrm{d}r} = \frac{C_{\mathrm{s}}}{r_{\mathrm{s}}\, x^2} - \mathcal{B}\, 8^{-m} e^{2m} m^{1-3m} \frac{\Gamma\left(3m, 2m\, x^{\frac{1}{m}}\right)}{r_{\mathrm{s}}\, x^2} \ , \tag{5.29}$$

and

$$\begin{aligned} \phi_{\mathrm{ext}}(x) =& \phi_\infty - \frac{C_{\mathrm{s}}}{x} + \frac{\mathcal{B}}{x} 8^{-m} e^{2m} m^{1-3m} \times \\ & \left[2^m m^m x\, \Gamma\left(2m, 2m\, x^{\frac{1}{m}}\right) - \Gamma\left(3m, 2m\, x^{\frac{1}{m}}\right)\right] \ . \end{aligned} \tag{5.30}$$

Where $\Gamma(n, z)$ is the upper incomplete gamma function:

$$\Gamma(n, z) = \int_z^\infty \mathrm{d}t\, t^{n-1} e^{-t} \ .$$

Despite the complicated look of the field profile, it is still possible to obtain an analytical solution for the junction conditions between the screened and unscreened regimes:

$$\begin{aligned} r_{\mathrm{c}} &= r_{\mathrm{s}} \left[\frac{1}{2m} Q^{-1}\left(2m, \frac{4^m \phi_\infty m^{2m-1}}{\mathcal{B}\, e^{2m}\, \Gamma(2m)}\right)\right]^m \ , \\ C_{\mathrm{s}} &= 8^{-m} e^{2m} m^{1-3m} \Gamma\left(3m, 2m\, x_{\mathrm{s}}^{\frac{1}{m}}\right) \mathcal{B} \ , \end{aligned} \tag{5.31}$$

where $Q^{-1}(y, a)$ is the inverse of the upper regularized incomplete gamma function, as well as for the case where there is no screening

$$C_{\mathrm{s}} = 8^{-m} e^{2m} n^{1-3m}\, \Gamma(3m) \mathcal{B} \ . \tag{5.32}$$

5.2.5 Solution's existence

Finally, let us discuss the solutions' existence and compatibility with the Chameleon screening mechanism through their asymptotic behaviour. It is clear from the previous mass models eqs. (5.1) to (5.6) that when $r/r_{\mathrm{s}} \gg 1$, eq. (5.9) becomes

$$\frac{1}{r^2}\frac{d}{dr}\left(r^2 \frac{d}{dr}\phi\right) \sim \frac{1}{r^3} \ , \tag{5.33}$$

with asymptotic solution

$$\phi \sim \frac{C}{r} + \phi_\infty \ . \tag{5.34}$$

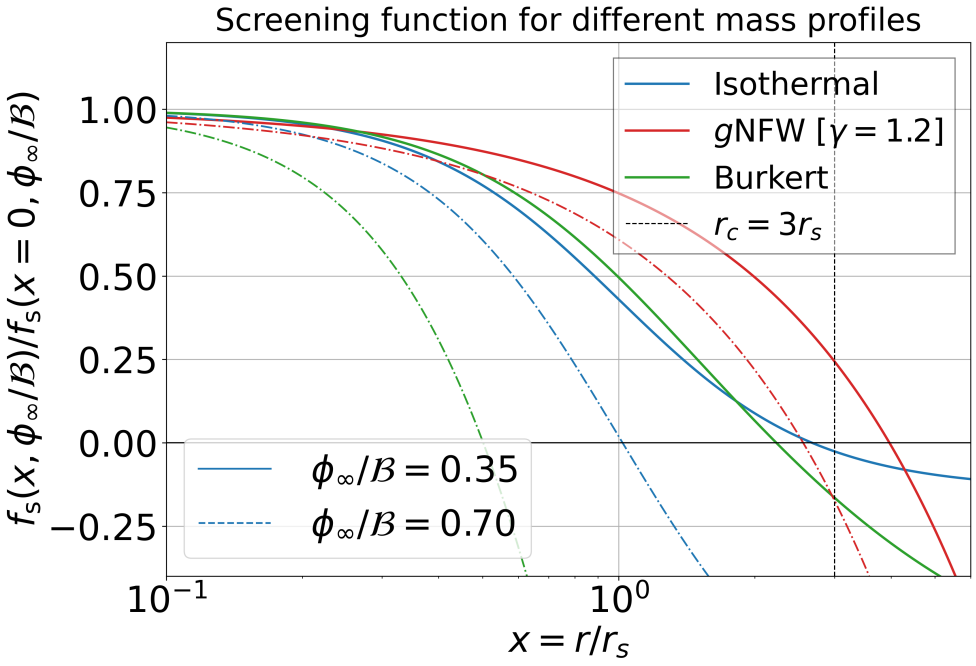

Figure 5.3: Comparison of the screening function for three different mass models, namely, Isothermal, gNFW and Burkert are shown. The screening functions plotted for two different values of $\frac{\phi_\infty}{\mathcal{B}} = 0.35$ (solid) and $\frac{\phi_\infty}{\mathcal{B}} = 0.7$ (dashed) are compared.

Therefore, all considered mass models are compatible with the Chameleon screening mechanism; that is, the field converges asymptotically to a finite background value ϕ_∞. Note that this wouldn't be the case if the matter density at large r goes as $1/r^2$. In that case, the field's solution does not converge to a finite value. In order to demonstrate that, assuming that the mass model goes as $1/r^\alpha$ for large r one can show that the resulting asymptotic behaviour is

$$\phi \sim \frac{C}{r} + C' + \frac{1}{(1-\alpha)(2-\alpha)} r^{2-\alpha} \ , \tag{5.35}$$

which consequently requires $\alpha > 2$ to have a finite solution.

Finally, in Fig 5.3, we show the comparison of the screening functions' behaviour for different mass models. Let us compare amongst the mass models shown for the same value of $\frac{\phi_\infty}{\mathcal{B}}$; we can immediately notice that the gNFW profile provides larger r_c with respect to the Isothermal and Burkert mass profiles. This implies that for the same normalization set by $\frac{\phi_\infty}{\mathcal{B}}$, using the gNFW mass profile more of the cluster is screened. It is also interesting to

note that the dependence of the solution to the screening varies significantly in the Isothermal and Burkert cases in comparison to the gNFW case.

This, in turn, implies that the gNFW profile coupled with the chameleon field screens the fifth force effects within the galaxy cluster more effectively than the two other mass profiles in comparison here. For the purpose of illustration, here we show the gNFW profile assuming $\gamma = 1.2$. Note that r_c grows with γ, and it remains larger than that obtained in the case of Burkert or Isothermal profiles for the same value of $\phi_\infty/\mathcal{B}$ down to the lower limit of $\gamma = 0$. This further indicates that the difference in r_c will be even larger for $\gamma \to 2$ in comparison to $\gamma = 1.2$.

5.3 Comparison with numerical solutions

In order to validate the approach described in section 5.2, let us compare the obtained semi-analytical solutions with the numerical solution of Eq. 4.3.

The set of numerical solutions of Eq. 4.3 were obtained through a 6^{th}-order explicit Runge-Kutta integrator while the appropriate boundary conditions – $\nabla^2\phi \approx 0$ at the centre of the mass distribution, and $\mathrm{d}\phi/\mathrm{d}r = 0$ at infinity – were imposed through a Newton-Rapshon shooting method. In order to avoid the divergence at the centre of the mass density distribution associated with some of the models, an inner cutoff radius was imposed. The value of the latter ranged between $5 - 10\%$ of the screening radius in order to get the best fit for the semi-analytic approach. The appropriate boundary condition at infinity was imposed by considering a numerically small value of the scalar field derivative, $\sim 10^{-8}$, at a scaled radius x several times larger than the main mass distribution, $x_{max} \approx 10^3$.

Comparative results between the semi-analytic (solid) and the full numerical solutions (points) can be seen in Fig. 5.4 for all the mass density models under consideration, assuming $\rho_s = 5{\times}10^{14}\,\mathrm{M}_\odot/\mathrm{Mpc}^3$, $r_s = 0.5\,\mathrm{Mpc}$, $\beta = 0.5$ and $\phi_\infty = 5 \times 10^{-5}$.

Let us now quickly analyze the difference between the semi-analytical solution and the full non-linear numerically obtained solution, Fig. 5.4. Both the effective mass (top left) and the total mass (top right), as well as the relative difference between the semi-analytically obtained and the numerically obtained solutions (bottom), are represented in Fig. 5.4. For the study of how well the semi-analytical solution describes the true solutions, let us analyze the relative difference for the effective mass. As x increases from the origin $x = 0$ until the defined cut-off radius, $x = x_\mathrm{s}$ – where the strongest assumptions and approximations were made –, while the semi-analytical is set to zero, the numerical solutions are small but non-zero, originating a large

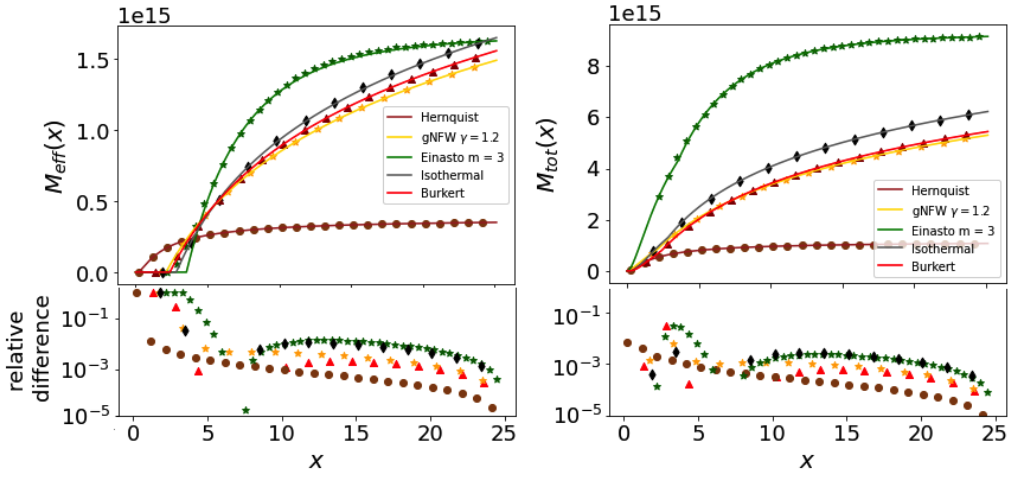

Figure 5.4: Left: Semi-analytic approximation for the effective mass $M_{\rm eff}$ (solid lines) as a function of $x = r/r_{\rm s}$ compared with the numerical solution (points) for the different mass ansatz defined in Section 5.1.1. The bottom plot indicates the relative difference between the two. Right: the same for the total dynamical mass $M_{\rm tot} = M + M_{\rm eff}$.The adopted parameters are $\rho_s = 5 \times 10^{14}\,{\rm M}_\odot/{\rm Mpc}^3$, $r_s = 0.5\,{\rm Mpc}$, $\beta = 0.5$, $\phi_\infty = 5 \times 10^{-5}$.

relative difference which is accentuated at the transitional scaled radius $x_{\rm s}$, where the numerical starts to gain significant non-zero values before the semi-analytical (smoother transition from a negligible value). This behavior is, however, canceled as one goes away from the mass distribution (increase x) to the background configuration (no mass distribution, flat scalar field profile). At this point, the semi-analytical and the numerically obtained solutions coincide almost perfectly, with a maximum relative error of 10^{-3}. Hence, besides some slight differences in the screening radius transition and asymptotic behavior, the semi-analytic approximation describes with a high degree of agreement the full numerically obtained results, giving confidence for their use in more complex calculations that will proceed. Note that the maximum discrepancy between the numerical and semi-analytic approach in the total mass $M(r) + M_{\rm eff}(r)$ (right plots) is of 7%, and corresponds to $x = \sim 2$ (*i.e.* $r \sim 1\,{\rm Mpc}$ for the adopted value of $r_{\rm s}$).

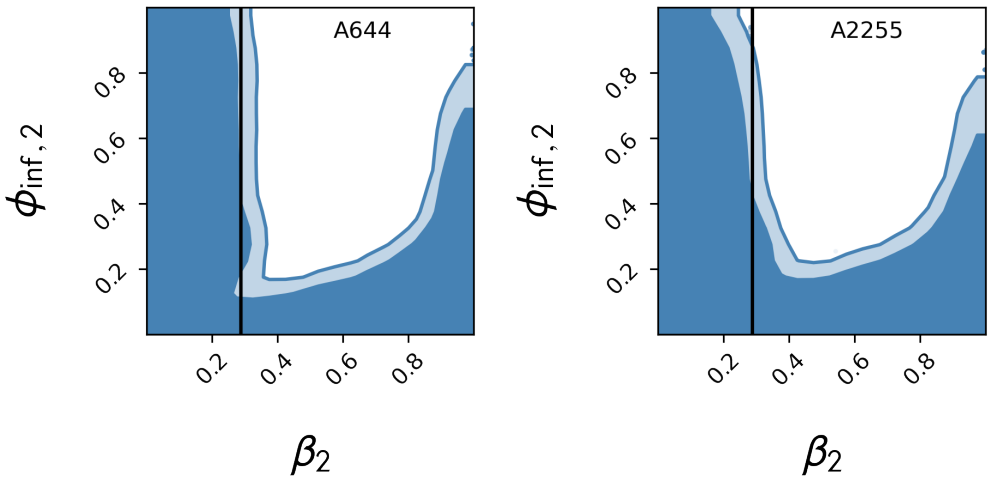

Figure 5.5: We show the 95%, 99% C.L. contours for A644 to the left and A2255 to the right utilizing the Isothermal mass profile instead of the NFW as utilised in the main analysis. The vertical line shows the $\beta_2 \sim 0.29$, corresponding to the $f(R)$ scenario where $\beta = \sqrt{1/6}$.

5.4 Constraints obtained on A644 and A2255

As discussed earlier in this Chapter, some clusters prefer a different mass model rather than NFW, for instance, as we have pointed out in second Chapter, among the 12 XCOP clusters, 3 of them does not prefer an NFW mass model, namely A644 and A2255 prefer an Isothermal mass model [137]. Using the same analysis as the one performed in the second Chapter (see section 4.4.5), we can obtain constraints on these two cluster by adopting the Isothermal mass model illustrated in section 5.2. In fig. 5.5 we present the posterirors of parameter space of the Chameleon parameters for A644 and A2255 clusters. This in fact will be the subject of the next work in preparation [199] to assess how this dependence on the mass model when using the Hydrostatic equilibrium can be aided by the kinematics in a joint analysis, to which the work presented so far is a prelude. We find in this preliminary assessment that the Isothermal mass profile is able to replicate the usual exclusion posteriors as are obtained in the case of NFW.

Chapter 6

Concluding remarks

We have Introduced General relativity as the most successful theory yet, that describes gravity, starting from the perception that spacetime is four dimensional, affected by the presence of matter and energy. Therefore, gravity is no longer seen a force but rather a distortion in the spacetime. Thus, it became possible to study the evolution of the universe through its metric by adopting the cosmological principle that states that our universe is homogeneous and isotropic for all observers. This led to concluding that our universe is not static but rather expands, following the Hubble's observations and several other cosmological observables, available at present. However, this expansion was discovered to be accelerating at recent times, as opposed to what one may think since gravity is "a pulling force". Thus a new type of dark energy had to be added in order to explain this occurrence. The later raised the question whether General Relativity is everything about gravity or this very successful theory needs modification in order to account for the mysterious dark energy effects. This, along with other considerations related to high curvature regimes like black holes, motivated the introduction of new theories that takes into consideration unexplained phenomena in the framework of General Relativity. We briefly mentioned some of these ideas in the third chapter of the first part while focusing on Chameleon gravity and consequently a subclass of $f(R)$ models.

Chameleon gravity introduces a new scalar field in the action of General Relativity, coupling to matter non minimally in a way that makes its mass dependent on the matter density, as the density grows the chameleon mass increases, making the field undetectable at high density regions such as the solar system where General Relativity is proved to be in agreement with observations. Nonetheless, the chameleon field comes into play at lower densities such as at the cosmological scales where it induces a fifth force in addition to the gravitational one. Therefore, in order to be able to detect

the affect of such a force, it is conceivable to consider cluster of galaxies.

There are different manners to constrain manifestations of MG in cosmology, involving all observables, the Cosmic Microwave Background, and the Large Scale Structure, and others. In this Thesis, we bring the analysis of manifestations of specific MG scenarios in the largest cosmological objects, namely galaxy clusters, taking the advantage of new datasets which became available recently.

We proceed to study the Chameleon field in clusters of Galaxies and improve the constraints on the same utilizing similar approach as in [126, 145]. We use the SZ pressure and X-ray XCOP data that consists of 12 clusters[4]. However, we utilize only 9 clusters among them which are known to prefer an NFW mass model[137]. The idea is to model each cluster with a single mass model and find the Chameleon field solution. Then, due to the fifth force that is proportional to the gradient of the Chameleon field, the hydrostatic pressure is modified to account for the new force. Using the XCOP data we perform an MCMC analysis to constrain parameters of the model. The analysis adopted with the consideration of different mass priors permits us to improve the constrains obtained on the Modified Gravity parameters. We obtain constraints which are among the tightest constraints obtained using the galaxy clusters to date, owing to the improvement in the data and our posterior importance sampling approach.

We then extended our analysis to include clusters which do not immediately prefer an NFW mass model. We have developed similar semi-analytical approach to solving the chameleon field equation, we do it for several mass model including NFW-type solutions, Burkert, Isothermal, Einasto. Throughout this chapter we discuss the difference between different field solutions and how effective is the screening mechanism in each of them. We also show the consistency of the chameleon field solutions with a generic mass model along with the agreement of the semi-analytical solution with the ones obtained numerically. By the end we show the contours of two of the remaining clusters of XCOP that prefer an Isothermal mass model.

Future prospects and ongoing work include the following aspects.

i) Developing pipelines, to test newer dataset to better constraint and test the nature fo gravity in galaxy clusters.

ii) Simulating clusters which prefer different mass models mentioned in the second section could reveal the difference between the constraints derived from clusters with the same mass and concentration while with different mass models. This is important as the validity of NFW profile to describe the mass in MG scenarios is not yet well understood as is subject of an ongoing work [199].

iii) It was assumed throughout the thesis that the baryonic matter can be neglected since the data is concerned with outskirts of the clusters. However, an explicit analysis could be done by considering coupling of the Chameleon field to different matter components and find the solution accordingly, as was recently explored in [200]. Although, as pointed out in section 4.4.6, we do not expect the baryonic matter to affect the constrains strongly, it will be necessary to explore this area especially in terms of its affect on the degenerate parameter space section 4.4.2 and approaching precise modeling for the better data arrive in near future.

iv) Usually, different probes of gravity in galaxy clusters are explored independently. Combining Hydrostatic data with other probes like kinematics [1] and caustics [2] could give a much tighter constraints on the models. Evidently a joint analysis of all the probes is eminent and will be more robust test of gravity.

We intend to appropriately implement our formalism here and future developments to other modifications to gravity beyond the Chameleon gravity tested in this work.

Bibliography

[1] Lorenzo Pizzuti, Yacer Boumechta, Sandeep Haridasu, Alexandre M. Pombo, Sofia Dossena, Minahil Adil Butt, Francesco Benetti, Carlo Baccigalupi, and Andrea Lapi. Mass Modeling and Kinematics of Galaxy Clusters in Modified Gravity. 7 2024.

[2] Minahil Adil Butt, Balakrishna S. Haridasu, Yacer Boumechta, Francesco Benetti, Lorenzo Pizzuti, Carlo Baccigalupi, and Andrea Lapi. Caustic and hydrostatic mass bias: Implications for modified gravity. 1 2024.

[3] Francesco Benetti, Andrea Lapi, Giovanni Gandolfi, Minahil Adil Butt, Yacer Boumechta, Balakrishna S. Haridasu, and Carlo Baccigalupi. Dark Matter in Fractional Gravity III: Dwarf Galaxies Kinematics. *Universe*, 9(11):478, 2023.

[4] Yacer Boumechta, Balakrishna S. Haridasu, Lorenzo Pizzuti, Minahil Adil Butt, Carlo Baccigalupi, and Andrea Lapi. Constraining chameleon screening using galaxy cluster dynamics. *Phys. Rev. D*, 108(4):044007, 2023.

[5] Albert Einstein. Zur elektrodynamik bewegter körper. *Annalen der Physik*, 17(10):891–921, 1905.

[6] Albert Einstein. Über den einfluss der schwerkraft auf die ausbreitung des lichtes. *Annalen der Physik*, 35(10):898–908, 1911.

[7] Albert Einstein. Die grundlage der allgemeinen relativitätstheorie. *Annalen der Physik*, 49(7):769–822, 1916.

[8] Gerardo Munoz and Preston Jones. The equivalence principle, uniformly accelerated reference frames, and the uniform gravitational field. *Am. J. Phys.*, 78:377–383, 2010.

[9] Eolo Di Casola, Stefano Liberati, and Sebastiano Sonego. Nonequivalence of equivalence principles. *Am. J. Phys.*, 83:39, 2015.

[10] G. M. Tino, L. Cacciapuoti, S. Capozziello, G. Lambiase, and F. Sorrentino. Precision Gravity Tests and the Einstein Equivalence Principle. *Prog. Part. Nucl. Phys.*, 112:103772, 2020.

[11] Hermann Minkowski. Die grundgleichungen für die elektromagnetischen vorgänge in bewegten körpern. In *Nachrichten von der Gesellschaft der Wissenschaften zu Göttingen, Mathematisch-Physikalische Klasse*, pages 53–111, 1908.

[12] Hermann Minkowski. Raum und zeit. In *Jahresberichte der Deutschen Mathematiker-Vereinigung*, volume 18, pages 75–88, 1909.

[13] Estelle Asmodelle. Tests of General Relativity: A Review. Bachelor thesis, Central Lancashire U., 2017.

[14] Ajit Kumar Mehta, Alessandra Buonanno, Roberto Cotesta, Abhirup Ghosh, Noah Sennett, and Jan Steinhoff. Tests of general relativity with gravitational-wave observations using a flexible theory-independent method. *Phys. Rev. D*, 107(4):044020, 2023.

[15] Georgios V. Kraniotis and S. B. Whitehouse. Exact calculation of the perihelion precession of mercury in general relativity, the cosmological constant and jacobi's inversion problem. *Class. Quant. Grav.*, 20:4817–4835, 2003.

[16] Joachim Wambsganss. Gravitational lensing in astronomy. *Living Rev. Rel.*, 1:12, 1998.

[17] Matthias Bartelmann. Gravitational Lensing. *Class. Quant. Grav.*, 27:233001, 2010.

[18] R. Abbott et al. Tests of General Relativity with GWTC-3. 12 2021.

[19] B. P. Abbott et al. LIGO: The Laser interferometer gravitational-wave observatory. *Rept. Prog. Phys.*, 72:076901, 2009.

[20] B. P. Abbott et al. Observation of Gravitational Waves from a Binary Black Hole Merger. *Phys. Rev. Lett.*, 116(6):061102, 2016.

[21] R. Adam et al. Planck 2015 results. I. Overview of products and scientific results. *Astron. Astrophys.*, 594:A1, 2016.

[22] P. A. R. Ade et al. Planck 2015 results. XIII. Cosmological parameters. *Astron. Astrophys.*, 594:A13, 2016.

[23] Jean-Philippe Uzan. The Big-Bang Theory: Construction, Evolution and Status. *Prog. Math. Phys.*, 76:1–72, 2021.

[24] Daniel Martin. *Manifold Theory: An Introduction for Mathematical Physicists*. E. Horwood, Chichester, 2002.

[25] Paul Renteln. *Manifolds, Tensors, and Forms: An Introduction for Mathematicians and Physicists*. Cambridge University Press, 2014.

[26] Sean M. Carroll. *Spacetime and Geometry: An Introduction to General Relativity*. Cambridge University Press, 7 2019.

[27] Charles W. Misner, K. S. Thorne, and J. A. Wheeler. *Gravitation*. W. H. Freeman, San Francisco, 1973.

[28] Steven Weinberg. *Gravitation and Cosmology: Principles and Applications of the General Theory of Relativity*. John Wiley and Sons, New York, 1972.

[29] Alexander Friedmann. Über die krümmung des raumes. *Zeitschrift für Physik*, 10:377–386, 1922.

[30] Alexander Friedmann. Über die möglichkeit einer welt mit konstanter negativer krümmung des raumes. *Zeitschrift für Physik*, 21:326–332, 1924.

[31] Georges Lemaître. Un univers homogène de masse constante et de rayon croissant rendant compte de la vitesse radiale des nébuleuses extragalactiques. *Annales de la Société Scientifique de Bruxelles*, 47A:49–59, 1927.

[32] Howard P. Robertson. Kinematics and world-structure. *Astrophysical Journal*, 82:284–301, 1935.

[33] Howard P. Robertson. Kinematics and world-structure iii. *Astrophysical Journal*, 83:257–271, 1936.

[34] Arthur G. Walker. On milne's theory of world-structure. *Proceedings of the London Mathematical Society*, 42:90–127, 1937.

[35] Sebastian De Haro. Noether's Theorems and Energy in General Relativity. 3 2021.

[36] A. Einstein. Kosmologische betrachtungen zur allgemeinen relativitätstheorie. *Sitzungsberichte der Königlich Preußischen Akademie der Wissenschaften zu Berlin*, pages 142–152, 1917.

[37] R. C. Tolman. *Relativity, Thermodynamics, and Cosmology*. Oxford University Press, 1934.

[38] Albert Petrov. *Introduction to Modified Gravity*. SpringerBriefs in Physics. Springer, 2nd edition, 2023.

[39] H. Vermeil. Die theorie der relativistischen gravitation und die lichtausbreitung im gravitationsfeld. *Nachrichten der Gesellschaft der Wissenschaften zu Göttingen*, page 334, 1917.

[40] E. Cartan. Sur les espaces à connexion affine de courbure constante. *Journal de Mathématiques Pures et Appliquées*, 1:141–202, 1922.

[41] Hermann Weyl. *Space-Time-Matter*. Dover Publications, New York, 1922.

[42] D. Lovelock. The einstein tensor and the identity. *Journal of Mathematical Physics*, 12:498–504, 1971.

[43] D. Lovelock. The form of the gravitational field equation. *Journal of Mathematical Physics*, 13:874–878, 1972.

[44] Claudius Ptolemy. *Almagest*. Translated by G. J. Toomer, Duckworth, London, 150. Revised edition, 1984.

[45] Nicolaus Copernicus. *De revolutionibus orbium coelestium*. Johannes Petreius, Nuremberg, 1543.

[46] Galileo Galilei. *Sidereus Nuncius*. Thomas Baglioni, Venice, 1610.

[47] Tycho Brahe. *Astronomiae Instauratae Progymnasmata*. Typis Rostochii [Posthumously by Johannes Kepler], Prague, 1602.

[48] Johannes Kepler. *Astronomia Nova*. Typis Mylleri, Heidelberg, 1609.

[49] Johannes Kepler. *Harmonices Mundi*. Johannes Plank, Linz, 1619.

[50] Isaac Newton. *Philosophiæ Naturalis Principia Mathematica*. Royal Society, London, 1687.

[51] A. Einstein. Die feldgleichungen der gravitation. *Sitzungsberichte der Königlich Preußischen Akademie der Wissenschaften zu Berlin*, 1915:844–847, 1915.

[52] Willem de Sitter. On the curvature of space. *Proc. Amsterdam Academy*, 19:1217–1225, 1917.

[53] Edwin Hubble. A relation between distance and radial velocity among extra-galactic nebulae. *Proceedings of the National Academy of Sciences*, 15(3):168–173, 1929.

[54] George Gamow. *The Creation of the Universe*. Viking Press, New York, 1952.

[55] Arno A. Penzias and Robert W. Wilson. A measurement of excess antenna temperature at 4080 mc/s. *Astrophysical Journal*, 142:419–421, 1965.

[56] E. et al. Komatsu. Seven-year wilkinson microwave anisotropy probe (wmap) observations: Cosmological interpretation. *Astrophysical Journal Supplement Series*, 192(2):18, 2011.

[57] P. A. R. Ade et al. Planck 2015 results. XXIV. Cosmology from Sunyaev-Zeldovich cluster counts. *Astron. Astrophys.*, 594:A24, 2016.

[58] Fritz Zwicky. Die rotverschiebung von extragalaktischen nebeln. *Helvetica Physica Acta*, 6:110–127, 1933.

[59] Vera Rubin and Kent Ford. Rotation of the andromeda nebula from a spectroscopic survey of emission regions. *Astrophysical Journal*, 159:379–403, 1970.

[60] J. A. Tyson, R. A. Wenk, and F. Valdes. Detection of systematic gravitational lensing distortions in a field of faint galaxies. *Astrophysical Journal*, 349:L1–L4, 1990.

[61] Georges Lemaître. L'univers en expansion. *Annales de la Société Scientifique de Bruxelles*, 53:51–85, 1933.

[62] Hermann Bondi. Spherically symmetric models in general relativity. *Monthly Notices of the Royal Astronomical Society*, 107:410–425, 1947.

[63] D. J. Fixsen, J. C. Mather, C. L. Bennett, et al. The temperature of the cosmic microwave background. *Astrophysical Journal*, 473:576–587, 1996.

[64] Daniel Baumann. *Cosmology*. Cambridge University Press, Cambridge, 2019.

[65] C. Ma and E. Bertschinger. Cosmological perturbation theory. *Astrophysical Journal*, 455:7–25, 1995.

[66] U. Seljak and M. Zaldarriaga. The cmb anisotropies: Theory. *Astrophysical Journal*, 469:437–448, 1996.

[67] M. Kamionkowski, D. N. Spergel, and N. Sugiyama. Large-scale structure and the cosmic microwave background. *Physical Review D*, 55:7368–7382, 1997.

[68] W. Hu and S. Dodelson. Cosmological perturbation theory. *Annual Review of Astronomy and Astrophysics*, 40:171–216, 2002.

[69] Adam G. Riess et al. Observational evidence from supernovae for an accelerating universe and a cosmological constant. *Astron. J.*, 116:1009–1038, 1998.

[70] N. Aghanim et al. Planck 2018 results. VI. Cosmological parameters. *Astron. Astrophys.*, 641:A6, 2020. [Erratum: Astron.Astrophys. 652, C4 (2021)].

[71] Planck Collaboration. Planck 2018 results. I. Overview and the cosmological legacy of Planck. , 641:A1, September 2020.

[72] Steven Weinberg. The Cosmological Constant Problem. *Rev. Mod. Phys.*, 61:1–23, 1989.

[73] Philip Bull et al. Beyond ΛCDM: Problems, solutions, and the road ahead. *Phys. Dark Univ.*, 12:56–99, 2016.

[74] S. Dodelson. *Modern Cosmology*. Academic Press, 2003.

[75] Alan H. Guth. Inflationary universe: A possible solution to the horizon and flatness problems. *Physical Review D*, 23:347–356, 1981.

[76] Andrei D. Linde. A new inflationary universe scenario: A possible solution of the horizon, flatness, homogeneity, isotropy, and primordial monopole problems. *Physics Letters B*, 108:389–393, 1982.

[77] Andreas Albrecht and Paul J. Steinhardt. Cosmology for grand unified theories with radiatively induced symmetry breaking. *Physical Review Letters*, 48:1220–1223, 1982.

[78] Shin'ichi Nojiri and Sergei D. Odintsov. Introduction to modified gravity and gravitational alternative for dark energy. *International Journal of Geometric Methods in Modern Physics*, 4:115–146, 2007.

[79] Timothy Clifton, Pedro G. Ferreira, Antonio Padilla, and Constantinos Skordis. Modified gravity and cosmology. *Physics Reports*, 513:1–189, 2012.

[80] Shinji Tsujikawa. Modified gravity models of dark energy. *Lect. Notes Phys.*, 800:99–145, 2010.

[81] Shin'ichi Nojiri and Sergei D. Odintsov. Unified cosmic history in modified gravity: from F(R) theory to Lorentz non-invariant models. *Phys. Rept.*, 505:59–144, 2011.

[82] Timothy Clifton, Pedro G. Ferreira, Antonio Padilla, and Constantinos Skordis. Modified Gravity and Cosmology. *Phys. Rept.*, 513:1–189, 2012.

[83] S. Nojiri, S. D. Odintsov, and V. K. Oikonomou. Modified Gravity Theories on a Nutshell: Inflation, Bounce and Late-time Evolution. *Phys. Rept.*, 692:1–104, 2017.

[84] Serge Reynaud and Marc-Thierry Jaekel. Tests of general relativity in the solar system. *Proc. Int. Sch. Phys. Fermi*, 168:203–217, 2009.

[85] Wei-Tou Ni. Solar-system tests of the relativistic gravity. *Int. J. Mod. Phys. D*, 25(14):1630003, 2016.

[86] Philip Bull, Timothy Clifton, Pedro G. Ferreira, et al. Beyond λcdm: Problems, solutions, and the road ahead. *Physics of the Dark Universe*, 12:56–99, 2016.

[87] Roger Penrose. Gravitational collapse and space-time singularities. *Phys. Rev. Lett.*, 14:57–59, 1965.

[88] Stephen W. Hawking and Roger Penrose. *The Nature of Space and Time*. Princeton University Press, 1970.

[89] C. M. Will. The confrontation between general relativity and experiment. *Living Reviews in Relativity*, 17:4, 2014.

[90] J. Baeza-Ballesteros, A. Donini, and S. Nadal-Gisbert. Dynamical measurements of deviations from Newton's $1/r^2$ law. *Eur. Phys. J. C*, 82(2):154, 2022.

[91] D. Lovelock. The Einstein tensor and its generalizations. *J. Math. Phys.*, 12:498–501, 1971.

[92] Pedro G. S. Fernandes, Pedro Carrilho, Timothy Clifton, and David J. Mulryne. The 4D Einstein–Gauss–Bonnet theory of gravity: a review. *Class. Quant. Grav.*, 39(6):063001, 2022.

[93] David Langlois and Karim Noui. Degenerate higher derivative theories beyond Horndeski: evading the Ostrogradski instability. *JCAP*, 1602(02):034, 2016.

[94] Marco Crisostomi, Kazuya Koyama, and Gianmassimo Tasinato. Extended Scalar-Tensor Theories of Gravity. *JCAP*, 1604(04):044, 2016.

[95] Jibril Ben Achour, Marco Crisostomi, Kazuya Koyama, David Langlois, Karim Noui, and Gianmassimo Tasinato. Degenerate higher order scalar-tensor theories beyond Horndeski up to cubic order. *JHEP*, 12:100, 2016.

[96] Hayato Motohashi, Karim Noui, Teruaki Suyama, Masahide Yamaguchi, and David Langlois. Healthy degenerate theories with higher derivatives. *JCAP*, 1607(07):033, 2016.

[97] Justin Khoury. Chameleon Field Theories. *Class. Quant. Grav.*, 30:214004, 2013.

[98] Clare Burrage, Edmund J. Copeland, Adam Moss, and James A. Stevenson. The shape dependence of chameleon screening. *JCAP*, 01:056, 2018.

[99] Philippe Brax, Carsten van de Bruck, Anne-Christine Davis, and Anne M. Green. Small scale structure formation in chameleon cosmology. *Phys. Lett. B*, 633:441–446, 2006.

[100] Philippe Brax, Carsten van de Bruck, Anne-Christine Davis, Justin Khoury, and Amanda Weltman. Detecting dark energy in orbit: The cosmological chameleon. *Phys. Rev. D*, 70:123518, 2004.

[101] Philippe Brax, Anne-C. Davis, Baojiu Li, Hans A. Winther, and Gong-Bo Zhao. Systematic simulations of modified gravity: chameleon models. *JCAP*, 04:029, 2013.

[102] Narayan Banerjee, Sudipta Das, and Koyel Ganguly. Chameleon field and the late time acceleration of the universe. *Pramana*, 74:L481–L489, 2010.

[103] Y. Fujii and K. Maeda. *The scalar-tensor theory of gravitation*. Cambridge Monographs on Mathematical Physics. Cambridge University Press, 7 2007.

[104] Tsutomu Kobayashi. Horndeski theory and beyond: a review. *Rept. Prog. Phys.*, 82(8):086901, 2019.

[105] Gregory W. Horndeski and Alessandra Silvestri. 50 Years of Horndeski Gravity: Past, Present and Future. *Int. J. Theor. Phys.*, 63(2):38, 2024.

[106] Alberto Nicolis, Riccardo Rattazzi, and Enrico Trincherini. The Galileon as a local modification of gravity. *Phys. Rev. D*, 79:064036, 2009.

[107] Hans A. Buchdahl. Non-linear Lagrangians and cosmological theory. *Mon. Not. Roy. Astron. Soc.*, 150:1, 1970.

[108] Justin Khoury and Amanda Weltman. Chameleon fields: Awaiting surprises for tests of gravity in space. *Phys. Rev. Lett.*, 93:171104, 2004.

[109] Justin Khoury and Amanda Weltman. Chameleon cosmology. *Phys. Rev. D*, 69:044026, 2004.

[110] Thomas Faulkner, Max Tegmark, Emory F. Bunn, and Yi Mao. Constraining f(R) Gravity as a Scalar Tensor Theory. *Phys. Rev. D*, 76:063505, 2007.

[111] I. Navarro and K. Van Acoleyen. f(R) actions, cosmic acceleration and local tests of gravity. *JCAP*, 02:022, 2007.

[112] Burin Gumjudpai and Phongsaphat Rangdee. Non-minimal derivative coupling gravity in cosmology. *Gen. Rel. Grav.*, 47(11):140, 2015.

[113] Je-An Gu, Chung-Chi Lee, and Chao-Qiang Geng. Teleparallel Dark Energy with Purely Non-minimal Coupling to Gravity. *Phys. Lett. B*, 718:722–726, 2013.

[114] Nima Arkani-Hamed, Savas Dimopoulos, and G. R. Dvali. The Hierarchy problem and new dimensions at a millimeter. *Phys. Lett. B*, 429:263–272, 1998.

[115] Lisa Randall and Raman Sundrum. A Large mass hierarchy from a small extra dimension. *Phys. Rev. Lett.*, 83:3370–3373, 1999.

[116] J. M. Overduin and P. S. Wesson. Kaluza-Klein gravity. *Phys. Rept.*, 283:303–380, 1997.

[117] Francesco Benetti, Andrea Lapi, Giovanni Gandolfi, and Stefano Liberati. A relativistic scalar model for fractional interaction between dark matter and gravity. *Class. Quant. Grav.*, 41(17):175010, 2024.

[118] R. R. Caldwell, Rahul Dave, and Paul J. Steinhardt. Cosmological imprint of an energy component with general equation of state. *Phys. Rev. Lett.*, 80:1582–1585, 1998.

[119] Thomas P. Waterhouse. An Introduction to Chameleon Gravity. 11 2006.

[120] Raziyeh Zaregonbadi, Mehrdad Farhoudi, and Nematollah Riazi. Dark Matter From f(R,T) Gravity. *Phys. Rev. D*, 94:084052, 2016.

[121] Alexei A. Starobinsky. A New Type of Isotropic Cosmological Models Without Singularity. *Phys. Lett. B*, 91:99–102, 1980.

[122] Assaf Shomer. A Pedagogical explanation for the non-renormalizability of gravity. 9 2007.

[123] K. S. Stelle. Renormalization of Higher Derivative Quantum Gravity. *Phys. Rev. D*, 16:953–969, 1977.

[124] Wayne Hu and Ignacy Sawicki. Models of f(R) Cosmic Acceleration that Evade Solar-System Tests. *Phys. Rev. D*, 76:064004, 2007.

[125] Philippe Brax, Carsten van de Bruck, Anne-Christine Davis, and Douglas J. Shaw. f(R) Gravity and Chameleon Theories. *Phys. Rev. D*, 78:104021, 2008.

[126] Ayumu Terukina, Lucas Lombriser, Kazuhiro Yamamoto, David Bacon, Kazuya Koyama, and Robert C. Nichol. Testing chameleon gravity with the Coma cluster. *JCAP*, 04:013, 2014.

[127] Alexei A. Starobinsky. Disappearing cosmological constant in f(R) gravity. *JETP Lett.*, 86:157–163, 2007.

[128] Hiroaki Oyaizu, Marcos Lima, and Wayne Hu. Nonlinear evolution of f(R) cosmologies. 2. Power spectrum. *Phys. Rev. D*, 78:123524, 2008.

[129] Julio F. Navarro, Carlos S. Frenk, and Simon D. M. White. The Structure of cold dark matter halos. *Astrophys. J.*, 462:563–575, 1996.

[130] J. Stuart B. Wyithe, E. L. Turner, and D. N. Spergel. Gravitational lens statistics for generalized nfw profiles: parameter degeneracy and implications for self-interacting cold dark matter. *Astrophys. J.*, 555:504, 2001.

[131] Jesus Zavala, Dario Nunez, Roberto A. Sussman, Luis G. Cabral-Rosetti, and Tonatiuh Matos. Stellar polytropes and NFW halo model: Stellar polytropes and Navarro-Frenk-White halo models: comparison with observations. *JCAP*, 06:008, 2006.

[132] Tonatiuh Matos and Dario Nunez. The general relativistic geometry of the Navarro - Frenk - White model. *Rev. Mex. Fis.*, 51:71–75, 2005.

[133] Razieh Dehghani, Paolo Salucci, and H. Ghaffarnejad. Navarro-Frenk-White dark matter profile and the dark halos around disk systems. *Astron. Astrophys.*, 643:A161, 2020.

[134] K. Asano. Usability of the nfw galaxy profile as a cosmological tool estimated from 2-image gravitational lens systems. *Publ. Astron. Soc. Jap.*, 52:99, 2000.

[135] Ayumu Terukina, Lucas Lombriser, Kazuhiro Yamamoto, David Bacon, Kazuya Koyama, and Robert C. Nichol. Testing chameleon gravity with the Coma cluster. , 2014(4):013, April 2014.

[136] S. Ettori, V. Ghirardini, D. Eckert, F. Dubath, and E. Pointecouteau. Dark matter distribution in X-ray luminous galaxy clusters with Emergent Gravity. *Mon. Not. Roy. Astron. Soc.*, 470(1):L29–L33, 2017.

[137] S. Ettori, V. Ghirardini, D. Eckert, E. Pointecouteau, F. Gastaldello, M. Sereno, M. Gaspari, S. Ghizzardi, M. Roncarelli, and M. Rossetti. Hydrostatic mass profiles in X-COP galaxy clusters. *Astron. Astrophys.*, 621:A39, 2019.

[138] D. Eckert, S. Ettori, E. Pointecouteau, S. Molendi, S. Paltani, and C. Tchernin. The XMM cluster outskirts project (X-COP). *Astron. Nachr.*, 338(2/3):293–298, 2017.

[139] V. Ghirardini et al. Universal thermodynamic properties of the intracluster medium over two decades in radius in the X-COP sample. *Astron. Astrophys.*, 621:A41, 2019.

[140] Christian Arnold, Ewald Puchwein, and Volker Springel. Scaling relations and mass bias in hydrodynamical $f(R)$ gravity simulations of galaxy clusters. *Mon. Not. Roy. Astron. Soc.*, 440(1):833–842, 2014.

[141] Myles A. Mitchell, Jian-hua He, Christian Arnold, and Baojiu Li. A general framework to test gravity using galaxy clusters – I. Modelling the dynamical mass of haloes in $f(R)$ gravity. *Mon. Not. Roy. Astron. Soc.*, 477(1):1133–1152, 2018.

[142] Myles A. Mitchell, Christian Arnold, and Baojiu Li. A general framework to test gravity using galaxy clusters – V. A self-consistent pipeline for unbiased constraints of f(R) gravity. *Mon. Not. Roy. Astron. Soc.*, 508(3):4157–4174, 2021.

[143] Hans A. Winther et al. Modified Gravity N-body Code Comparison Project. *Mon. Not. Roy. Astron. Soc.*, 454(4):4208–4234, 2015.

[144] Lucas Lombriser, Baojiu Li, Kazuya Koyama, and Gong-Bo Zhao. Modeling halo mass functions in chameleon $f(r)$ gravity. *Phys. Rev. D*, 87:123511, Jun 2013.

[145] Harry Wilcox et al. The XMM Cluster Survey: Testing chameleon gravity using the profiles of clusters. *Mon. Not. Roy. Astron. Soc.*, 452(2):1171–1183, 2015.

[146] Raziyeh Zaregonbadi, Nasim Saba, and Mehrdad Farhoudi. Cosmic acceleration and geodesic deviation in chameleon scalar field model. *Eur. Phys. J. C*, 82(8):730, 2022.

[147] A. N. Ivanov and M. Wellenzohn. Can a Chameleon Field Be Identified with Quintessence? *Universe*, 6(12):221, 2020.

[148] Lucila Kraiselburd, Susana J. Landau, Marcelo Salgado, Daniel Sudarsky, and Héctor Vucetich. Equivalence Principle in Chameleon Models. *Phys. Rev. D*, 97(10):104044, 2018.

[149] Shinji Tsujikawa, Takashi Tamaki, and Reza Tavakol. Chameleon scalar fields in relativistic gravitational backgrounds. *JCAP*, 05:020, 2009.

[150] Ryotaro Kase and Shinji Tsujikawa. Screening the fifth force in the Horndeski's most general scalar-tensor theories. *JCAP*, 08:054, 2013.

[151] Matthieu Schaller, Carlos S. Frenk, Richard G. Bower, Tom Theuns, James Trayford, Robert A. Crain, Michelle Furlong, Joop Schaye, Claudio Dalla Vecchia, and I. G. McCarthy. The effect of baryons on the inner density profiles of rich clusters. *Monthly Notices of the Royal Astronomical Society*, 452(1):343–355, 07 2015.

[152] M. T. Hogan, B. R. McNamara, F. Pulido, P. E. J. Nulsen, H. R. Russell, A. N. Vantyghem, A. C. Edge, and R. A. Main. Mass distribution in galaxy cluster cores. *The Astrophysical Journal*, 837(1):51, mar 2017.

[153] B. Sartoris, A. Biviano, P. Rosati, A. Mercurio, C. Grillo, S. Ettori, M. Nonino, K. Umetsu, P. Bergamini, G. B. Caminha, and M. Girardi. CLASH-VLT: a full dynamical reconstruction of the mass profile of Abell S1063 from 1 kpc out to the virial radius. , 637:A34, May 2020.

[154] L. Lombriser, K. Koyama, G.-B. Zhao, and B. Li. Chameleon f(R) gravity in the virialized cluster. , 85(12):124054, June 2012.

[155] Difu Shi, Baojiu Li, Jiaxin Han, Liang Gao, and Wojciech A. Hellwing. Exploring the liminality: properties of haloes and subhaloes in borderline f(R) gravity. , 452(3):3179–3191, September 2015.

[156] Harry Wilcox, Robert C. Nichol, Gong-Bo Zhao, David Bacon, Kazuya Koyama, and A. Kathy Romer. Simulation tests of galaxy cluster constraints on chameleon gravity. *Mon. Not. Roy. Astron. Soc.*, 462(1):715–725, 2016.

[157] Aneesh P. Naik, Ewald Puchwein, Anne-Christine Davis, Debora Sijacki, and Harry Desmond. Constraints on chameleon f(R)-gravity from galaxy rotation curves of the SPARC sample. , 489(1):771–787, October 2019.

[158] Lorenzo Pizzuti, Ippocratis D. Saltas, and Luca Amendola. MG-MAMPOSST: a code to test modifications of gravity with internal kinematics and lensing analyses of galaxy clusters. , 506(1):595–612, September 2021.

[159] Baojiu Li and John D. Barrow. n-body simulations for coupled scalar-field cosmology. *Phys. Rev. D*, 83:024007, Jan 2011.

[160] Baojiu Li and George Efstathiou. An extended excursion set approach to structure formation in chameleon models. , 421(2):1431–1442, April 2012.

[161] Baojiu Li and Hongsheng Zhao. Structure formation by the fifth force: Segregation of baryons and dark matter. *Phys. Rev. D*, 81:104047, May 2010.

[162] Bhuvnesh Jain, Vinu Vikram, and Jeremy Sakstein. Astrophysical Tests of Modified Gravity: Constraints from Distance Indicators in the Nearby Universe. *Astrophys. J.*, 779:39, 2013.

[163] H. A. Buchdahl. Non-Linear Lagrangians and Cosmological Theory. *Monthly Notices of the Royal Astronomical Society*, 150(1):1–8, 09 1970.

[164] Philippe Brax, Carsten van de Bruck, Anne-Christine Davis, and Douglas J. Shaw. f(R) gravity and chameleon theories. , 78(10):104021, November 2008.

[165] Yong-Seon Song, Wayne Hu, and Ignacy Sawicki. The Large Scale Structure of f(R) Gravity. *Phys. Rev. D*, 75:044004, 2007.

[166] Lorenzo Pizzuti, Ippocratis D. Saltas, Andrea Biviano, Gary Mamon, and Luca Amendola. MG-MAMPOSSt, a Fortran code to test gravity at galaxy-cluster scales. *J. Open Source Softw.*, 8(81):4800, 2023.

[167] Rajeev Kumar Jain, Chris Kouvaris, and Niklas Grønlund Nielsen. White Dwarf Critical Tests for Modified Gravity. *Phys. Rev. Lett.*, 116(15):151103, 2016.

[168] Juan M. Z. Pretel, Sergio E. Jorás, and Ribamar R. R. Reis. Strongest constraint in f(R) = R+ α R^2 gravity: stellar stability. , 2020(11):048, November 2020.

[169] Marco Raveri, Bin Hu, Noemi Frusciante, and Alessandra Silvestri. Effective Field Theory of Cosmic Acceleration: constraining dark energy with CMB data. *Phys. Rev. D*, 90(4):043513, 2014.

[170] Matteo Cataneo, David Rapetti, Lucas Lombriser, and Baojiu Li. Cluster abundance in chameleonf(r) gravity i: toward an accurate halo mass function prediction. *JCAP*, 2016(12):024–024, Dec 2016.

[171] L. Pizzuti, B. Sartoris, L. Amendola, S. Borgani, A. Biviano, K. Umetsu, A. Mercurio, P. Rosati, I. Balestra, G. B. Caminha, M. Girardi, C. Grillo, and M. Nonino. CLASH-VLT: constraints on f(R) gravity models with galaxy clusters using lensing and kinematic analyses. *JCAP*, 7:023, July 2017.

[172] E L D Perico, R Voivodic, M Lima, and D F Mota. Cosmic voids in modified gravity scenarios. *arXiv e-prints*, page arXiv:1905.12450, May 2019.

[173] Xiangkun Liu, Baojiu Li, Gong-Bo Zhao, Mu-Chen Chiu, Wei Fang, Chuzhong Pan, Qiao Wang, Wei Du, Shuo Yuan, Liping Fu, and Zuhui Fan. Constraining $f(r)$ gravity theory using weak lensing peak statistics from the canada-france-hawaii-telescope lensing survey. *Phys. Rev. Lett.*, 117:051101, Jul 2016.

[174] Harry Desmond and Pedro G. Ferreira. Galaxy morphology rules out astrophysically relevant Hu-Sawicki f (R) gravity. , 102(10):104060, November 2020.

[175] Lixin Xu. Constraints on $f(r)$ gravity through the redshift space distortion. *Phys. Rev. D*, 91:063008, Mar 2015.

[176] Alexey Vikhlinin, A. Kravtsov, W. Forman, C. Jones, M. Markevitch, S. S. Murray, and L. Van Speybroeck. Chandra sample of nearby relaxed galaxy clusters: Mass, gas fraction, and mass-temperature relation. *Astrophys. J.*, 640:691–709, 2006.

[177] M. McDonald et al. The Remarkable Similarity of Massive Galaxy Clusters from z $\sim$ 0 to z $\sim$ 1.9. *Astrophys. J.*, 843(1):28, 2017.

[178] Balakrishna S. Haridasu, Purnendu Karmakar, Marco De Petris, Vincenzo F. Cardone, and Roberto Maoli. Testing generalized scalar-tensor theories of gravity with clusters of galaxies. 11 2021.

[179] Balakrishna S. Haridasu, Purnendu Karmakar, Marco De Petris, Vincenzo F. Cardone, and Roberto Maoli. Generalised scalar-tensor theories of gravity and pressure profiles of galaxy clusters. In *mm Universe @ NIKA2* , 11 2021.

[180] P.A.R. Ade et al. Planck 2013 results. XXIX. The Planck catalogue of Sunyaev-Zeldovich sources. *Astron. Astrophys.*, 571:A29, 2014.

[181] Ricardo Herbonnet, Cristobal Sifon, Henk Hoekstra, Yannick Bahe, Remco F. J. van der Burg, Jean-Baptiste Melin, Anja von der Linden, David Sand, Scott Kay, and David Barnes. CCCP and MENeaCS: (updated) weak-lensing masses for 100 galaxy clusters. *Mon. Not. Roy. Astron. Soc.*, 497(4):4684–4703, 2020.

[182] D. Foreman-Mackey, D. W. Hogg, D. Lang, and J. Goodman. emcee: The MCMC Hammer. *Publications of the Astronomical Society of the Pacific*, 125:306, March 2013.

[183] David W. Hogg and Daniel Foreman-Mackey. Data analysis recipes: Using Markov Chain Monte Carlo. *Astrophys. J. Suppl.*, 236(1):11, 2018.

[184] Antony Lewis. GetDist: a Python package for analysing Monte Carlo samples. 10 2019.

[185] Aaron D. Ludlow, Julio F. Navarro, Raul E. Angulo, Michael Boylan-Kolchin, Volker Springel, Carlos Frenk, and Simon D. M. White. The mass–concentration–redshift relation of cold dark matter haloes. *Mon. Not. Roy. Astron. Soc.*, 441(1):378–388, 2014.

[186] Aaron A. Dutton and Andrea V. Macciò. Cold dark matter haloes in the Planck era: evolution of structural parameters for Einasto and NFW profiles. *Mon. Not. Roy. Astron. Soc.*, 441(4):3359–3374, 2014.

[187] Piotr Oleśkiewicz, Carlton M. Baugh, and Aaron Ludlow. The connection between halo concentrations and assembly histories: a probe of gravity? *Mon. Not. Roy. Astron. Soc.*, 489(4):4658–4668, 2019.

[188] Myles A. Mitchell, César Hernández-Aguayo, Christian Arnold, and Baojiu Li. A general framework to test gravity using galaxy clusters IV: cluster and halo properties in DGP gravity. *Mon. Not. Roy. Astron. Soc.*, 508(3):4140–4156, 2021.

[189] Pier Stefano Corasaniti, Carlo Giocoli, and Marco Baldi. Dark matter halo sparsity of modified gravity scenarios. , 102(4):043501, August 2020.

[190] Mauro Sereno, Cosimo Fedeli, and Lauro Moscardini. Comparison of weak lensing by nfw and einasto halos and systematic errors. *Journal of Cosmology and Astroparticle Physics*, 2016(01):042–042, January 2016.

[191] Sébastien Peirani, Yohan Dubois, Marta Volonteri, Julien Devriendt, Kevin Bundy, Joe Silk, Christophe Pichon, Sugata Kaviraj, Raphaël Gavazzi, and Mélanie Habouzit. Density profile of dark matter haloes and galaxies in the horizon–agn simulation: the impact of AGN feedback. *Monthly Notices of the Royal Astronomical Society*, 472(2):2153–2169, 08 2017.

[192] Ayumu Terukina and Kazuhiro Yamamoto. Gas Density Profile in Dark Matter Halo in Chameleon Cosmology. , 86(10):103503, November 2012.

[193] Hongsheng Zhao. Analytical models for galactic nuclei. , 278(2):488–496, January 1996.

[194] Andreas Burkert. The Structure and evolution of weakly selfinteracting cold dark matter halos. *Astrophys. J. Lett.*, 534:L143–L146, 2000.

[195] Ivan King. The structure of star clusters. I. an empirical density law. , 67:471, October 1962.

[196] J. Einasto. On the Construction of a Composite Model for the Galaxy and on the Determination of the System of Galactic Parameters. *Trudy Astrofizicheskogo Instituta Alma-Ata*, 5:87–100, January 1965.

[197] Andrius Tamosiunas, Chad Briddon, Clare Burrage, Weiguang Cui, and Adam Moss. Chameleon screening depends on the shape and structure of NFW halos. *JCAP*, 04(04):047, 2022.

[198] Lars Hernquist. An Analytical Model for Spherical Galaxies and Bulges. , 356:359, June 1990.

[199] Yacer Boumechta, Sandeep Haridasu, Lorenzo Pizzuti, Alexandre M. Pombo, Sofia Dossena, Minahil Adil Butt, Carlo Baccigalupi, and Andrea Lapi. Mass Modeling in Modified Gravity: Joint assessement of Hydrostatics and Kinematics of Galaxy Clusters. *In. prep.*, 2024.

[200] Lorenzo Pizzuti, Valentina Amatori, Alexandre M. Pombo, and Sandeep Haridasu. The shape of the Chameleon fifth-force on the mass components of galaxy clusters. 11 2024.